UNIVERSITAT POLITÈCNICA DE CATALUNYA
BARCELONATECH
Institut de Tècniques Energètiques

Neutron-induced fission cross section of ^{240,242}Pu

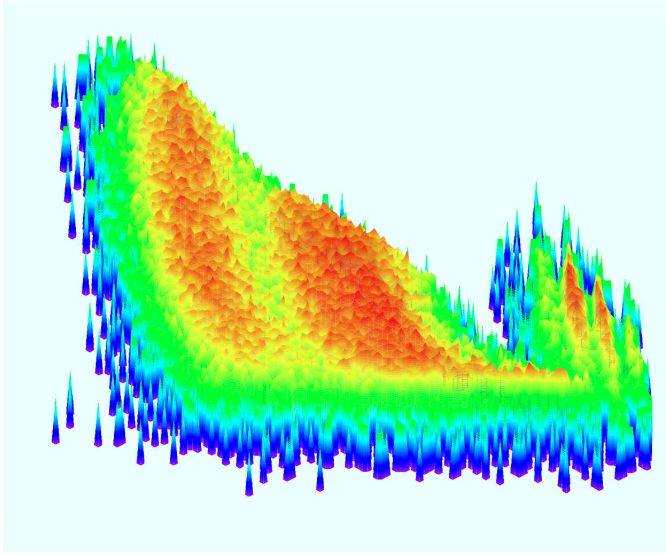

Paula Salvador-Castiñeira

Supervisors:
Dr. Franz-Josef Hambsch
Dr. Carme Pretel

Doctoral dissertation
PhD in Nuclear Engineering and Ionizing Radiation
Barcelona, September 2014

UNIVERSITAT POLITÈCNICA DE CATALUNYA
BARCELONATECH
Escola de Doctorat

Acta de qualificació de tesi doctoral

Curs acadèmic:

Nom i cognoms

Programa de doctorat

Unitat estructural responsable del programa

Resolució del Tribunal

Reunit el Tribunal designat a l'efecte, el doctorand / la doctoranda exposa el tema de la seva tesi doctoral titulada

_____

_____.

Acabada la lectura i després de donar resposta a les qüestions formulades pels membres titulars del tribunal, aquest atorga la qualificació:

☐ NO APTE ☐ APROVAT ☐ NOTABLE ☐ EXCEL·LENT

(Nom, cognoms i signatura) President/a		(Nom, cognoms i signatura) Secretari/ària
(Nom, cognoms i signatura) Vocal	(Nom, cognoms i signatura) Vocal	(Nom, cognoms i signatura) Vocal

_____, _____ d'/de _____ de _____

El resultat de l'escrutini dels vots emesos pels membres titulars del tribunal, efectuat per l'Escola de Doctorat, a instància de la Comissió de Doctorat de la UPC, atorga la MENCIÓ CUM LAUDE:

☐ SÍ ☐ NO

(Nom, cognoms i signatura) President de la Comissió Permanent de l'Escola de Doctorat	(Nom, cognoms i signatura) Secretària de la Comissió Permanent de l'Escola de Doctorat

Barcelona, _____ d'/de _____ de _____

Universitat Politècnica de Catalunya

Institut de Tècniques Energètiques

Neutron-induced fission cross section of ^{240,242}Pu

Author:
Paula Salvador-Castiñeira

Supervisors:
Dr. Franz-Josef Hambsch
Dr. Carme Pretel

Barcelona, Setembre 2014
Programa de Doctorat: Enginyeria Nuclear i de les Radiacions Ionitzants
Tesi presentada per obtenir el títol de Doctora per la Universitat Politècnica de Catalunya

Abstract

Nuclear data needs for the newest generation (Gen-IV) of nuclear power plants focus, mainly, on several neutron-induced fission cross section in the fast neutron energy region. Following the directions of the Nuclear Energy Agency (NEA) [1] and within the Accurate Nuclear Data for nuclear Energy Sustainability (ANDES) collaboration [2], the neutron-induced fission cross section of ^{240,242}Pu needs to be determined with improved accuracy of 1-3% and of 5%, respectively. At the Institute for Reference Materials and Measurements (JRC-IRMM) a measurement of this cross section relative to three different fission cross section standards (^{235}U, ^{238}U and ^{237}Np) was performed using a Twin Frisch-Grid Ionization Chamber. The neutrons were produced at the 7 MV Van de Graaff accelerator, covering an energy range from 0.3 MeV to 3 MeV. In addition to an extended study on the overall corrections needed to achieve accurate cross section results, the spontaneous fission half-life for ^{240,242}Pu has been determined, too.

KEYWORDS: neutron-induced fission cross section, ^{240}Pu, ^{242}Pu, ^{237}Np, ^{238}U, spontaneous fission half-life, Ionization chambers, accelerator.

Als meus Pares
i germans

Publication List

I. Salvador-Castiñeira, P., Bryś, T., Eykens, R., Moens, M., Hambsch, F.-J., Oberstedt, S., Pretel, C., Sibbens, G., Vanleeuw, D., Vidali, M., **Highly accurate measurements of the spontaneous fission half-life of ^{240,242}Pu**, Physical Review C 88.6 (2013): 064611.

II. Vanleeuw, D., Sapundjiev, D., Sibbens, G., Oberstedt, S., Salvador-Castiñeira, P., **Physical vapor deposition of metallic lithium**, Journal of Radioanalytical and Nuclear Chemistry, DOI: 10.1007/s10967-013-2669-6 (2013).

III. Salvador-Castiñeira, P., Bryś, T., Hambsch, F.-J., Oberstedt, S., Pretel, C., Vidali, M., **Neutron-induced fission cross section of ^{240,242}Pu up to E_n=3 MeV**, Nuclear Data Sheets 119, 55-57 (2014).

IV. Salvador-Castiñeira, P., Bevilacqua, R., Bryś, T., Hambsch, F.-J., Oberstedt, S., Pretel, C., Vidali, M., **Measurement of the neutron-induced fission cross section of ^{240,242}Pu**, Physics Procedia 47, 150-155 (2013).

Contents

List of Acronyms

ABTR	Advanced Breeder Test Reactor
ANDES	Accurate Nuclear Data for nuclear Energy Sustainability
CFD	Constant Fraction Discriminator
DAQ	data acquisition system
DSP	digital signal processing
EXFOR	Experimental Nuclear Reaction Data Library
FF	fission fragment
FNR	Fast Neutron Reactors
GIF	Generation IV International Forum
HPRL	High Priority Request List
HV	high voltage
IC	ionization chamber
IEA	International Energy Agency
JRC-IRMM	Joint Research Center - Institute for Reference Materials and Measurements
NEA	Nuclear Energy Agency
PCI	Peripheral Component Interconnect
PH	pulse height
SF	spontaneous fission
TFA	Timing Filter Amplifier
TFGIC	Twin Frisch-Grid Ionization Chamber

VdG Van de Graaff

WFD Waveform Digitizers

WP Work Package

List of Figures

List of Tables

Introduction

The aim of this project is to provide the nuclear data community, in particular evaluators, with new accurate data on the neutron-induced fission cross section of ^{240,242}Pu. This project should achieve the target accuracy requested by the OECD/NEA [1], 1-3% for ^{240}Pu(n,f) and 5% for ^{242}Pu(n,f), as current accuracies are 5% and 20%, respectively. The neutron energy of interest is in the fast region, from 300 keV up to 3 MeV, which correspond to the neutron spectrum in the core of GEN-IV nuclear power plants. The challenge of these two transuranium isotopes falls in the difficulty of getting the material of appropriate purity and in their high α-activity, what makes them difficult to handle.

In Chapter 1, the importance of measuring the neutron-induced fission cross section of ^{240,242}Pu is explained. An overview of the current status of the nuclear energy in the overall share of energy production is presented. The nuclear data needs for the improved designs of the new generations of nuclear power plants are listed. Additionally, the main purposes to be achieved by the ANDES collaboration, where this project was englobed, are disclosed.

The previous experimental data sets available in the literature are described together with the most recent evaluations in Chapter 2. Also, the importance of the uncertainties in experimental data is interpreted.

All the experimental laboratories, techniques and samples used are disclosed in Chapter 3. Specially, an extended discussion is given on the neutron flux characterization and the sample mass measurements; issues that are believed to be a key point of the excellent performance of cross section measurements.

In Chapter 4, the newly digital system to acquire data is expound. The main advantages of this system are listed.

Thanks to the spontaneous fission half-lives of both isotopes ^{240,242}Pu, the experimental techniques could be improved without the need of beam time. In addition, highly accurate values of the spontaneous fission could be determined for both isotopes as explained in Chapter 5.

The fission cross section measurements are explained in Chapter 6. Not only the mathematical formulation is given, but a detailed description of the corrections needed to achieve final results are revealed. Special care is taken for the MCNP simulations,

since they are of stake for the correct comprehension of the neutron spectra seen by the different reference samples used. In addition, a detailed description of the uncertainties implied in this experiment is listed. Finally, the reference cross section evaluations are presented.

All the cross section results are listed chronologically in Chapter 7. Discussions on the different results achieved are given.

Finally, in the Conclusions, an overview of the work is given and further measurements are proposed.

Chapter 1
The future of nuclear energy

1.1 Nuclear energy and power plants

The total worldwide electricity production by nuclear energy in 2011 was around 12% according to the International Energy Agency (IEA) [3] (see Figure 1.1). Nuclear energy production takes place in only 30 countries. In those countries production ranges from around 2% of their consumption, as in China, up to 78%, as in France. The fossil fuel share of electricity generation has been in a steady state since 1973, around 70% of the total. Yet, one can see that nowadays coal and peat produce around 40% of electricity, while natural gas around 22% and oil just 5%. With an actual scenario that predicts an increase of the global electricity production by a factor of two in 2050, it is likely that fossil fuels being used today will run short by this date and, with a constant purpose of reducing the CO_2 emissions, the electricity generation will need to be focused shortly on renewables and nuclear sources. Besides, natural uranium is becoming more difficult to extract and its enrichment is a highly-priced technique, thus reprocessing of nuclear waste and its use for the next generation (Generation IV) of nuclear power plants has become an interesting option for managing long-lived waste and reducing the use of fossil fuels in the near future.

In the case of the installed capacity of nuclear energy, it is expected to be three times higher in 2050, with an increased share from emerging countries such as China or India. In addition, the nuclear share of global electricity production is predicted to raise from 14% up to 23% according to the NEA and the IEA [4, 5] (see Figure 1.2).

After the Fukushima accident in 2011 several countries decided to back away from producing their energy with nuclear power plants and move to other sources of energy, mainly coal, wind and solar. Nevertheless, other countries did not just decide to keep on getting energy from nuclear, but they also approved an extended program to build nuclear power plants. One example is the United Kingdom, that has 16 operational reactors, 4 planned and 7 proposed. In addition, emerging economies are the ones building the highest number of power plants in the world, including nuclear ones. China has 21 operational reactors, 28 under construction, 58 planned and 118 proposed and India, 21 operable, 6 under construction, 18 planned and 39 proposed [6]. Worldwide there are 435 civil power nuclear reactors operational today, and 72 under construction [7]. This means that the present situation all over the world concerning

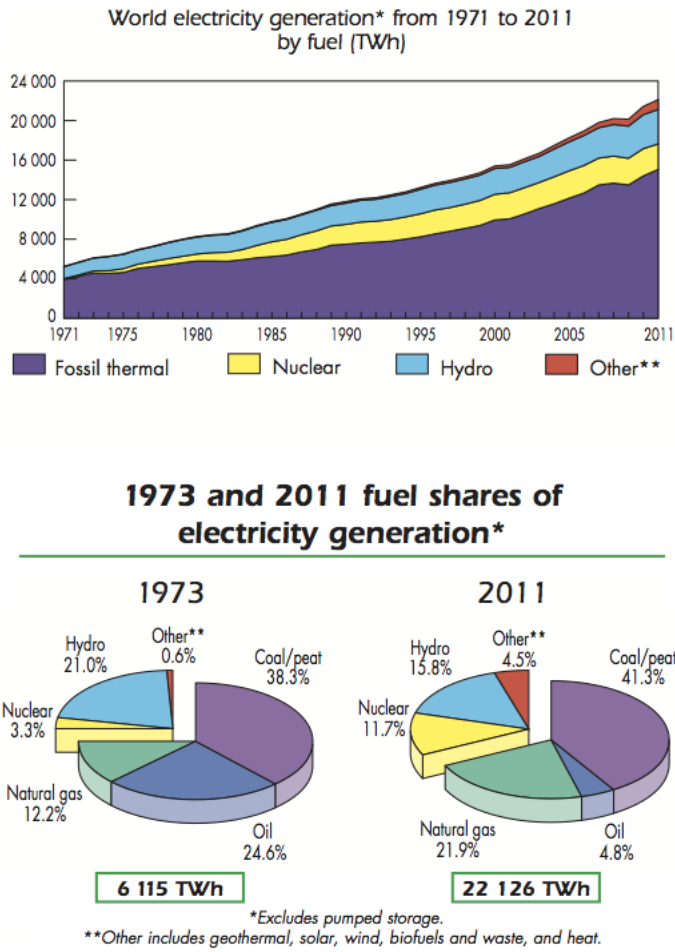

Figure 1.1: World electricity production in 1973 and 2011 [3].

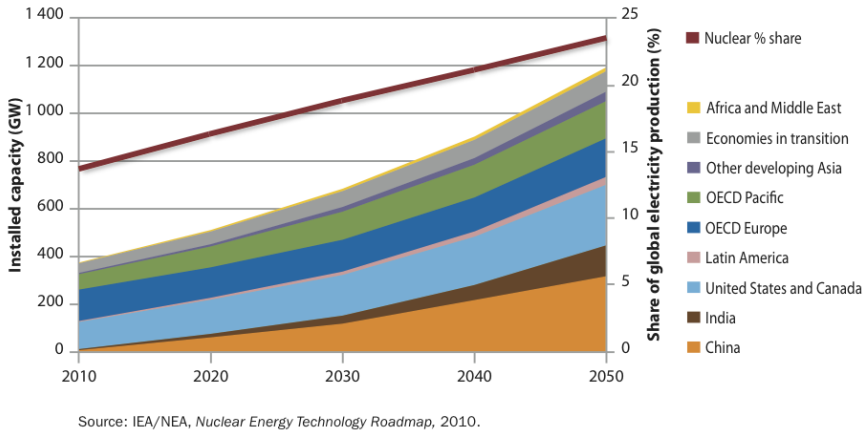

Figure 1.2: Growth in nuclear power capacity and its share of global electricity production [4, 5].

nuclear energy is quite disperse and not all the countries are taking the same path for their energy production. The new designs of nuclear power plants will provide a safer and cheaper technology. On top, by avoiding the use of ^{235}U, the nuclear waste will be reduced, such as long-lived actinides and fission products, with the consequent reduction of storage[1].

1.2 Evolution of nuclear power plants

Nuclear power plants are classified in several groups according to their technology and corresponding to the time they were designed and/or constructed. These groups are the so-called generations,

Generation I: developed in the 1950-60s. Early prototypes and experimental reactors. The only ones that are still running today are in the United Kingdom.

Generation II: developed and built in the 1970-1990s. Most of the operational reactors today: Light Water Reactors (LWR), Pressurized Water Reactor (PWR), Boiling Water Reactor (BWR), ... Their design life is around 40 years. Even though, their life cycles are being extended now to 60 years and it is likely that they will be extended further to 80 years.

Generation II+: Evolution of the designs of Gen-II, mainly enhancing safety and extending their designed life up to 60 years. Built after the year 2000.

Generation III: Evolution of Gen-II. Developed during the last decades (1990-2000). The major developments are the improved fuel technology, increased thermal efficiency, passive safety systems and designs for reducing maintenance and costs. Advanced LWRs. The first ones are already in operation in Japan and others are under construction or planned.

Generation III+: Evolution of Gen-III. After 2000. Evolutionary designs in terms of improved economics and safety features.

Generation IV: Totally new designs. To be operational not earlier than 2020. (An extended explanation is followed.)

Many improvements have been achieved since the early days concerning the design and operation of nuclear power plants. Probably, with the knowledge acquired and the technologies of nowadays most of the major accidents which happened (Three Mile Island, Chernobyl, Fukushima) could have been avoided. The development of

[1] Further reading on nuclear waste management and storage can be found in Ref. [8].

the Generation-IV of nuclear reactors will enhance sustainability, economics, safety, reliability and proliferation-resistance.

The Generation IV International Forum (GIF) [9] was initiated in 2000 by 9 countries[2] to review around 100 concepts of reactors. In 2002, 6 reactor technologies were selected. The election was made in terms of meeting increased energy demands on a sustainable basis by means of clean, safe and cost-effective models. In addition, non-proliferation and security against terrorist attacks were considered. Three of the six reactors were Fast Neutron Reactors (FNR), one epithermal and two thermal. Most of them are meant to use a closed fuel cycle to minimize waste and optimize available resources. The explanation will be extended for the FNR since these are the most relevant for this project.

1.2.1 Fast neutron reactors

FNR use in a more efficient way uranium and have the major advantage that they can be employed to burn minor actinides. Thus, reducing the long-lived nuclear waste produced by previous generations of reactors.

A FNR is a reactor where the chain reaction is sustained by fast neutrons emitted during the fission process without any moderator. This is the main reason why, by using the same fuel as thermal reactors, a fast reactor will be less efficient. Not moderating the neutrons implies to use a much higher enriched uranium fuel (>20%) or using plutonium as fuel. The plutonium fuel can be obtained from light water reactors, because their spent fuel is a mixture of ^{238,239,240,242}Pu. The content of ^{240,242}Pu increases rapidly by capture of thermal neutrons. This excess of plutonium needs to be discarded after the first cycle, having two possibilities: either store it as a long-lived nuclear waste or use it as a fuel for fast reactors.

When ^{239}Pu fissions, it generates on average 25% more neutrons than ^{235}U. This means that it is not only possible to maintain the chain reaction but, in addition, to convert ^{238}U into ^{239}Pu continuously. Usually a liquid metal, such as sodium, is used as coolant to avoid any neutron moderation and provide an efficient heat transfer medium.

The designs being considered for FNR are listed in Table 1.1. Despite, just three of the configurations were initially considered FNR two of the other models were found to be able to work either thermal or fast.

[2]Argentina, Brazil, Canada, France, Japan, Republic of Korea, South Africa, the United Kingdom and the United States. Afterwards 4 other countries joined the charter: Switzerland (2002), Euratom (2003), the People's Republic of China (2006) and the Russian Federation (2006).

Table 1.1: Main types and characteristics of Fast Neutron Reactors (Data from Ref. [10, 11].)

Type of reactor	Neutron spectrum	Coolant	Temperature (°C)	Pressure	Fuel type	Fuel cycle
Gas-cooled (GFR)	fast	helium	850	high	^{238}U	closed, on site
Lead-cooled (LFR)	fast	lead or Pb-Bi	480-800	low	^{238}U	closed, regional
Molten-salt (MSR)	fast, thermal	fluoride salts	700-800	low	UF in salt	closed
Sodium-cooled (SFR)	fast	sodium	550	low	^{238}U MOX	closed
Supercritical water-cooled (SCWR)	thermal, fast	water	510-625	very high	UO_2	closed or open

Major developments in Europe and worldwide

Even though there were six initial designs to be studied in terms of sustainability, safety and reliability, economic competitiveness, proliferation resistance and physical protection; major efforts were employed mainly in Sodium-cooled Fast Reactors (SFR) and the Very-High-Temperature Reactor (VHTR) design. Several FNRs have been operating either for experimental purposes, as prototypes or even as commercial units since the early 1950's. Some others are currently under development. The main successes have been:

Phénix & Superphénix (France): the first commercial fast breeder reactors. Phénix was operated from 1973 till 2009; Superphénix from 1985 till 1998.

Astrid (France): Sodium-cooled reactor. It is conceived as a 600 MWe prototype for a commercial 1500 MWe, that would burn the plutonium in used MOX fuel. Its high fuel burn up will include minor actinides. The final decision of construction will be made in 2019.

Allegro (France and Euratom): Gas-cooled fast reactor. A 50-100 MWt version can be expected by 2025. Two of the main objectives of the design will be to have a fuel incorporating minor actinides and determine its feasibility as an alternative of the sodium-cooled design.

MYRRHA (Belgium): 57 MWt accelerator-driven system to be build in Mol (Belgium). It consists of a proton accelerator delivering a 600 MeV, 2.5 mA (or 350 MeV, 5 mA) proton beam to a liquid lead-bismuth (Pb-Bi) spallation target that in turn couples to a Pb-Bi cooled, subcritical fast nuclear core. It will be

used to study transmutation of long-lived radionuclides in nuclear waste. Its construction should start in 2015 and its operation in 2023.

EBR series & IFR (USA): EBR-II (1960s) was a sodium-cooled breeder reactor with on-site reprocessing of metallic fuel. Then, it shifted to testing materials and fuels. It became the first Integral Fast Reactor (IFR) prototype using metallic alloy U-Pu-Zr fuels and proving inherent safety, improved management of high-level nuclear waste by recycling all actinides and using the full energy potential of uranium. The program was closed in 1994, but is now again under consideration by the Advanced Fuel Cycle Initiative.

BN-600, BN-350 (Russia and Kazakhstan): fast breeder reactor. Those two reactors were connected to the grid already for more than 20 years and used uranium oxide fuel enriched from 17 up to 26%. An updated model, BN-800 is almost constructed and has the possibility of fuel flexibility: U + Pu nitride, MOX, or metal. The version BN-1200 is under development.

JSFR (Japan): The Japan Sodium-cooled Fast Reactor (JSFR) will be a unit from 500 to 1500 MWe that will burn actinides with uranium and plutonium in oxide fuel.

FBTR, PFBR (India): A Fast Breeder Test Reactor (FBTR) has been operative since 1985 with a power of 40 MWt. A Prototype Fast Breeder Reactor (PFBR) is expected to be operative at the end of 2014. It will produce 500 MWe with a uranium-plutonium oxide fuel and with a thorium blanket to breed ^{233}U.

CEFR (China): The Chinese Experimental Fast Reactor (CEFR) is a fast neutron reactor of 65 MWt. It was connected to the grid in 2011 achieving 20 MWe.

1.2.2 Nuclear data needs for the Gen-IV nuclear power plants

In the previous section a short summary of major developments of innovative nuclear power plants was given. The knowledge already acquired with these prototypes together with the improved modeling tools that are nowadays available have been a breakthrough to determine the major nuclear data needs for FNRs.

The international nuclear data community, involving partners from theoretical modeling, evaluators and experimentalists, defined in 2008 the most urgent nuclear data needs for the Gen-IV fast reactors and other designs. The members of the so-called Subgroup 26 of the Working Party on Evaluation Co-operation (WPEC) of the OECD/NEA made, in addition, a comprehensive sensitivity and uncertainty study to evaluate the impact of neutron cross section uncertainties on the most significant integral parameters related to the core and fuel cycle of a wide range of innovative

Table 1.2: Summary of highest priority of nuclear data and their target accuracies for fast reactors [1].

		Energy Range (MeV)	Current Accuracy (%)	Target Accuracy (%)
^{238}U	σ_{inel}	0.498 - 6.07	10 - 20	2 - 3
	σ_{capt}	2.04 - 24.8	3 - 9	1.5 - 2
^{239}Pu	σ_{capt}	0.002 - 498	7 - 15	4 - 7
^{241}Pu	σ_{fiss}	454 eV - 1.35	8 - 20	2 - 3 (SFR,GFR,LFR) 5 - 8 (ABTR,EFR)
^{240}Pu	σ_{fiss}	0.498 - 1.35	6	1.5 - 2
	ν	0.498 - 1.35	4	1 - 3
^{242}Pu	σ_{fiss}	0.498 - 2.23	19 - 21	3 - 5
^{238}Pu	σ_{fiss}	0.183 - 1.35	17	3 - 5
^{242m}Am	σ_{fiss}	0.067 - 1.35	17	3 - 4
^{241}Am	σ_{fiss}	2.23 - 6.07	12	3
^{244}Cm	σ_{fiss}	0.498 - 1.35	50	5
^{245}Cm	σ_{fiss}	0.067 - 0.183	47	7
^{56}Fe	σ_{inel}	0.498 - 2.23	16 - 25	3 - 6
^{23}Na	σ_{inel}	0.498 - 1.35	28	4 - 10
^{206}Pb	σ_{inel}	1.35 - 2.23	14	3
^{207}Pb	σ_{inel}	0.498 - 1.35	11	3
^{28}Si	σ_{inel}	1.35 - 6.07	14 - 50	3 - 6
	σ_{capt}	6.07 - 19.6	53	6

systems. The discrepancy in different evaluations is aimed to be solved by having a common criteria to assess and improve the quality and completeness of such files [1]. The high priority nuclear data needs for fast reactors are presented in Table 1.2.

As it can be observed, not only several actinides that will have a major impact in the chain reaction taking place in the fuel were evaluated, but several structural, moderator and coolant materials (Fe, Na, Pb and Si) involved in FNRs were considered as well.

1.2.3 The importance of ^{240,242}Pu and other actinides

The chain reaction of a nuclear reactor is ensured when a neutron produced by the fission process is able to interact with another nucleus leading to fission. Neutrons produced by fission have an energy of several MeV, thus in thermal reactors they need to be moderated using, for instance, water or graphite. These neutrons, then, can

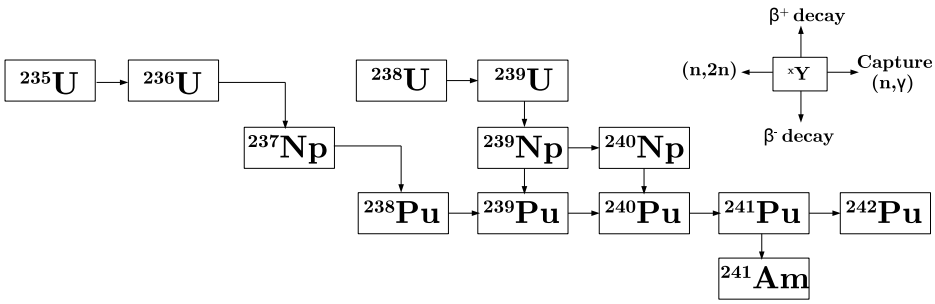

Figure 1.3: Example of processes that can lead to the production of ^{240,242}Pu and other minor actinides in the fuel of a nuclear power plant core.

interact with atoms of ^{235}U to maintain the chain reaction and the energy production. Instead, in a fast reactor, where the initial fuel is often highly enriched uranium, the neutrons emitted have enough energy to interact and fission not just with ^{235}U atoms, but with the ones from ^{238}U and other actinides. These actinides are mainly produced inside the core due to neutron capture of ^{238}U (see Figure 1.3). Since the chain reaction is favored using fast neutrons, there is no need of a moderator such as water. The fast neutron environment minimizes neutron capture reactions and maximizes fission in actinides. As a consequence, there will be less long-lived nuclides in high-level waste.

1.3 The ANDES collaboration

The ANDES collaboration started in 2009 involving 20 partners from Europe in the field of nuclear physics and nuclear energy applications [2].

Nuclear fission is not just considered as a key source of energy for electricity production, but a system that will help to reduce the dependence on fossil sources of energy. Not only Europe is producing nowadays about 30% of its energy by means of nuclear power plants, but emerging countries, where several of the world largest economies are englobed, have constructed and planned nuclear power plants to satisfy their energy needs. However, and specially after the Fukushima accident in 2011, there is an urgent need to improve the sustainability and security for such plants. In terms of sustainability three key points need to be considered: the optimization of the use of natural resources (such as Uranium), the minimization of final high level waste and the economical competitiveness. To meet those requirements the new Gen-IV designs need to be optimized.

A high-level modeling of those power plants will be followed by a more reliable and cost-effective design and safety assessment. These can only be achieved if high-quality and -accurate nuclear data can be used in those models. With such simulations, the costs of development and operation of the plants can be reduced, reaching higher efficiencies with increased safety standards.

These new designs of nuclear power plants involve the use of new fuels (which might have a large content of Pu and minor actinides), new coolants and structural material, new spectra, closed fuel cycles with multiple recycling, and so on. Not only these aspects are an arising source of challenges, but the simulation tools available require an upgrade to provide better precision to improve the preliminary designs of the new reactors.

Considering all the above mentioned, the ANDES project aimed to construct a program to address the most critical points of the knowledge of nuclear data for its application to the development of the new nuclear systems and their fuel cycles to enhance the nuclear energy sustainability. The project was divided into several Work Packages (WPs):

WP1: Measurements for advanced reactor systems

WP2: Uncertainties and covariances of nuclear data

WP3: Integral experiments for validation of nuclear data and constraints on uncertainties

WP4: High energy model validation in the 150-600 MeV energy domain

WP5: Management, dissemination, education and training

The present work was part of WP1.

1.3.1 Related projects within the ANDES collaboration

Four of the 20 partners were involved in task 1.3 of WP1: High accuracy measurements for fission. Those partners were: the *Centre National de la Recherche Scientifique* (CNRS, France), the *Istituto Nazionale di Fisica Nucleare* (INFN, Italy), the *Instituto Tecnologico e Nuclear* (ITN, Portugal) and the *Joint Research Centre - Institute for Reference Materials and Measurements* (JRC-IRMM, Belgium).

Task 1.3 involved the measurement of the neutron-induced fission cross section of ^{238}Pu, ^{240}Pu, ^{242}Pu, ^{241}Am, ^{243}Am and ^{245}Cm, as well as fission yields for n+Pu, Np and Cm. The three projects related with the ^{240,242}Pu(n,f) will be explained hereafter.

^{240,242}Pu(n,f) measurement at the Van de Graaff facility at JRC-IRMM

This experiment will be the one discussed in this thesis. The measurement was made by means of a TFGIC with a back-to-back configuration. The reference isotopes used were ^{237}Np, ^{238}U and ^{235}U. The quasi-monoenergetic neutrons were produced with the Van de Graaff (VdG) accelerator at the JRC-IRMM and the energy range covered was from 0.3 MeV up to 3 MeV.

The main challenge of the experiment was the fact that two of the reference isotopes used are not primary standards but secondary. This means that their uncertainties are higher than for a primary standard. For instance, the uncertainty associated with the ^{238}U neutron-induced fission cross section is around 0.7% for the neutron energy range used. Even more, ^{237}Np(n,f) is not considered as a standard and its uncertainty ranges from 3 to 4% in the present energy region.

^{240,242}Pu(n,f) measurement at the n_TOF facility at CERN

A MicroMegas detector was used to measure simultaneously ^{240,242}Pu(n,f) relative to the primary standard ^{235}U(n,f). Neutrons were produced at the n_TOF time-of-flight facility at CERN covering an energy range from sub-threshold up to 2 MeV.

The main challenge of this experiment was the unexpected signal degradation of the fission fragments from the ^{240}Pu(n,f) reaction due to its strong α-radiation.

^{240,242}Pu(n,f) measurement at the AIFIRA facility at CNRS

The technique used by the CNRS group consisted in placing the two Pu samples in a sandwich between two solar cells. The fission fragment detection efficiency is around 70%, due to the close geometry between the samples and the cells. At the same plane a polyethylene foil was placed, producing recoil protons when a neutron interaction happened. These protons were detected by a silicon telescope. The first measurements were performed at the Van de Graaff facility at Bruyères-le-Châtel (CEA, France). The data analysis is in progress.

The main challenges of this experiment were the fast degradation of the solar cells due to the high α-activity of the ^{240,242}Pu, specially the one of ^{240}Pu, and the energy range limitation of the proton recoil telescope.

These three experiments will be explained in more detail in Chapter 2, together with previous experiments available in the literature.

Chapter 2

State-of-the-Art

2.1 Current experiments within the ANDES collaboration

As mentioned in Chapter 1, two other measurements of the neutron-induced fission cross section of ^{240,242}Pu were carried out using different techniques and to different standards.

2.1.1 ^{240,242}Pu(n,f) measurement at the n_TOF facility (INFN, ITN)

The first measurement was performed at the n_TOF facility (CERN) by the INFN. The setup used was the Micromegas (Micro-MEsh GAseous Structure) detector [12]. A Micromegas detector consists of two electrodes separated by a distance of a few mm and, in between them, at a distance of tens of μm from the anode, a micromesh with holes on its surface is placed (see Figure 2.1). The cathode holds the sample. Two regions are discernible: the charge collection region (cathode-micromesh) and an amplification region (micromesh-anode). The amplification region enhances the signal-to-noise ratio. The detector assembly had a total of 10 Micromegas detectors: 4 of them held samples of ^{240}Pu, 4 of ^{242}Pu, 1 of ^{235}U and a dummy; a picture of it can be seen in Figure 2.2. The ^{240,242}Pu samples were produced at JRC-IRMM and had a total mass (activity) of 3.1 mg (30 MBq) and 3.6 mg (1.2 MBq), respectively.

The detector was placed in the n_TOF experimental area. It is around 185 m away from the lead target where neutrons are produced by a 20 GeV/c proton beam. The neutron energy range goes from thermal to >10 GeV. The experiment lasted several months. The challenging α-activity of the ^{240}Pu samples resulted in a mechanical damage of the corresponding micromeshes. The consequence, as explained in Ref. [13], is the deterioration of the electrical field and of the detector gain. Therefore, up to now, just the data obtained with the ^{242}Pu samples could be used and analyzed. Preliminary results were presented for this actinide in Ref. [13] and are shown in Figure 2.3.

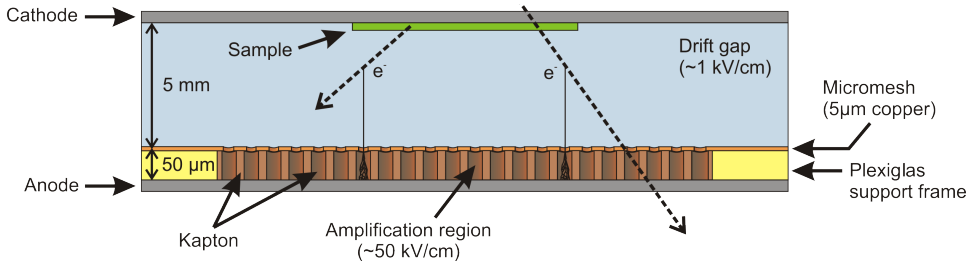

Figure 2.1: Schematic view of part of the Micromegas assembly [14].

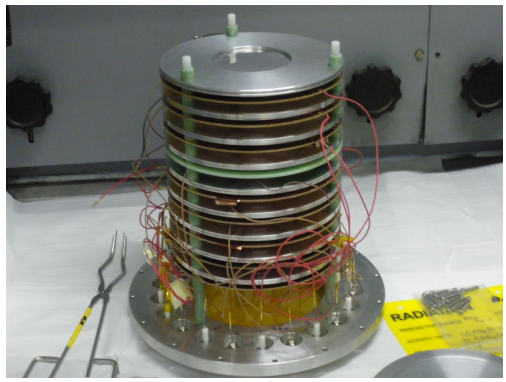

Figure 2.2: The Micromegas assembly [15].

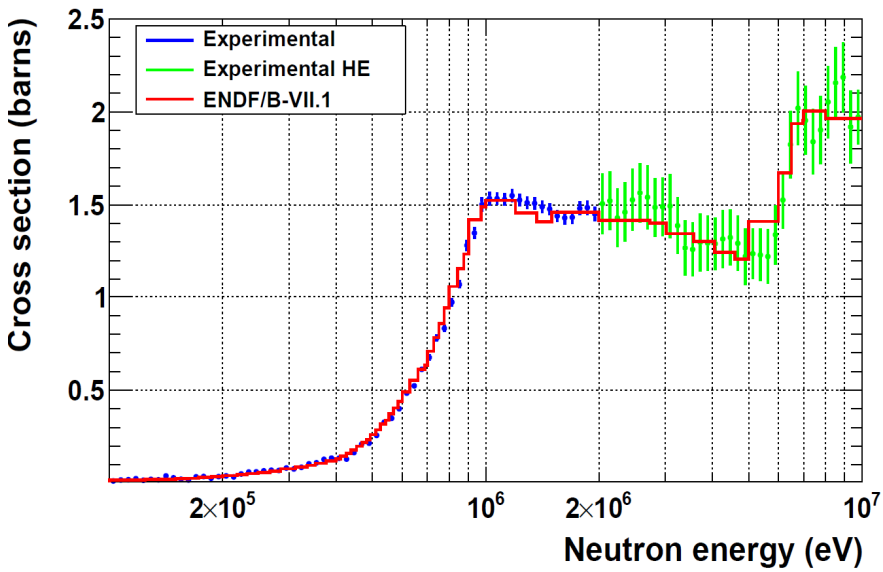

Figure 2.3: Preliminary results of the n_TOF experiment for ^{242}Pu [13].

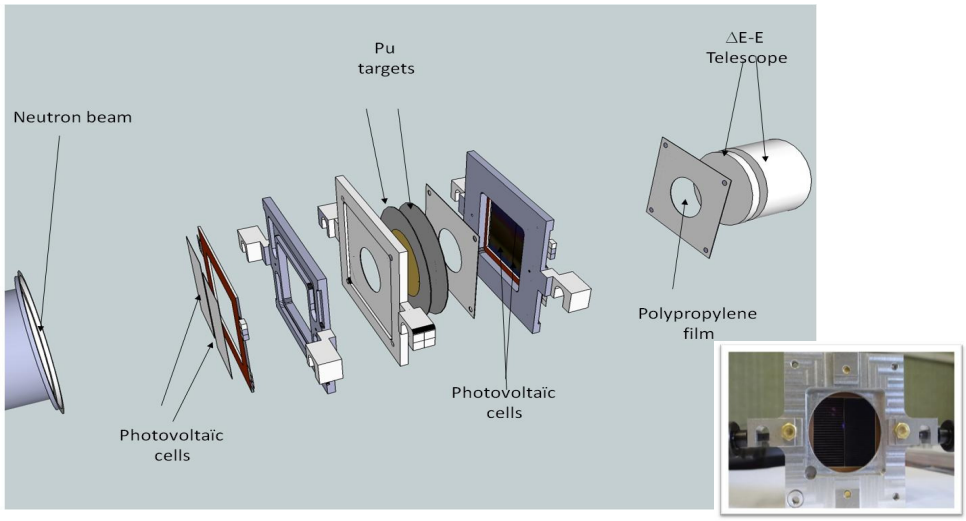

Figure 2.4: Experimental setup of the measurement performed at Bruyères-le-Châtel relative to the ^{1}H(n,p) reaction [13].

2.1.2 ^{240,242}Pu(n,f) measurement at the AIFIRA facility (CNRS)

This experiment uses the same principle as in Ref. [16], where they measured the ^{243}Am neutron-induced fission cross section successfully. There, it was proven that photovoltaic cells could be employed in nuclear physics as fission detectors in on beam experiments, since they do not suffer damage under a neutron beam. The setup proposed was the one in Figure 2.4. The solar cells are used in a sandwich with the two samples, ^{240,242}Pu. The compact geometry gives a geometrical efficiency of around 72% and the photovoltaic cells have an intrinsic efficiency of 95(1)% [13]. Just after the sandwich a polypropylene (PP) film is placed. This film contains mainly hydrogen and the ^{1}H(n,p) reaction is used as a reference. The protons are detected by a proton recoil telescope or a silicon detector. To avoid the overestimation of proton counts due to neutron interaction in other materials surrounding the setup, background measurements were performed by placing a tantalum screen between the PP film and the telescope.

One week of measurement was performed in december 2012 at the 4 MV Van de Graaff accelerator of the BRC-CEA-DIF (Bruyères-le-Châtel). Three energies were measured in the range from 1.1 to 2.0 MeV. The ^{240,242}Pu samples used were produced at JRC-IRMM. Data are currently under analysis. Nevertheless, it was clear already during the first days of the experiment that the cells corresponding to the ^{240}Pu sample were suffering from the high α-activity of the sample (13.2 MBq). The data taken with ^{240}Pu will not be analyzed since there is no visible separation between α-particles and fission fragments in the pulse height spectra.

2.2 The MetroFission experiment

MetroFission [17] is a project of the European Metrology Research Program (EMRP) with the aim of providing new quality data related to the new generation of nuclear power plants. These data are in the area of materials, temperature, neutron fluence, nuclear data and radiometric methods. WP4 is devoted to improve cross sections through neutron metrology. Within this WP the absolute measurement of the neutron-induced fission cross section of ^{240,242}Pu has been performed using a TFGIC with the two samples in a back-to-back geometry at two different national laboratories: the National Physics Laboratory (NPL, United Kingdom) and Physikalisch-Technische Bundesanstalt (PTB, Germany). Data have not been published yet.

2.3 Previous experiments

In this section an overview of the most relevant measurements that have been done since the early 1960s for both isotopes is presented. The experiments where the original publication could not be traced back have been discarded from the text, as well as those where data points were scarce, the ones where data points were not in the region of interest and the ones that were not included in the Experimental Nuclear Reaction Data Library (EXFOR) [18]. Figures 2.5 and 2.6 present for ^{240}Pu(n,f) and ^{242}Pu(n,f), respectively, the experimental data together with the current evaluations from USA (ENDF/B-VII.1 [19]), Europe (JEFF 3.1 [20]) and Japan (JENDL 4.0 [21]). An extended explanation of the figures is given later.

2.3.1 ^{240}Pu(n,f)

Ruddick, 1964

The experiment was performed at a 3-MV VdG accelerator [22]. Neutrons were produced using the ^{7}Li(p,n)^{7}Be reaction, from 60 keV to 500 keV. The measurement was done relative to ^{235}U and the samples were placed in a gas scintillation counter. Both samples were produced by painting from a nitrate solution. The uncertainty listed is around 20%.

White, 1967

The accelerator used was the same as in the previous experiment, but neutrons were produced using the reactions T(p,n), D(d,n) and T(d,n). Four energies were measured: 1.0, 2.25, 5.4 and 14.1 MeV. The measurement was done relative to ^{235}U(n,f) and its stated accuracy is around 2% [23].

Meadows, 1981

The measurement was performed at the Argonne National Laboratory (ANL) Fast Neutron Generator (FNG) using the ^{7}Li(p,n)^{7}Be and D(d,n)^{3}He reactions to cover a neutron energy range from threshold to 10 MeV [24]. A double ionization chamber was used as detector with a back-to-back geometry. The reference sample used was ^{235}U. The samples were produced by molecular plating. Statistical errors can go up to 4.1% and systematic ones up to 4.5%.

Budtz-Jørgensen, 1981

Two accelerators were used to perform this measurement: the 7-MV VdG accelerator and the electron linear (GELINA) accelerator, both at the Central Bureau for Nuclear Measurements (CBNM) - today's JRC-IRMM. An energy range from 10 keV to 10 MeV was covered. The measurements performed at the GELINA facility covered a range from 7 eV up to 2.0 MeV, but only the region from 10 to 300 keV was considered of interest (this region is not covered in the present experiment). Therefore, just the data taken at the VdG facility will be considered hereafter. A parallel plate ionization chamber with a ^{240}Pu and a ^{235}U sample in a back-to-back configuration was used. Both samples were evaporated. The statistical uncertainty listed is up to 2.5% for the measurements at the VdG, the corresponding systematic uncertainty is of 2.3% [25].

Laptev, 2004

The experiment was performed at the neutron spectrometer GNEIS in Gatchina (Russia) [26]. The neutron energy range covered was from 1 to 200 MeV and was determined by time-of-flight. A fast parallel plate ionization chamber with 6 sections was used. ^{235}U was used as a reference sample. The targets were produced using the painting technique. The shape measurement of the ratio ^{240}Pu(n,f) vs ^{235}U(n,f) obtained was normalized with the data of Ref. [27] in the range of 1-2 MeV and then, converted to cross section using the JENDL-3.2 [28] evaluation for ^{235}U(n,f) below 20 MeV. The uncertainty presented is just describing statistics and corresponds to 3%.

2.3.2 ^{242}Pu(n,f)

Butler, 1960

The experiment was done in 1960 at the 3-MV VdG accelerator at the Argonne National Laboratory (USA) [29]. It used a gas scintillation counter with a back-to-back geometry. ^{242}Pu(n,f) was measured relative to ^{235}U(n,f) in the energy range from 0.1 MeV to 1.7 MeV. Both samples were prepared by means of electrodeposition. The plotted uncertainty corresponds just to statistics and is around 3.5%. Systematic uncertainties amount to 5.5%.

Fomushkin, 1970

Dielectric detectors with photographic silicate glass were placed in a vacuum chamber together with layers of ^{242}Pu, ^{235}U and ^{238}U among others [30]. The experiment was carried out using an electrostatic accelerator with a tritium target to produce neutrons. The energy range covered was from 0.45 MeV up to 3.6 MeV. The uncertainty on the cross section values is between 4-6%; this uncertainty does not include the uncertainty on the standard cross section used for normalization.

Bergen, 1970

The technique used for the experiment was a time-of-flight spectrometer that was pulsed using an underground nuclear explosion in May 1968 [31]. The measurement was done relative to ^{235}U(n,f) and both samples were prepared by vacuum deposition. The FF detectors used were p-n diodes. The energy range covered is from 50 eV to 5 keV and from 0.1 MeV to 3 MeV. The overall systematic error is 4.4% below 5 keV and 5.8% above 0.1 MeV.

Auchampaugh, 1971

The neutron source used was the same as for the experiment of Bergen (1970). The ^{242}Pu sample was prepared by vacuum deposition. The FFs were detected as current from fully depleted diffuse-junction Si semiconductor detectors. The normalization was done to ^{6}Li(n,α) below 100 keV and to ^{235}U(n,f) above. The plotted uncertainty corresponds just to statistics, 4% should be added due to systematic errors [32]; this value was updated to 6.2% in EXFOR.

Meadows, 1978

At the Argonne National Laboratory Fast Neutron Generator they used the ^{7}Li(p,n)^{7}Be and D(d,n)^{3}He reactions to produce neutrons covering an energy range from 0.4 MeV up to 10 MeV [33]. The measurement was done relative to ^{235}U(n,f) and the electrodeposited samples were placed back-to-back in a double ionization chamber. The statistical uncertainty ranges from 0.8 to 3.2%, while the systematic one from 1.3 to 1.7%.

Weigmann, 1985

The experiment was performed at the GELINA accelerator at the CBNM [34]. The beam was pulsed and covered an energy range from 2 eV to 10 MeV. The measurement was done with an ionization chamber. The samples used were a ^{242}Pu made by solution-spraying and an ^{235}U sample made by electrodeposition. The presented data show just statistical uncertainties. Systematic uncertainties are calculated to be around 3% above 100 keV.

2.3.3 Common experiments, ^{240,242}Pu(n,f)

Staples, 1998

The experiment was done at the Weapons Neutron Research white neutron source at the Los Alamos National Laboratory. A multi-plate gas ionization detector measured simultaneously the fission rate for each of the isotopic targets (several Pu isotopes and an ^{235}U sample for normalization). The ^{240,242}Pu were produced by electrodeposition. The neutron energies were determined by time-of-flight and the range covered was from 0.5 MeV to 400 MeV. The uncertainty is described to be lower than 4% for energies below 50 MeV [27].

Tovesson, 2009

The measurements were done at the Los Alamos Neutron Science Center (LANSCE) [35]. The time-of-flight technique was used to determine the incident neutron energy. The detector used was a parallel-plate ionization chamber holding six samples (^{239}Pu, ^{240}Pu, ^{241}Pu, ^{242}Pu, ^{235}U and ^{238}U). The samples used were the same as the ones in the experiment of Staples (1998), with the exception of the ^{241}Pu. The later was produced by evaporation. The neutron-induced fission cross section was measured relative to ^{235}U(n,f). Nevertheless, the ^{235}U sample had a slightly different spot size than the Pu samples, and its thickness was only known to about 10%. The measured ^{239}Pu(n,f) cross section at 3 MeV was used to normalize the measured shape and reduce the final uncertainty. The total uncertainty is described to be 3%.

2.3.4 Data comparison and discussion

All the data described in this Chapter have no value if they cannot be compared and plotted together. The aim of this data comparison is to provide a wide overview of the most relevant experiments listed above and compare them with the most recent evaluations. In addition, it is critical to bring a summary of all the uncertainties related to the measurements with the aspiration of providing an outlook of the challenge of meeting the target accuracies requested by the High Priority Request List (HPRL) (see Table 1.2). For a given data set it is even more important to have an extended description of all the uncertainty sources that had an influence on the measurement. Without such information the results provided become meaningless since they lack of a stated accuracy. For cross section measurements several experimental parameters can bring an important contribution to the uncertainty. For instance, fission deposits can have very different homogeneity depending on the production method employed. These inhomogeneities need to be accounted in the overall stated accuracy. The α-activity of the samples, the detection efficiency and the neutron flux normalization can also play a role in the systematic source of uncertainties.

^{240}Pu(n,f)

Figure 2.5 shows all the data described previously together with current evaluations (ENDF/B-VII.1, JEFF 3.1 and JENDL 4.0). For clearness, not all data points are shown. As it is seen, all the evaluations agree in the placement of the first chance fission threshold, nevertheless the JEFF 3.1 evaluation is up to 5% higher than the others in the plateau region. The data from Tovesson (2009) [35] were measured later than any of the evaluation was performed, even though it confirms the most recent evaluation (JEFF 3.1); meanwhile, the other evaluations (ENDF/B-VII.1 and JENDL 4.0) agree better with the other subsets of the data.

The disagreement between evaluations is due to the different methods used to obtain them. For instance, the ENDF/B-VII.1 evaluation has strongly relied on the measurement from Staples (1998) [27]. The JEFF 3.1 evaluation seems to have performed a trial and error procedure using two different codes; this could be the reason why this evaluation was not following any particular set of data when it was presented. Finally, the JENDL 4.0 evaluation was obtained after doing a simultaneous fitting of any subset of experimental data later than 1960 of ^{233,235,238}U(n,f) and ^{239,240,241}Pu(n,f); and after, that result was increased slightly in the region of 500 keV to 10 MeV.

An overview of the experiments listed above and their uncertainty together with the target accuracy requested by the HPRL is given in Table 2.1. Reaching an accuracy of 1.5-2% for the fission cross section of ^{240}Pu has its major challenge on the strong α-activity of the sample; as will be explained in Chapter 3. Very thin samples need to be employed, which translates in longer measuring times. Thus, reaching better statistics is not easy due to the restricted beam times available nowadays. Besides, systematic uncertainties are often driven by the reference sample used to normalize the measurement. From the presented data, not even the most recent measurement performed by Tovesson in 2009 could achieve such low uncertainties.

^{242}Pu(n,f)

Figure 2.6 shows all the data described previously together with current evaluations (ENDF/B-VII.1, JEFF 3.1 and JENDL 4.0). For clearness, not all data points are shown. The ENDF/B-VII.1 and the JENDL 4.0 evaluations are identical. The agreement of these two evaluations with the JEFF 3.1 is perfect in the first fission chance, but is slightly different in the plateau region, where the JEFF 3.1 shows more structure and has a stronger resonance-like peak around 1 MeV. Unmistakable, this evaluation follows the experiment from Weigmann in 1984 [34], yet the data from Tovesson (2009) [35] agree better with JENDL 4.0/ENDF/B-VII.1. The spread of the data, though, is substantially higher than for ^{240}Pu(n,f).

In the case of ^{242}Pu(n,f) the JEFF 3.1 evaluation was obtained by the best fit (using fission barrier parameters, etc.) to the experimental data. Nevertheless, the data used as reference was the one from Weigmann (1984) [34]. As mentioned, the ENDF/B-VII.1 is taken from the JENDL 4.0. The later was coded using most of the data sets presented here.

The α background of ^{242}Pu is less severe than the one of ^{240}Pu, still the uncertainties listed of the measurements are often higher than the ones obtained with ^{240}Pu (see Table 2.2). The large spread on all the subsets of data could be the reason of the 3 to 5% accuracy requested by the HPRL.

Table 2.1: Summary of the uncertainties corresponding to the neutron-induced fission cross section of ^{240}Pu of the literature values presented in Figure 2.5 and the target accuracy requested by the HPRL. The statistical and systematic uncertainties are given where known together with the total uncertainty. (The hyphen indicates a situation where the uncertainty budget of the experiment is not well described; thus, the total uncertainty is taken.)

Experiment	σ_{STAT}	σ_{SYST}	σ_{TOTAL}
Ruddick (1964) [22]	-	-	20%
White (1967) [23]	-	-	3.5%
Meadows (1981) [24]	<4.1%	<4.5%	6.1%
Budtz-Jørgensen (1981) [25]	2.9%	2.3%	3.7%
Staples (1998) [27]	<2%	1.3%	<4%[a]
Laptev (2004) [26]	2-4%	2.8%	3.4-5%
Tovesson (2009) [35]	-	3%[b]	3%
HPRL (2008) [1]			**1.5-2%**

[a] Uncertainty of the reference cross section not included.
[b] This uncertainty is due to the overall normalization and it is not included in the total uncertainty. The combined total uncertainty should be 4.2%.

Table 2.2: Summary of the uncertainties corresponding to the neutron-induced fission cross section of ^{242}Pu of the literature values presented in Figure 2.6 and the target accuracy requested by the HPRL. The statistical and systematic uncertainties are given where known together with the total uncertainty. (The hyphen indicates a situation where the uncertainty budget of the experiment is not well described; thus, the total uncertainty is taken.)

Experiment	σ_{STAT}	σ_{SYST}	σ_{TOTAL}
Butler (1960) [29]	3.5%	5.5%	6.5%
Fomushkin (1970) [30]	-	-	4-6%[a]
Bergen (1970) [31]	-	5.8%	6-7%
Auchampaugh (1971) [32]	≈5%	6.2%	8%
Meadows (1978) [33]	0.8-3.2%	1.3-1.7%	<3.6%
Weigmann (1985) [34]	<1%	3%	3.2%
Staples (1998) [27]	≈1%	1.3%	<4%[a]
Tovesson (2009) [35]	-	3%[b]	3%
HPRL (2008) [1]			**3-5%**

[a] Uncertainty on the reference cross section not included.
[b] This uncertainty is due to the overall normalization and it is not included in the total uncertainty. The combined total uncertainty should be 4.2%.

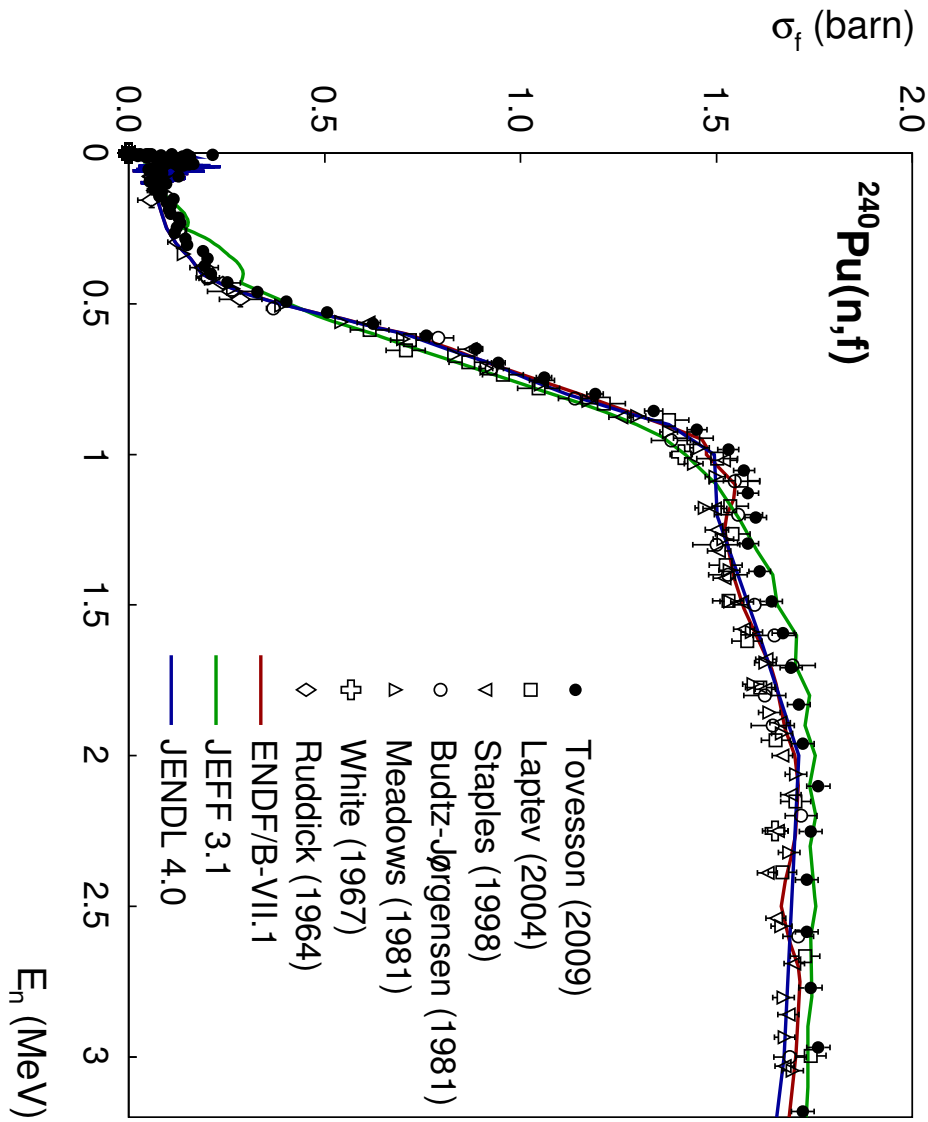

Figure 2.5: Summary of the most relevant experiments performed on the neutron-induced fission cross section of ^{240}Pu compared with current evaluations. The evaluations chosen are: ENDF/B-VII.1 [19], JEFF 3.1 [20] and JENDL 4.0 [21]. The experimental data shown are: Ruddick (1964) [22], White (1967) [23], Meadows (1981) [24], Budtz-Jørgensen (1981) [25], Staples (1998) [27], Laptev (2004) [26] and Tovesson (2009) [35]. Selected data points are shown for legibility of the plot. Data found as a ratio of ^{235}U were normalized to the ENDF/B-VII.1 evaluation of this isotope. Further explanation is given in the text.

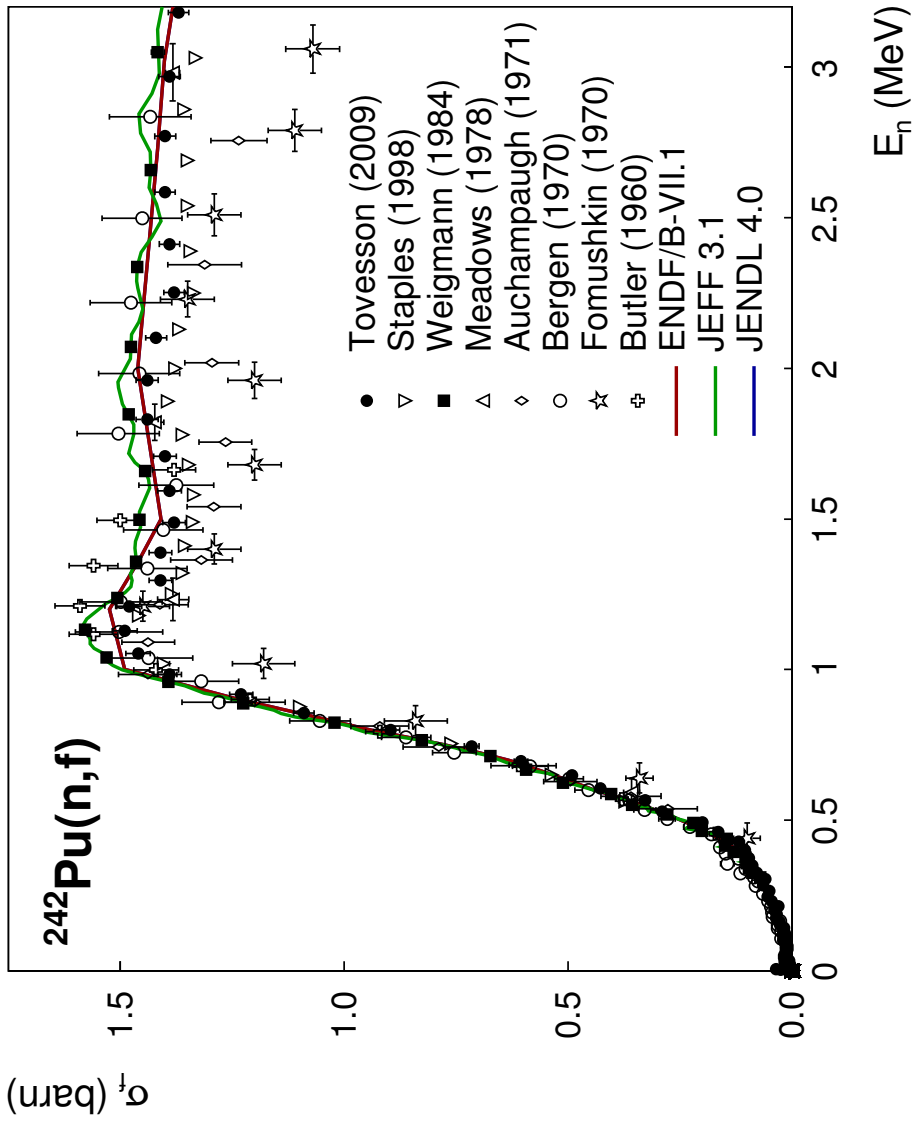

Figure 2.6: Summary of the most relevant experiments performed on the neutron-induced fission cross section of ^{242}Pu compared with current evaluations. The evaluations chosen are: ENDF/B-VII.1 [19], JEFF 3.1 [20] and JENDL 4.0 [21]. The JENDL 4.0 evaluation follows perfectly the ENDF/B-VII.1. The experimental data shown are: Butler (1960) [29], Fomushkin (1970) [30], Bergen (1970) [31], Auchampaugh (1971) [32], Meadows (1978) [33], Weigmann (1984) [34], Staples (1998) [27] and Tovesson (2009) [35]. Selected data points are shown for legibility of the plot. Data found as a ratio of ^{235}U were normalized to the ENDF/B-VII.1 evaluation of this isotope. Further explanation is given in the text.

Chapter 3

Experimental laboratories and techniques

3.1 The Van de Graaff accelerator

All the measurements in this work were done at the VdG accelerator laboratory located at the Institute for Reference Materials and Measurements in Geel (Belgium). The accelerator was built in 1978 as a vertical device with a maximum voltage of 7 MV.

A scheme of the accelerator is plotted in Figure 3.1. The functioning of the accelerator is explained hereafter. Inside the pressure tank positive charges are transported using the belt to charge the terminal to a given voltage. The particles to be accelerated (protons, deuterons or α-particles) are extracted at the high voltage terminal using a gas bottle of the respective gas via an ion source as negative ions. The extracted ion beam is accelerated by the potential difference between the high voltage (HV) terminal and the ground (GND). The beam is steered and focused using beam optics and quadrupole magnets. A bending/analyzing magnet is used to deflect the beam 90° and select just the charged particles that have the desired energy and mass. Thereafter a beam line is chosen and the ion beam is focused using additional beam optics and magnets. At the end of the beam line a neutron producing target is placed. Depending on the neutron energy of interest, different reactions must be used (see Table 3.1).

At the VdG facility of the JRC-IRMM the target hall is subdivided into two levels: one at 4.6 m above ground (5 beam lines) and the other at 0 m (1 beam line). The advantage of using the beam line at 0 m level is that the floor is able to support heavy shielding structures. The experiments presented here have been performed using both levels. To direct the beam to the target hall at 0 m a second analyzing magnet is available at this level.

Table 3.1: Nuclear reactions and their energy regions available at the VdG of the JRC-IRMM.

Nuclear reactions	Neutron energy regions (*mono-energetic region)
^{7}Li(p,n)^{7}Be	E_n: 0 - 5.3 MeV (*0.1 - 0.7 MeV)
T(p,n)^{3}He	E_n: 0 - 6.2 MeV (*0.3 - 3.5/4.5 MeV)
D(d,n)^{3}He	E_n: 2.4 - 10.1 MeV (*2.4 - 7.7 MeV)
T(d,n)^{4}He	E_n: 12.1 - 24.1 MeV (*14.0 - 20.5 MeV)

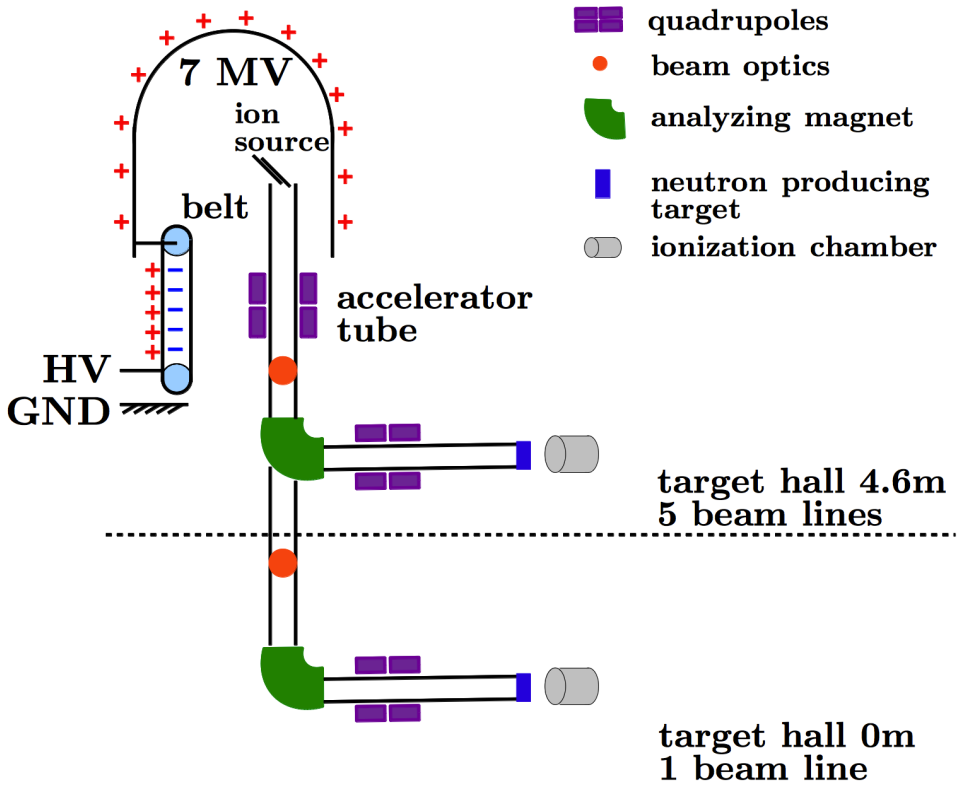

Figure 3.1: Scheme of the Van de Graaff facility at JRC-IRMM.

3.1.1 Neutron production

One of the main advantages of using a VdG accelerator to study cross sections in the fast neutron energy region is the possibility to get very high neutron fluxes at single energies. In the present work protons have been used as charged particles. Even though the proton energy is determined to very high precision, the neutron producing targets have a non-zero thickness that will cause the incoming protons to travel through the target thickness losing some energy. Thus, since the cross section of the proton induced reactions used is not flat in all the energy region and no neutron energy determination is used in these experiments, special care of the neutron spectrum is taken. In Figure 3.2 the neutron flux per cm^2 and second is presented for the two reactions used: ^{7}Li(p,n)^{7}Be (a) and T(p,n)^{3}He (b). The presented data corresponds to a LiF target thickness of 647 $\mu g/cm^2$ in the case of ^{7}Li(p,n)^{7}Be and a TiT target thickness of 1902 $\mu g/cm^2$ for T(p,n)^{3}He, always considering an average beam intensity of 5 μA and the fission deposit to be at a distance of 6 cm from the neutron producing target.

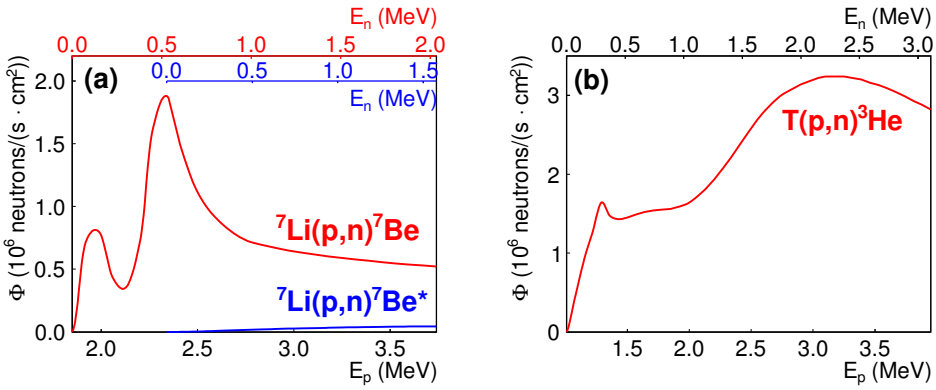

Figure 3.2: Neutron flux spectrum when using (a) the ^{7}Li(p,n)^{7}Be reaction (LiF target thickness of 647 μg/cm^2) and (b) the T(p,n)^{3}He reaction (TiT target thickness of 1902 μg/cm^2). The excited state of the ^{7}Li(p,n)^{7}Be reaction, ^{7}Li(p,n)^{7}Be* starts at a neutron energy of around 0.4 MeV, producing an almost negligible secondary contribution. The data have been taken from the EnergySet code developed at JRC-IRMM [36].

The ^{7}Li(p,n)^{7}Be reaction has an excited state (^{7}Li(p,n)^{7}Be*) with a threshold of about 0.4 MeV, which produces a constant secondary energy background of 0.4 MeV less than the primary state.

In addition, the neutron emission is not fully isotropic. Figure 3.3 presents the differential cross section in the laboratory system ($d\sigma/d\omega$) as a function of the proton energy and the neutron emission angle for the three reactions of interest [37,38]. This effect can produce corrections of up to 3% when actinide samples of different sizes are used or when the samples show inhomogeneities in their thickness.

Li metallic targets

Usually, the lithium neutron producing targets are a compound of lithium fluoride (LiF). Due to the compound, these LiF targets need to have larger thicknesses in order to reach a given neutron flux. In addition, if these LiF targets are irradiated with a proton beam, the interaction with the fluorine will produce high energetic γ-rays. This effect can have a non-negligible contribution to the background when doing γ-ray spectrometry. For this reason, a new set of Li metallic samples were produced at JRC-IRMM. The challenge is that metallic Li is known to diffuse into some material and reacts in air. Because of that, several sandwich samples of metallic Li with Au or LiF were manufactured [39].

The stability in terms of neutron production was tested in one of the experiments. Figure 3.4(a) shows the normalized neutron fluence as a function of irradiation time using three different proton energies. The neutrons produced were calculated from the fissions detected in an ionization chamber which contains two samples: ^{237}Np and

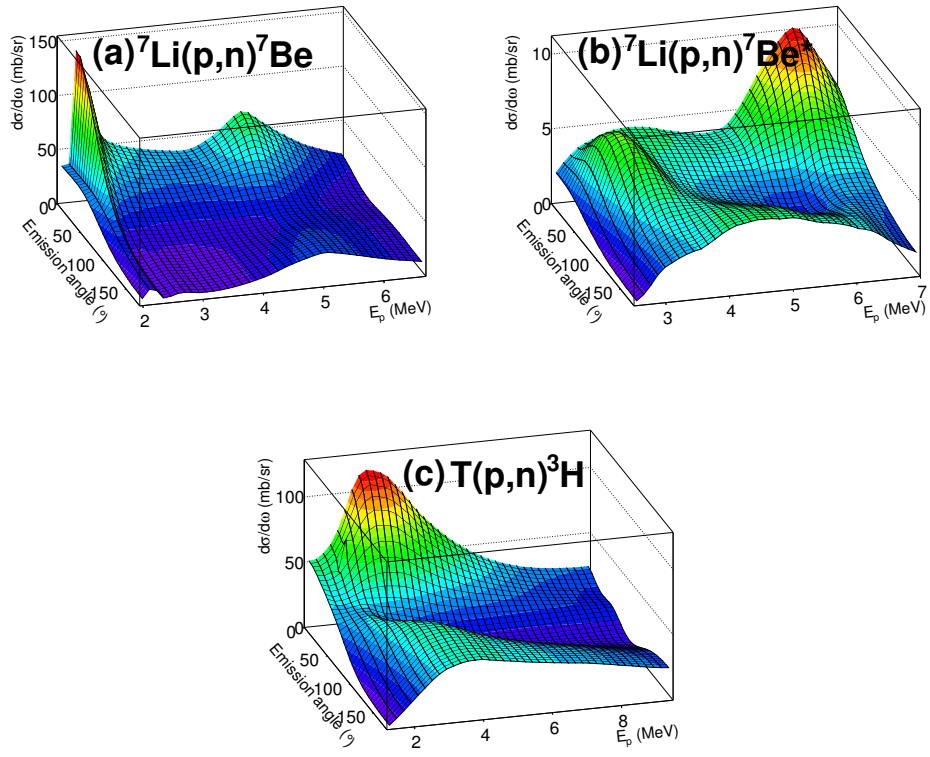

Figure 3.3: Differential cross section in the laboratory system as a function of the proton energy and the neutron emission angle for (a) ^{7}Li(p,n)^{7}Be, (b) ^{7}Li(p,n)^{7}Be* and (c) T(p,n)^{3}He. Data are taken from [37, 38].

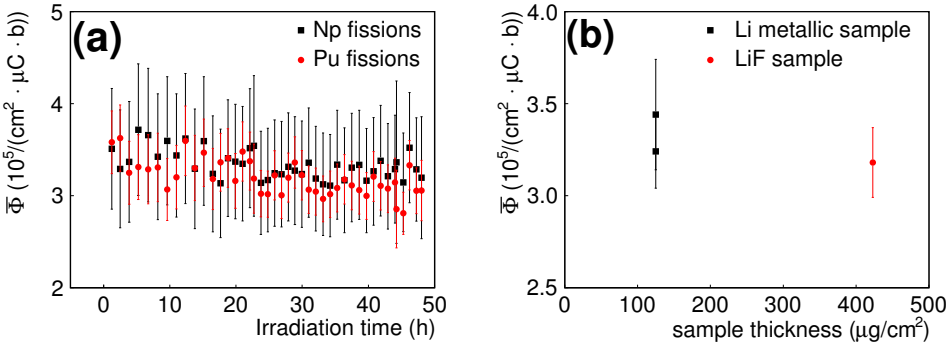

Figure 3.4: Stability test of the Li metallic sample. (a) Stability of the neutron production during irradiation time. (b) Comparison between the normalized neutron fluence of a Li metallic target and a LiF target. The data point shown for the Li metallic target corresponds to different incoming proton energies (2.6 and 2.7 MeV) [39].

^{242}Pu. The proton energy was changed at 22.7 h from 2.6 to 2.7 MeV and at 44.24 h from 2.7 to 3.3 MeV. A fit to the data shows that the neutron production decreased by (9±5)% after 2.5 days of irradiation.

In addition, a comparison of the normalized neutron fluence when using a Li metallic sample and LiF samples was performed (see Figure 3.4(b)), showing that with Li metallic samples it is possible to get the same neutron flux under the same accelerator configuration as with the LiF sample, but with one third of the total Li mass, reducing significantly the neutron energy spread.

The results of this study were published in Paper II.

3.2 Ionization Chamber

An ionization chamber (IC) is a detector where two electrodes are confined in a cylindrical enclosure. The space is filled with a counting gas, such as P10 (90% Ar + 10% CH_4), CH_4, CF_4, ... A sample is placed on one of the electrodes and these are connected to a HV supply to generate an electric field. When the sample has intrinsic activity or emits induced radiation, the emitted particles (i.e. fission fragments or α-particles) will ionize the counting gas along their path generating an ion-electron cloud. Due to the difference in ion mobility, the positive ions can be considered at rest, while the electrons will travel along the field lines towards the positive potential. Nevertheless, the positive ions will induce a charge on the negative potential.

The amount of ion pairs generated will be a property of the counting gas, the type of radiation and its energy. For gases such as Ar or CH_4 a typical value for the energy to create an ion-pair is around 27 eV. If there are no additional loses due to recombination or diffusion, one can assume that the number of ion-pairs generated is proportional to the incident particle energy. This is not completely correct since often the ionizing particles, such as α's or FFs, are not capable to ionize all the gas particles on their track, specially towards the end of the track. These non-ionizing processes contribute to the so-called *Pulse Height Deffect* (PHD). The PHD is a property of the gas used, of the particle and its energy.

3.2.1 Twin Frisch-Grid Ionization Chamber

The determination of the energy and the angle of emission can be important when fission fragment characterization is needed, for this purposes the parallel plate IC needs to be modified by placing a grid between the cathode and the anode plates. This modification of an IC was first introduced by Frisch in 1944 [40] and was named after him. In this work a TFGIC was employed. It consists of two anodes, two grids and a common cathode. The grid will act to shield the anode by dividing the volume

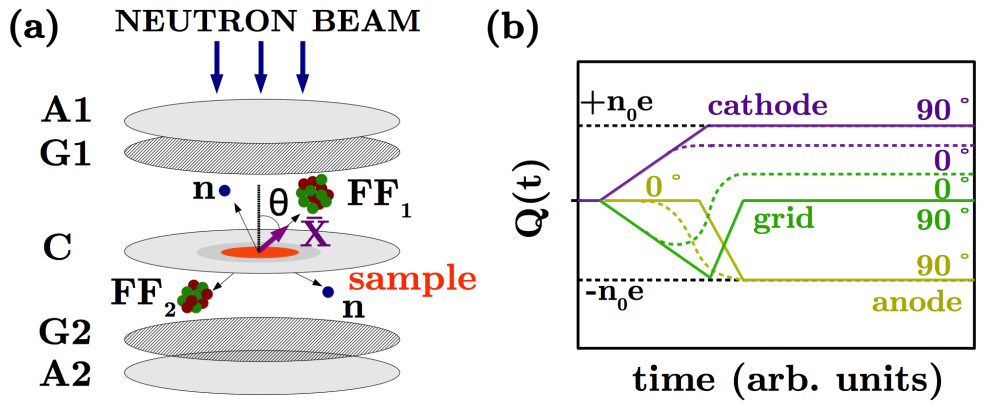

Figure 3.5: (a) Drawing of a TFGIC. (b) Ideal signals detected by a TFGIC at 0°(dotted line) and 90°(full line) emission angle.

into two, thus having two separated electric field regions (see Figure 3.5). Ideally, all the ion pairs will be generated in the cathode-grid electric field region. The electron cloud will travel along the field lines towards the grid inducing a negative pulse, once the cloud has passed the grid electrode all electrons will move towards the anode electrode that has a positive potential. At the same time, a positive charge will be induced on the grid electrode. Since all the electrons, once have passed the grid, will travel the same distance with the same potential difference, the charge induced on the anode electrode will be independent on where those electrons were generated, thus the emission angle of the FF.

The two main properties of a grid are its transparency to the drifting electrons and its opacity to charge induction. The transparency of a grid with parallel wires was described by Bunemann [41] in terms of a field, being this the positive gradient of the electric potential. The transparency (λ) is described by the difference of field lines per unit area in the grid-anode volume leaving the grid (L_{G-A}) and the field lines per unit area of the cathode-grid volume reaching the grid (L_{C-G}). An ideal grid, thus, will have the same number of lines reaching it from the cathode than leaving it towards the anode:

$$1 - \lambda = 1 - \frac{L_{G-A}}{L_{C-G}} \tag{3.1}$$

This will only be possible if the strength of the electric field in the grid-anode volume is higher than the one in the cathode-grid volume. As expressed by Bunemann to reach $\lambda \to 1$ the following condition needs to be fulfilled:

$$\frac{V_A - V_G}{V_G - V_C} \cdot \frac{D_{C-G}}{D_{G-A}} \geq \frac{1 + \rho \cdot \left[1 + \frac{d}{4\pi \cdot D_{G-A}}(\rho^2 - 4\ln\rho)\right]}{1 - \rho \cdot \left[1 + \frac{d}{4\pi \cdot D_{C-G}}(\rho^2 - 4\ln\rho)\right]} \tag{3.2}$$

where V_i is the voltage applied to the electrode i (cathode, anode or grid), D_{i-j} the distance between the electrodes $i-j$, d is the distance between grid wires and $\rho = 2\pi r/d$, with r being the grid wire radius.

The anode electrode will collect a charge proportional to the number of electrons generated,

$$Q_{\mathrm{A}} = -n_0 e \tag{3.3}$$

where n_0 is the sum of all electron contributions from the ion pairs. The induced charge on the cathode will have, in addition, a contribution corresponding to the place where the charges were originating,

$$Q_{\mathrm{C}} = -n_0 e\left(1 - \frac{\bar{X}}{\mathrm{D}}\cos\theta\right) \tag{3.4}$$

where $\bar{X}$ is the centre-of-gravity of the electron-cloud distribution and D is the cathode-grid distance. Finally, the signal induced on the grid will be:

$$Q_{\mathrm{G}} = n_0 e\frac{\bar{X}}{\mathrm{D}}\cos\theta \tag{3.5}$$

The charge collected by the anode electrode needs to be corrected to account for the incomplete transparency of the grid, the so-called grid inefficiency (σ, GI),

$$Q^*_{\mathrm{A}} = -n_0 e\left(1 - \sigma\frac{\bar{X}}{\mathrm{D}}\cos\theta\right) \tag{3.6}$$

A recent investigation proved that the charge induced on the anode needs to be corrected for the GI by using the extended additive approach [42, 43],

$$\mathrm{P}^{\mathrm{corr}}_{\mathrm{A}} = \frac{\mathrm{P}^*_{\mathrm{A}} - \sigma\cdot\mathrm{P}_{\mathrm{C}}}{(1-\sigma)} \tag{3.7}$$

where the pulse heights $\mathrm{P}^*_{\mathrm{A}} = Q^*_{\mathrm{A}}$ and $\mathrm{P}_{\mathrm{C}} = -Q_{\mathrm{C}}$. The GI for a TFGIC with a parallel-wired grid is given by:

$$\sigma(r, d, D_{A-G}) = \left(1 + \frac{D_{A-G}}{d/2\pi((\rho^2/4) - \ln\rho)}\right)^{-1} \tag{3.8}$$

With the geometry of the TFGIC used in this work $\sigma \approx 0.03$; considering $D_{A-G} =$ 6 mm, $r = 0.05$ mm and $d = 1$ mm.

3.2.2 Gases used, potential applied and pressure

A TFGIC can work under a wide range of parameters in terms of gas, potential applied and pressure. These three parameters are correlated and for a given experiment a choice has to be made. A starting point, in the particular case of this work, was the fact that the TFGIC available was not designed to work under vacuum conditions or over pressure. Therefore, a pressure close to the atmospheric one was preferred. Concerning the HV to be applied to each electrode there are three restrictions and one condition that needs to be fulfilled. The restrictions are:

1. The HV applied must be lower than the preamplifier voltage limit (in the present case ± 3 kV).

2. The HV applied must be lower than the maximum of the HV supply box (in the present case ± 5 kV).

3. The electric field applied between the electrodes needs to be such to prevent discharges within the gas volume. Thus, it is needed to keep the HV below the breakdown voltage[1].

And the condition is:

1. The HVs of each electrode needs to fulfill the condition implied by equation 3.2; thus, for the parameters choice in this case, the field strength between the grid-anode space must be at least twice as large as the one of the grid-cathode space. In that way, the field lines reaching and leaving the grid are almost the same and the electron loses on the grid are minimized.

The choice of the use of one or the other counting gas needs to be made with the main consideration of its drift velocity. In this experiment the consequence of having a gas with a large PHD is almost irrelevant, since the main purpose is to perform cross section measurements and not FF characterization. Two gases were used during this work: P10 (90% Ar and 10% CH_4) and CH_4. The experiment started using P10 as counting gas. The motivation at one point to change from one to the other counting gas will be explained in detail in Chapter 5. The parameters applied when employing each gas are listed in Table 3.2. Figure 3.6 shows (a) the drift velocity as a function of the reduced field strength and (b) the breakdown voltage (V_B) as a function of the pressure and the distance between electrodes. The HV applied to each electrode was chosen, besides the conditions explained before, taking into account that the most stable conditions to work with would be in a stable region of the drift velocity function and the pressure range that could be set in the chamber.

[1]The voltage applied to the chamber electrodes needs to be such that discharges in the detector

Table 3.2: Potential applied, pressure used and field strength as a function of the counting gas employed. Drift velocity and breakdown voltage are as well presented for a cathode-grid distance of 31 mm and a grid-anode distance of 6 mm.

Gas	Gas flow (ml/min)	Pressure (kPa)	HV_C (kV)	HV_G (kV)	HV_A (kV)	Reduced field strength (V/m·Pa)	Drift velocity (10^5 m/s)	V_B (kV)
P10	≈ 50	105	-1.5	0	1.0	≈0.44	≈0.5	>10
CH_4	≈100	105	-2.5	0	1.5	≈0.79	≈1.0	>10

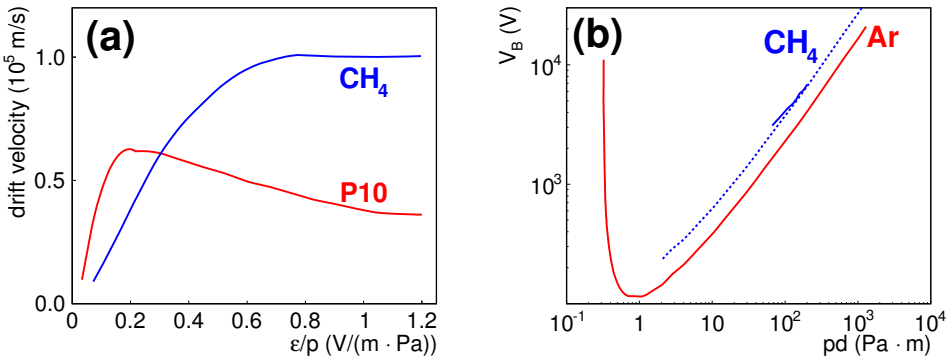

Figure 3.6: Drift velocity (a) and breakdown voltage (b) of CH_4 and P10. (a) Data taken from Ref. [44]. In (b) P10 has been considered as Argon [45]. The data from CH_4 is experimental and is taken from Ref. [46]; the dotted line is an extrapolation of the data considering the same shape as for Argon.

3.3 Experimental setup

The experimental setup consisted of the TFGIC described in Section 3.2.1. All the electrodes were connected to charge or current preamplifiers and these were fed into 12 bit 100 MHz WFD (see Figure 3.7). The cathode signal was used, as well, for triggering the system. Thus, it was split just before the WFD: one signal was connected to the WFD and the other was treated with a Timing Filter Amplifier (TFA) and a Constant Fraction Discriminator (CFD). The WFD was plugged into a computer were all the raw signals were recorded. Usually, a trace was recorded for 10 μs: 5 μs pre- and 5 μs post-trigger.

Cross section measurements can be performed in two different ways using TFGICs: absolute and relative. Absolute measurements are performed by placing a sample on the cathode of the TFGIC and a neutron counter aligned with the chamber. The counts in the TFGIC will be normalized by the neutron flux determined by the neutron

are avoided. Discharges happen in a gas when the breakdown potential is reached. This potential can be determined by the Paschen's law and it is a function of the gas used, the pressure applied and the distance between electrodes.

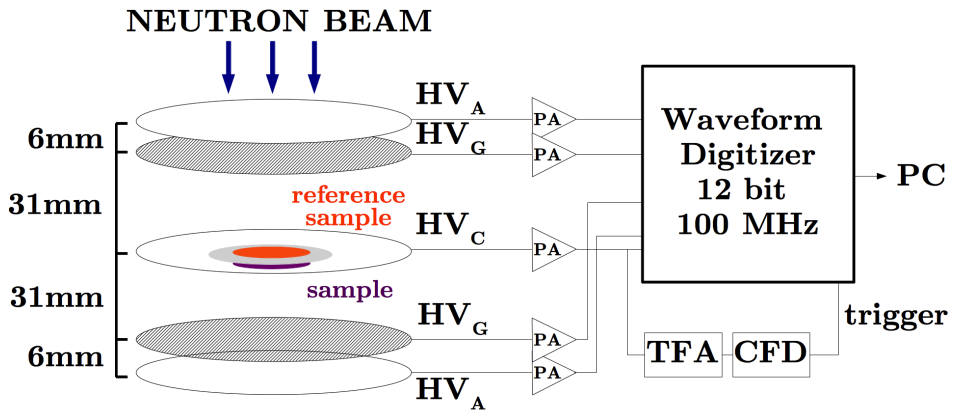

Figure 3.7: Experimental setup for a cross section measurement.

counter. The disadvantage of using this method is that the neutron counter cannot be placed at the same position as the fission detector; as a result, geometric corrections must be applied to properly determine the flux. In addition, it is needed to quantify the amount of neutrons scattered in the target hall that are being detected by the counter but do not have the proper energy. Relative measurements are performed using a back-to-back configuration. Two non-transparent samples are placed on the cathode of the TFGIC, each of them facing one side of the chamber. One of the samples will be the one under study and the other a reference sample. The latter should have a well-known cross section to reduce uncertainties in the normalization of the unknown cross section.

All the measurements within this work were done with a back-to-back configuration. Three different reference samples have been used: ^{237}Np, ^{238}U and ^{235}U.

A picture of the TFGIC aligned with the beam line and the neutron producing target can be seen in Figure 3.8.

Experiment with ^{235}U samples

The measurement of the two samples of interest, ^{240,242}Pu, relative to ^{235}U(n,f) needed to be taken with special care. ^{235}U being a fissile isotope has orders of magnitude higher fission cross section in the thermalized neutron energy region than at the fast neutron region. The scattering of the fast neutrons on the target hall walls and the rest of the material in the target hall can thermalize these neutrons and, thereafter, reach the TFGIC producing an increased amounts of counts in the reference sample side. To avoid this effect a shielding was build around the TFGIC.

The shielding consisted in a first layer of B_4C and a second layer of paraffin. The paraffin is a well-known neutron moderator. Therefore, if a neutron passes the wall, it

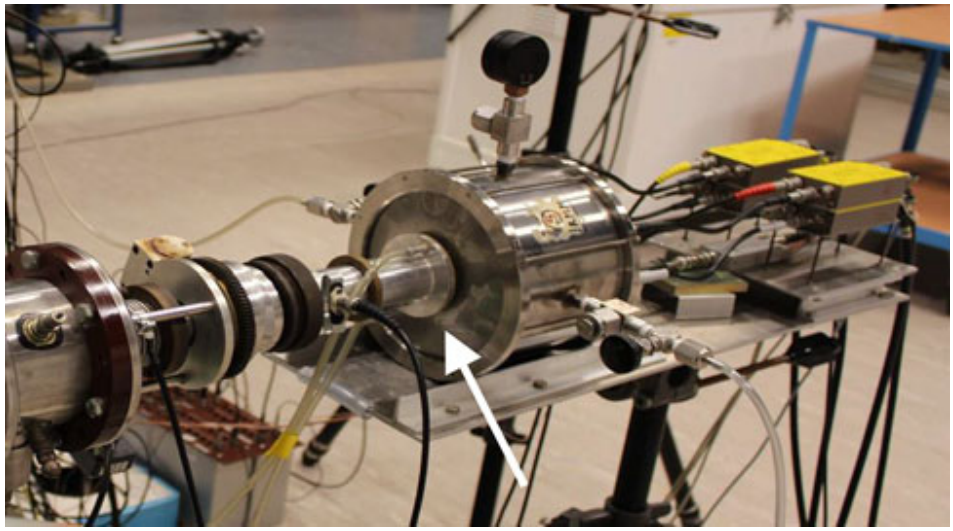

Figure 3.8: Picture of the beam line with the neutron producing target at the end and the TFGIC centered with it. The arrow indicated the position of the neutron producing target. Courtesy of D. Vanleeuw.

will be moderated once by the paraffin block and, if it scatters and enters again, it will be moderated a second time. Then, the B_4C will most likely capture this thermalized neutron since the neutron capture cross section for ^{10}B is around 10^5 barns at these energies.

The drawback of using a shielding close to the TFGIC is that neutrons might get back scattered towards the detector with lower energies than the initial one, but still in the MeV region. For this reason, Monte Carlo simulations of the neutron spectrum were performed with MCNP [47]. These simulations and the corresponding corrections will be explained in Chapter 6. In Figure 3.9 the experimental setup with the shielding is presented.

Influence of the setup in the neutron spectrum

Finally, the neutron spectrum can be degraded after the neutron producing target by the water cooling setup used to lower the heat in the neutron producing target, the target can and by the stainless steel chamber structure. When neutron-induced fission cross section ratios of two isotopes with a similar fission threshold and shape are being measured, this influence is almost negligible. But, in the other case, when a fissile isotope is used or the two isotopes in the chamber have a difference of hundred keVs in the position of the fission threshold, this correction can be crucial. For this reason, MCNP simulations were performed in order to correct the data by the distortion of

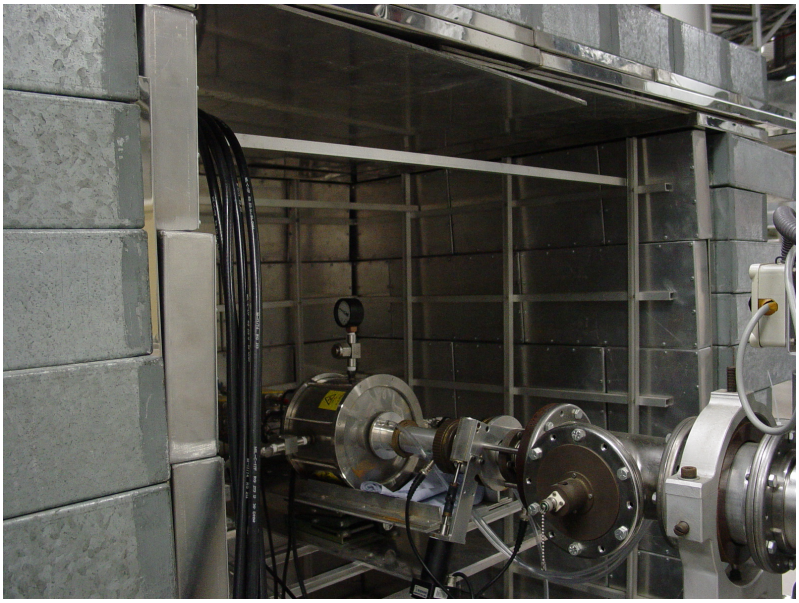

Figure 3.9: Picture of the beam line with the neutron producing target at the end, the TFGIC and the shielding structure around it.

the neutron spectra due to the experimental setup between the neutron producing target and the samples under study. The corrections will be explained in Chapter 6 together with the simulations of the shielding structure.

3.4 Sample description

Several samples were used for this work, all of them made in the Target Preparation laboratory of the JRC-IRMM. The plutonium samples were made specifically for this project, therefore the optimum mass could be chosen in order to minimize the background activity (α-particles). The reference samples were available already at the facility. A detailed description of all samples is presented in Tables 3.3, 3.4 and 3.5. A picture of the ^{242}Pu sample and the TFGIC opened with two samples placed on the cathode can be seen in Figure 3.10.

The Pu samples used in this experiment were produced by the so-called *molecular plating* technique. The Pu layers have a diameter of 29.95 mm (0.1%) and are deposited on an Al backing with a thickness of 0.25 mm and a diameter of 50 mm. Due to the short α half-life of the ^{240}Pu of 6561 yr (0.1%), the sample has been made in order to minimize its α-activity. Thus, the ^{240}Pu sample has a mass of 92.9 μg (0.4%) and an α-activity of 0.8 MBq (0.4%). The ^{242}Pu has an α half-life longer than 10^5 yr, for this reason more material could be deposited on top of the disk, being its mass

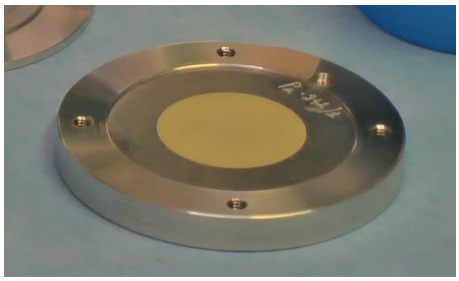

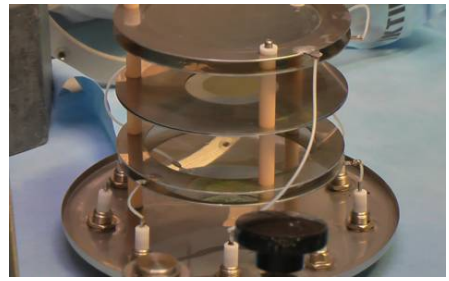

Figure 3.10: Left: picture of the ^{242}Pu sample. Right: picture of the TFGIC open with two samples on the cathode holder.

Table 3.3: Main characteristics of the ^{240,242}Pu samples [48]. The mass, areal density and α-activity are given for the main isotope of the sample. All the uncertainties are expanded with a coverage factor $k = 1$. The expanded uncertainty of the sample purity has a coverage factor $k = 2$.

	^{240}Pu	^{242}Pu
Method	molecular plating/electrodeposition	
Chemical composition (assumed)	$Pu(OH)_4$	$Pu(OH)_4$
Total mass (μg) (calculated)	119.22 (0.4%)	859.54 (0.9%)
Diameter (mm)	29.95 (0.1%)	29.95 (0.1%)
Total areal density (μg/cm^2) (calculated)	16.9 (0.4%)	122 (0.8%)
Backing	aluminum	aluminum
Mass (μg)	92.9 (0.4%)	671 (0.9%)
Areal density (μg/cm^2)	13.19 (0.4%)	95.3 (0.8%)
α-activity (MBq)	0.780 (0.4%)	0.0984 (0.3%)
% ^{238}Pu	0.0733 (*29*)	0.002719(*51*)
% ^{239}Pu	0.0144 (*18*)	0.00435 (*18*)
% ^{240}Pu	99.8915 (*18*)	0.01924 (*23*)
% ^{241}Pu	0.00041 (*31*)	0.00814 (*31*)
% ^{242}Pu	0.02027 (*41*)	99.96518 (*45*)
% ^{244}Pu	0.000046(*88*)	0.00036 (*13*)

of 671 μg (0.9%) and its α-activity of 0.1 MBq (0.3%). Although the accuracy on the determination of the α-activity is smaller, the main contribution on the mass uncertainty of ^{242}Pu is due to its uncertainty of the α half-life, 3.75×10^5 yr (0.5%). The activity of both samples was determined by defined solid angle α-particle counting. Their mass was calculated from the activity. The purity of the samples is higher than 99.8% and their atomic abundances were measured by mass spectrometry. To quantify the amount of fission fragments that will be fully stopped in the sample it is important to know the total sample mass. Assuming that the Pu deposits are hydroxide in the form of $Pu(OH)_4$, the measured Pu areal density was used to calculate the total areal density of the deposit. This increases the absolute sample thickness by about 28%.

Table 3.4: Main characteristics of the reference samples ^{237}Np and ^{238}U used [49, 50]. The mass, areal density and α-activity are given for the main isotope of the sample.

	^{237}Np	^{238}U
Method	vacuum deposition	
Chemical composition	NpF_4	UF_4
Total mass (μg) (calculated)	516.7	761.5
Diameter (mm)	12.7	30
Total areal density (μg/cm^2) (calculated)	408	107.7
Backing	aluminum	transparent
Mass (μg)	390.3 (0.3%)	577.2 (0.4%)
Areal density (μg/cm^2)	308.1 (0.3%)	81.7 (0.4%)
α-activity (Bq)	10168 (0.1%)	7.19 (0.4%)
Isotopic content	99.76% ^{237}Np 0.24% ^{238}Pu	99.998% ^{238}U <0.02% ^{234}U

The reference samples used were prepared by the vacuum deposition technique. Unfortunately by the time of performing the very first experiment the ^{237}Np sample of the same diameter as the Pu samples broke. Thus, a ^{237}Np sample with a much smaller spot size had to be chosen. As it can be seen in Table 3.4, the ^{237}Np sample is thicker than the rest, therefore the correction for FFs loss in the sample will be higher as well. The ^{237}Np sample mass was remeasured by low-geometry α-counting at the Radionuclides laboratory of the JRC-IRMM [49], providing a mass uncertainty smaller than 1%. The ^{238}U sample mass was remeasured using a single Frisch-Gridded Ionization Chamber, this method is explained later on. The other samples employed in this work are listed in Table 3.5.

3.4.1 Measurement of the ^{238}U sample mass

The original certificate of the ^{238}U sample used in these experiments had an uncertainty in its mass of 5%. In view of the higher target accuracies requested by the NEA on the neutron-induced fission cross section of interest in this project, the mass of the sample was re-measured with the aim of lowering its uncertainty.

A Single Frisch-Gridded Ionization Chamber was employed as a particle detector. The sample was positioned at the cathode, facing the grid and the anode. A pressure of 120 kPa was set and P10 was used as counting gas with a gas flow of around 80 ml/min. The HV applied was -0.7 kV to the cathode and 0.25 kV to the anode; the grid was grounded. The data were stored in 200 MHz waveform digitizers and analyzed offline afterwards [50]. There are two advantages of using this technique to determine the mass compared to a low geometry α counting. First, the solid angle covered here is nearly 2π, thus high statistics are reached in a short measuring time. Second, there is no dependence on the position of the sample on the cathode plate with respect to the anode. The technique was already proved satisfactory in Ref. [52].

Table 3.5: Main characteristics of the reference samples of ^{235}U used [50, 51]. Three different samples of this isotope were used, they have been labelled in the first row. The mass, areal density and α-activity are given for the main isotope of the sample.

	^{235}U (#6)	^{235}U (#2)	^{235}U (#1)
Method		vacuum deposition	
Chemical composition	UF_4	UF_4	UF_4
Total mass (μg) (calculated)	884.9	894.3	776
Diameter (mm)	30	30	28
Total areal density (μg/cm^2) (calculated)	125.2	126.5	126
Backing	transparent	transparent	stainless steel
Mass (μg)	653 (1.5%)	660 (1.5%)	584 (2%)
Areal density (μg/cm^2)	92.4 (1.5%)	93.4 (1.5%)	94.8 (2%)
α-activity (Bq) (^{234}U & ^{235}U)	2657 (0.4%)	2657 (0.4%)	265.7 (2.1%)
Isotopic content	97.663(*3*)% ^{235}U 1.6582(*17*)% ^{234}U 0.1497 (*5*)% ^{236}U 0.5296 (*6*)% ^{238}U	97.663(*3*)% ^{235}U 1.6582(*17*)% ^{234}U 0.1497 (*5*)% ^{236}U 0.5296 (*6*)% ^{238}U	99.475(*4*)% ^{235}U 0.1698 % ^{234}U 0.0273 % ^{236}U 0.3277 % ^{238}U

Figure 3.11(a) depicts a two dimensional anode versus grid distribution. Clearly the main peak is visible corresponding to the α-line of ^{238}U of around 4.2 MeV. In addition a tailing of α-particles can be seen at low grid values; these correspond to α-particles that have lost most of their energy inside the sample or have been emitted in opposite direction and afterwards backscattered into the detection volume. By doing the projection of the anode signal towards the grid axis, the cosine distribution can be obtained (see Figure 3.11(b)). If now one extrapolates the level of the distribution from $0.5 \geq \cos\theta \leq 0.9$ towards $\cos\theta = 0$, the true number of α-particles emitted in 2π is obtained. After correcting by the dead time of the acquisition software and using the α half-life of ^{238}U the sample mass obtained is 577.2 μg (0.4%). The uncertainty considered is statistical and systematic. The latter is mainly affected by the fitting of the cosine distribution and the determination of the half height of the cosine distribution at $\cos\theta = 1$. The value obtained here is in agreement with the one obtained by low geometry α-counting [51]; 577 μg (2.7%).

3.4.2 Measurement of the ^{235}U (#1) sample mass

Using the same method as for the determination of the ^{238}U sample mass, the mass of the ^{235}U (#1) sample was measured. The main challenges were due to the complexity of the α-decay of ^{235}U, the shorter half-life of ^{234}U compared to ^{235}U ($T_{1/2}(^{234}\text{U}) =$

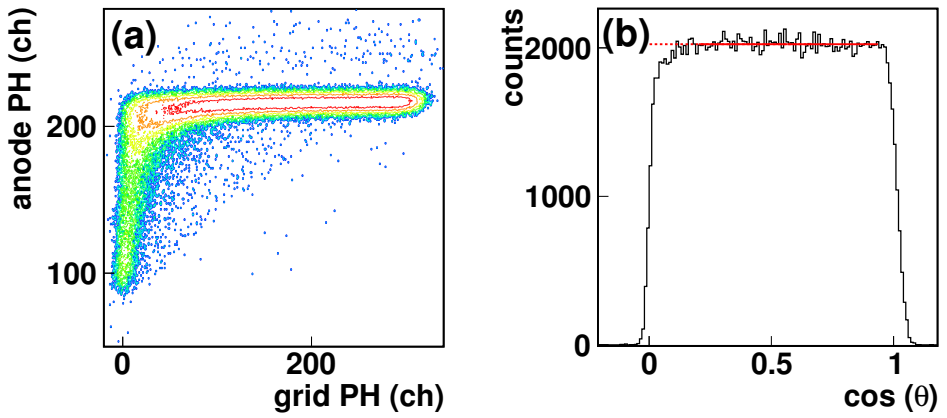

Figure 3.11: Determination of the ^{238}U sample mass. (a) 2D distribution of the anode vs grid pulse height. (b) Cosine distribution of the α-particles in 2π.

$2.46 \cdot 10^5$ y; $T_{1/2}(^{235}\text{U}) = 7.04 \cdot 10^8$ y) and the small energy difference between the main α-lines of ^{234}U ($\approx$4.7 MeV) and ^{235}U ($\approx$4.4 MeV). By searching different literature sources, it has been found that there is a difference of around 2% on the probability of the overall α-decay branches for this isotope. By using the data of Ref. [53], the amount of α-lines that were within the region of interest was 85.19%. After obtaining the cosine distribution and correcting by the isotopic content of the sample (99.475% of ^{235}U) the sample mass was determined to be 583.7 μg (2%) [50].

3.4.3 Vacuum deposition vs electrodeposition

The vacuum deposition technique consists in evaporating the solution in a vacuum chamber that has at the top a sample holder. There the backing of the sample is placed. During all the process the backing is rotating, reaching a high homogeneity of the sample.

Instead, *molecular plating* consists of an electrodeposition at a constant voltage. In the specific case of the ^{240,242}Pu samples a cathodic deposition of Pu onto Al substrates from isopropanol was made [48]. A rotating platinum grid was used to mix the electrolyte without disturbing the deposition.

Figure 3.12 shows fluorescence images of the ^{237}Np, ^{240}Pu and ^{242}Pu samples. It is clear that the sample produced by vacuum deposition (^{237}Np) presents a higher homogeneity than the two ^{240,242}Pu produced by electrodeposition. To account for the mass distribution on the ^{240,242}Pu samples, a scanning was performed by Ref. [51]. The scan consisted of placing a mask of 6 mm diameter on top of the target at 6 different points, a central one and 5 in an outer layer, and calculate the α-activity at

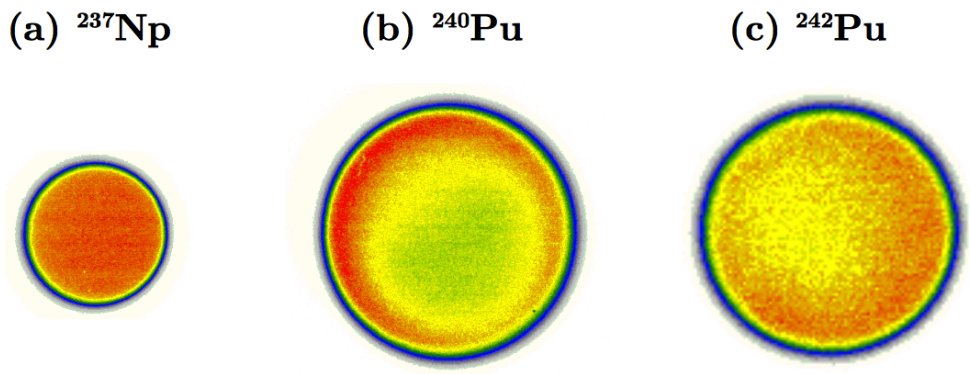

Figure 3.12: Fluorescence images of the ^{237}Np sample, the ^{240}Pu sample and the ^{242}Pu sample. The ^{237}Np sample presents a homogeneous distribution of its mass, while the ^{240,242}Pu have more mass in the outer layer [55].

each point. Then, the count rate at each point was normalized to the central one. An extended description of this technique can be found in Ref. [54]. The results pointed out that the outer layer of the ^{240}Pu had on average 11.4% more mass than the inner one, and for the ^{242}Pu the difference was 7.4%. This mass difference needs to be taken into account in the cross section analysis.

Chapter 4

Data acquisition and digital signal processing

4.1 Data acquisition

The data acquisition system (DAQ) consisted of three Spectrum M2i WFD cards [56] connected via PCI slots to the computer. Each of them had two channels and a trigger input. In total six signals were recorded: two anodes, two grids, a cathode and the trigger signal. The trigger was generated by the cathode signal, using an external discriminator, and then connected to all boards, as explained in Chapter 3.

The acquisition system was developed at JRC-IRMM by Refs. [57] and [58]. The DAQ code was created to work with a variety of digitizer cards from several brands and was fully integrated with the `ROOT` framework [59]. After the program started, it first read the information from the cards, initialize them and finally configure all parameters. Several acquisition preferences could be chosen, such as size of the files, length of the traces, trigger position and delay ...

The recorded data were stored in the computer memory in a binary data format including additional information, allowing a later reconstruction of the traces. After recording the events, the data were stored on a hard disk. During this time the system was not capable to register any event, causing a dead time of around 2 s for a 20 MB file size. The stored data files were then read out by another program for offline data analysis (display), also developed at JRC-IRMM by Refs. [57] and [58]. The offline data analysis program was written in `c++` [60], using the `ROOT` framework [59] and compiled with a specially designed digital signal processing (DSP) library. In the display program each signal was represented as a histogram in `ROOT` and analyzed event by event. The flexibility of the code allowed the user to implement their own functions, optimizing the analysis of the raw data. A scheme of the procedure explained is displayed in Figure 4.1.

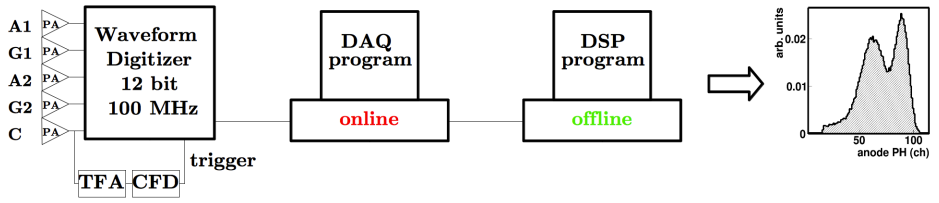

Figure 4.1: Scheme of the process followed to record and analyze the data (following Figure 3.7). The charge collection by the electrodes was sampled with the waveform digitizer. The DAQ program was initializing the digital boards, acquiring and storing the data. An offline analysis program based on a DSP was employed to perform an offline analysis of the stored events; obtaining all relevant information related to the traces.

4.1.1 Treatment of the signals

The data recorded directly from the detector had to be treated prior to the analysis. The method applied to the raw signals is listed henceforth. For all the steps two signals will be presented: an anode and a grid. The event corresponds to a ^{242}Pu trace at 2.0 MeV and using P10 as counting gas.

Figure 4.2 shows the charge collected by the anode (a) and by the grid (b) after their corresponding charge preamplifiers. Each signal was sampled with 100 MHz. The length of the signals was of 1024 channels and the trigger was positioned at channel 512, thus having 512 channels pre-trigger and 512 channels post-trigger. Each channel corresponded to 0.01 μs.

There are several corrections to the signal that have to be applied before extracting the pulse height (PH) information. Some of these corrections can be already seen from the raw signals presented in Figure 4.2. For instance, the α pile-up present in the base line of both traces is visible or the ballistic deficit can be seen as a reduction in signal height in the last part of the anode signal.

Baseline correction

The baseline correction is applied to the raw signals just to shift the entire trace that it starts at 0 mV. Figure 4.3 displays the two signals baseline corrected; the anode signal (a) has been also inverted. In the case of high count rates, including the background, special attention needs to be payed to correct for the baseline not at the beginning of the full track, but just before the FF event. The value for the correction is calculated as an average value of around 100 samples before the FF event.

The baseline shift is mainly due to the incomplete discharge of the preamplifiers [61].

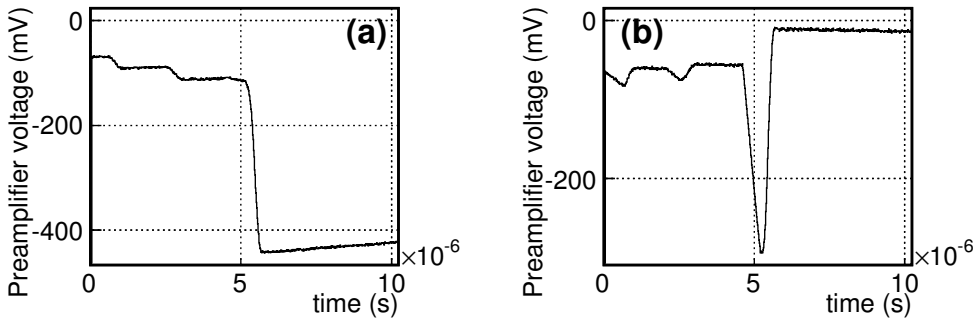

Figure 4.2: Charge collected by the anode (a) and grid (b) sampled with 100 MHz for an event of the ^{242}Pu using P10 as counting gas.

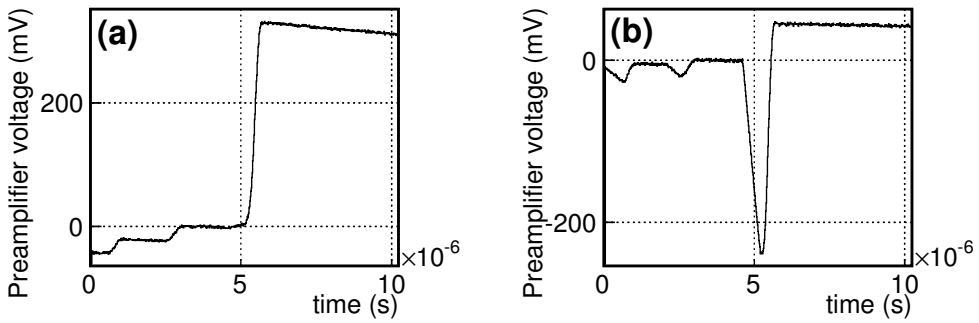

Figure 4.3: Baseline corrected anode (a) and grid (b) signals for the same event as presented in Figure 4.2.

Ballistic deficit and α background correction

Two effects had a strong influence on the collection of charges in this experiment. The first one was the ballistic deficit. This effect can be easily understood by the fact that the discharge of the preamplifier starts just after the first charges reached the electrode. Despite having a large shaping time constant, the charge collection rise time is around 1 μs when using P10 as counting gas, thus the discharge of the preamplifier starts well before all the charges generated by the FF have been collected. The slope of the FFs signals is corrected by differentiating the pulse with the decay time constant (the output signal is shown in Figure 4.4).

After the differentiation the position of the center of the signal slope can be determined. Next, the signal is being integrated. Starting at the center of the slope an iterative code is run upwards and downwards checking the change of slope. In the event of an α pile-up at the very beginning or ending of the FF slope, the code is

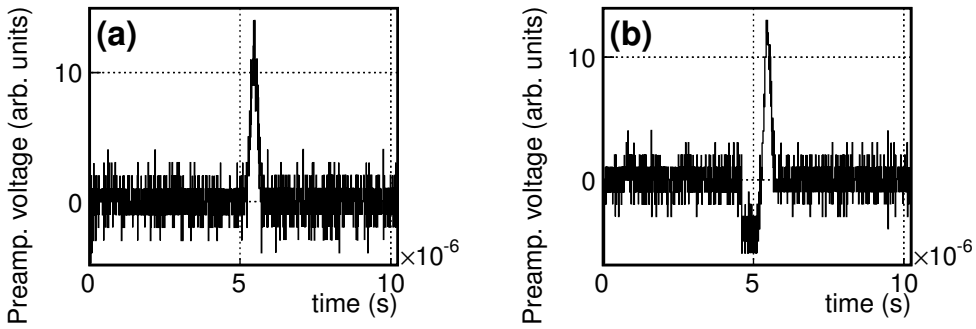

Figure 4.4: Differentiation of the anode (a) and grid (b) signals using the decay time of the preamplifier.

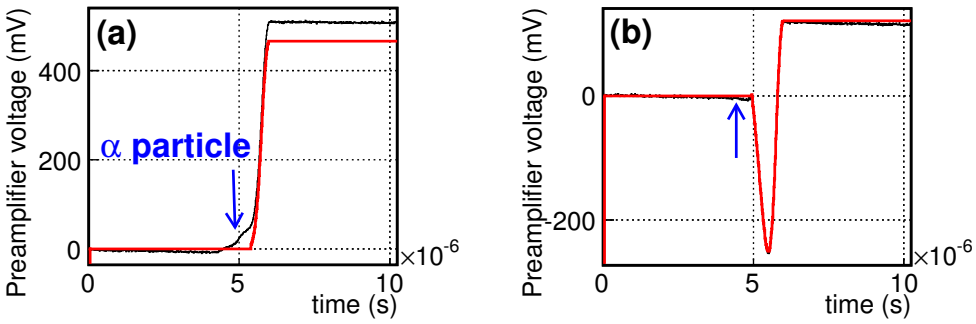

Figure 4.5: Anode (a) and grid (b) raw signals (black) and corrected signals (red) after baseline, ballistic deficit and α pile-up for an event of the ^{242}Pu sample using P10 as counting gas and having an α-particle signal (blue arrow) at the beginning of the FF slope for the anode signal but nearly invisible in the grid signal.

able to detect the different slope produced by the α-particle and discard its amplitude (Figure 4.5). The particular problem seen as well in Figure 4.5 where an α-signal is visible in the anode signal but not in the grid signal will be discussed in Chapter 5. In addition, the start and end channel of the slope is determined and is used to remove the α pile-up event occurring in the baselines pre- and post-trigger (see Figure 4.6).

CR-(RC)^4 filter and Pulse Height determination

In the last step of the signal processing a shaping filter is applied. A CR-(RC)^4 filter was chosen. The CR differentiation attenuates the low frequencies of the signal, while the (RC)^4 integrator smoothes the high frequencies [61]. The result after applying this filter is a Gaussian-like function. The amplitude of the pulse after the filter is equivalent to the charge collected, being the PH of the signal at its maximum amplitude (Figure 4.7).

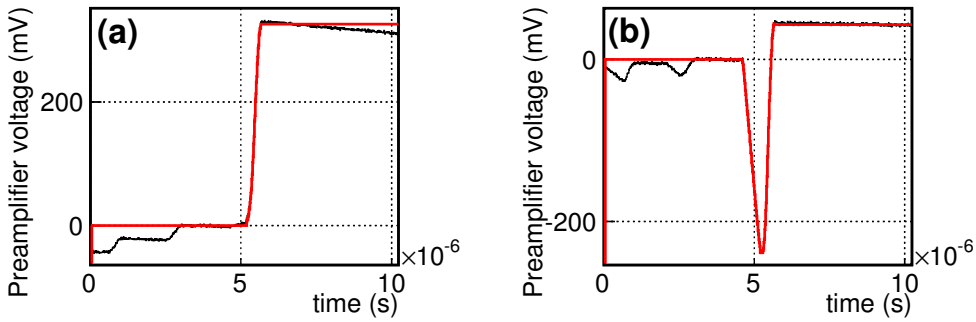

Figure 4.6: Anode (a) and grid (b) raw signals (black) and corrected signals (red) after baseline, ballistic deficit and α pile-up for an event with α pile-up happening well before the fission event.

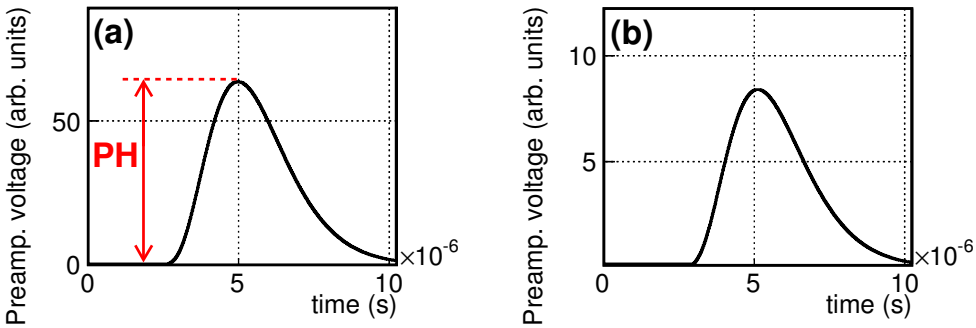

Figure 4.7: Amplitude signal of the anode (a) and grid (b) after CR-$(RC)^4$ filtering.

4.2 Corrections to the Pulse Height

After extracting the PH information from the stored signals they are saved in the form of `ROOT tree`'s. Then, data are read and treated entirely using `ROOT`.

4.2.1 Grid inefficiency correction

The first correction after the PH is generated is related to the grid inefficiency. In Chapter 3 it was explained that the shielding provided by the grid to the anode is not perfect. Therefore, a correction factor to the anode and grid PH needs to be applied. In the case of this experiment and taking into account the anode-grid distance, the grid wire radius and the distance between wires; the grid inefficiency factor (σ) was calculated using Equation (3.8) to 0.0304.

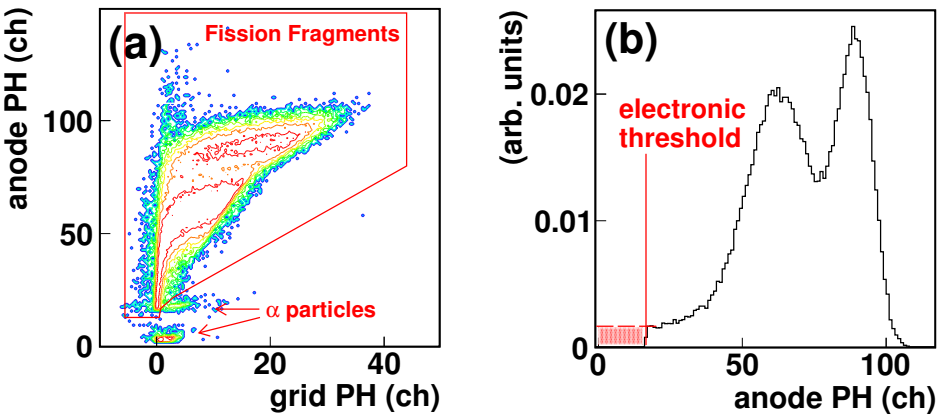

Figure 4.8: (a) Grid PH versus anode PH; data of ^{242}Pu with P10 as counting gas and at 2.0 MeV. Two regions can be identified: FFs and α-particle regions. (b) Projection of the anode PH.

4.2.2 Alpha pile-up rejection

Alpha-particles were already discarded from the baselines of the signals before obtaining the PH information. Nevertheless and even in the case of having an electronic threshold set on the constant fraction discriminator, several α-particles can pile-up together, specially in the case of ^{240}Pu, generating a PH of the same amplitude as a low energetic FF. These α-particles can be identified because their range inside the gas is different than the one of the FFs. In Figure 4.8(a) two separated regions of α-particles can be distinguished. In the first one, with anode PH values between 0 and 10, α-particles detected at the time of an event in the other side of the chamber are seen. In the second one, with anode PH values around 15 and 20, signals from several α particles piling up together have the same corresponding energy as low energetic FFs.

4.2.3 Extrapolation to zero pulse height

Due to the electronic threshold applied, FFs emitted at increasing angles that have lost an important amount of energy in their path through the sample, but still have reached the counting gas might not be able to trigger the system. To account for these events an extrapolation of the anode PH distribution is made (see Figure 4.8(b)). The value of the electronic threshold is mainly determined by the α-activity of the samples used, thus samples with higher activity will require higher thresholds. In the case of this experiment a linear fit to the low region of the anode PH was chosen to account for those FF emitted but not detected due to its low energy.

Chapter 5
Improvements on the experimental techniques and spontaneous fission half-life determination

5.1 The challenge of measuring high α-active targets

It is not the first time that measurements with high α-active targets are performed. In Chapter 2 the most relevant cross section measurements of ^{240,242}Pu have been listed and so it has been a long-standing problem how to measure highly active samples. The main issue when using analogue electronics with such samples and with ionization chambers as detectors is that the pile-up of several α-particle signals can produce the same amplitude as a low energy FF. Thus by introducing a grid between the cathode and the anode, as it has already been explained in Chapter 3, it is possible to determine the emission angle of the particle emitted, either an α or a FF. Finally, and considering that it is well known that an α-particle has a longer range than a FF in the gases considered, it is possible to identify them, even if they produce by piling up similar amplitudes as FF. An example of choosing the right region of interest to discard the α-particles was shown in Figure 4.8(a).

To test and make the proper adjustments both in the experimental setup as well as in the digital signal processing code and the subsequent pulse height analysis routines, the SF emission of both isotopes, ^{240,242}Pu, has been used. Not only has been an experiment performed to develop and test all the system, but to compare and analyze the influence of samples with different α-activity. All the investigations presented in this section were performed using the SF emission of both samples.

The results presented in this Chapter are an extended summary of Paper I.

In Figure 5.1 anode versus grid PH distributions for (a) ^{242}Pu and (b) ^{240}Pu are presented. It is perfectly visible how the ^{240}Pu distribution is distorted, specially at the edges and at the conjunction between α-particles and FFs. This effect was already noticeable when analyzing the obtained raw traces (Figure 5.2).

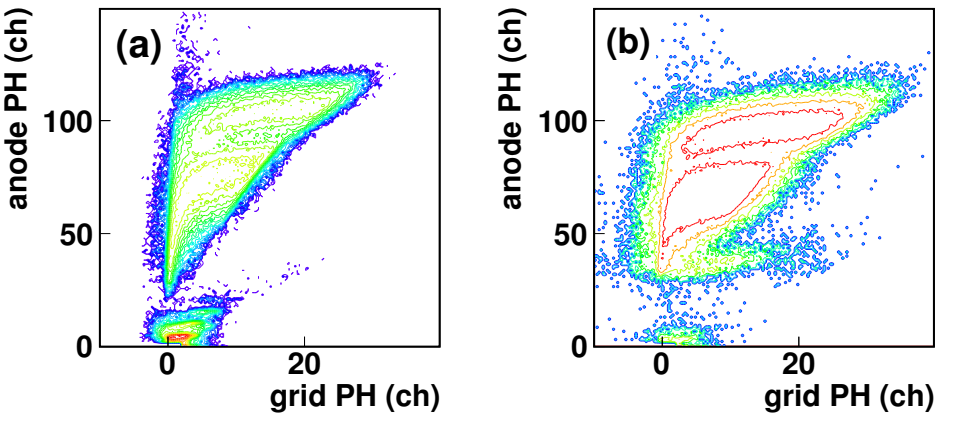

Figure 5.1: Grid PH versus anode PH for the two isotopes. (a) ^{242}Pu (0.1 MBq); (b) ^{240}Pu (0.8 MBq).

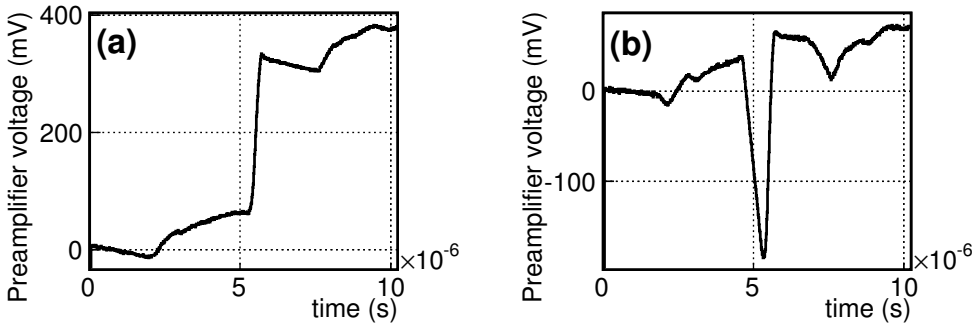

Figure 5.2: Charge collected by the anode (a) and grid (b) sampled with a 100 MHz WFD for an event of ^{240}Pu using P10 as counting gas.

The amount of α-particles that can pile up to distort the baseline and the FF event slope can be determined considering that the emission of α-particles follows a Poisson distribution such as:

$$P_m(z,\tau) = \frac{(z\cdot\tau)^m}{m!}\exp\left(-z\cdot\tau\right) \tag{5.1}$$

where z is the emission rate of the detected event, τ the signal length and m the pile-up order [61].

The rise time of a typical anode signal is around 0.20 μs when P10 is employed as counting gas. From the α-activity of the samples it is known that the ^{240}Pu emits 0.8 α/μs and, the ^{242}Pu, 0.1 α/μs. Considering that the α-particle emission follows a Poisson distribution, the amount of α-particles that can pile-up on the baseline of

the signal trace and on the FF slope from the preamplifier can be estimated. For the ^{240}Pu, it is expected to have in most of the cases between 2 and 5 α-particles piled-up on the baseline previous to the FF and the same amount on the baseline after the FF event. The case of ^{242}Pu is less severe and the prediction is to have 0 to 2 α-particles piled-up on the baseline before the FF and the same amount after. If the analysis is focused on the actual probability that a FF is detected together with 1 α-particle, it is foreseen around 14% of these events in the case of ^{240}Pu and just 2% in case of ^{242}Pu. In the case of the grid signal, where the full FF rise time is twice as long as the anode rise time, the probability of having an α-particle within the FF signal is 23% for ^{240}Pu and 4% for ^{242}Pu, respectively.

5.2 Efficiency determination for high α-active targets

An important correction when treating data from cross section measurements is the efficiency determination of the detection system. As mentioned, a TFGIC has a nearly 4π efficiency when using transparent samples and $2\times2\pi$ with a back-to-back configuration. Hence, the major impact on the efficiency is the FF loss inside the sample, meaning those FF emitted mainly at increasing angles that are stopped before being able to reach the counting gas.

An experimental method to determine FF losses inside the targets was already described in Ref. [52]. The method consists of determining the amount of FF stopped within the sample using their angular distribution. To apply this method an isotropic distribution of FF emission is sought. There are mainly two scenarios where fully isotropic emission of FFs is given: fission induced by thermal neutrons and spontaneous fission. Thus, the SF distribution will be used hereafter.

The FF angular information is extracted from the 2D grid versus anode PH distribution. For a value of the anode PH, there are a set of values that the grid can take. The range of these grid values is proportional to the emission angles, from 0° up to 90° (Figure 5.3). Thus, each anode PH value is projected onto the grid PH axis. The minimum of this projected distribution will correspond to $\cos\theta = 0$ and the maximum to $\cos\theta = 1$. The angular distribution is calculated as follows,

$$\cos\theta = \frac{P_G}{P_A\bar{X}/D} \tag{5.2}$$

where P_i corresponds to the PH of the anode (A) and the grid (G), $\bar{X}$ is the centre-of-gravity of the electron cloud ionized by the FF and D is the cathode-grid distance.

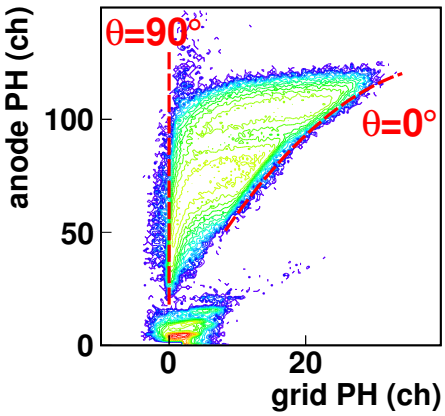

Figure 5.3: Grid PH versus anode PH for ^{242}Pu. The emission angle range for each anode PH value is plotted.

The cosine distribution obtained is shown in Figure 5.4(a). The degradation due to FFs stopped inside the sample and those below the electronic threshold is visible at low cosine values. To determine the total number of emitted FFs (N_{cos}), one would do:

$$N_{cos} = A + \Delta A \tag{5.3}$$

with A being the integral of the cosine distribution and ΔA the missing part related with the thickness of the sample. To extract the sample loss it is needed to consider the anode PH distribution (N_{PH}) and extrapolate down to 0 (ΔN_{PH}) to account for FFs emitted but not detected due to the high electronic threshold requested not to trigger on α events (Figure 5.4(b)). The experimental efficiency due to sample loss (ϵ_{expt}) will be calculated as:

$$\epsilon_{\text{expt}} = \frac{N_{PH} + \Delta N_{PH}}{N_{cos}} = \frac{N_{2\pi}}{N_{cos}} \tag{5.4}$$

Without any previous consideration it is expected that using the thinner sample (^{240}Pu) will have a higher efficiency than using the thicker one (^{242}Pu). The results showed, instead, that ϵ_{expt} was nearly the same for both samples: 94(1)% for ^{240}Pu and $94 - 95(1)$% for ^{242}Pu.

5.2.1 Angular dependence

In Chapter 4 it was explained that the major contribution to the baseline oscillation of the preamplifier signal is due to an incomplete discharge of the latter before a new set of charged particles approaches the electrode. This effect is more evident in Figure 5.2

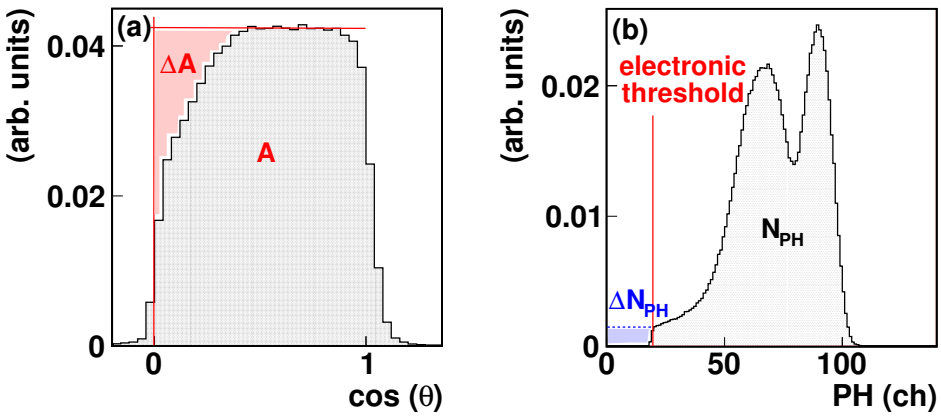

Figure 5.4: (a) Angular distribution for ^{242}Pu. The FF loss inside the sample is visible at low $\cos\theta$ values. By determining the integral of the distribution and ΔA (the missing part of the distribution) one can obtain the sample loss. (b) PH distribution for ^{242}Pu and determination of the counts under the electronic threshold.

where an anode and a grid signal of ^{240}Pu are plotted. In that single event it is possible to distinguish up to two α-particles prior to the FF event and up to two after, still if focus is taken in just the anode trace probably the conclusion would be that only one α-particle has piled-up before the FF and only one after.

A way to prove that not only the preamplifier was not discharging completely but that this is the reason of the deterioration of the 2D anode versus grid PH distribution in case of ^{240}Pu is to tag and obtain a quantified value of the α-particles piling up before and after the FF event. This was done at the time of the data analysis by running an iterative code that was searching for a strong change of the slope in the baseline before and after the FF event. Figures 5.5 and 5.6 prove the correlation of the amount of α-particles piled up on the baseline before and after the FF event, respectively, with the determination of the cosine distribution. Even more, this correlation is inexistent when the pile-up occurs after the FF event (see Figure 5.6).

The zero-α method

To avoid the degrading effect of the α-particles the distribution obtained when selecting events with no α-particle piled up can be used. Normally, this distribution is expected to be close to the true cosine distribution from a sample with no α-activity. By doing so a more consistent result of the efficiency is obtained: 97(1)% for ^{240}Pu and 95$-$96(1)% for ^{242}Pu.

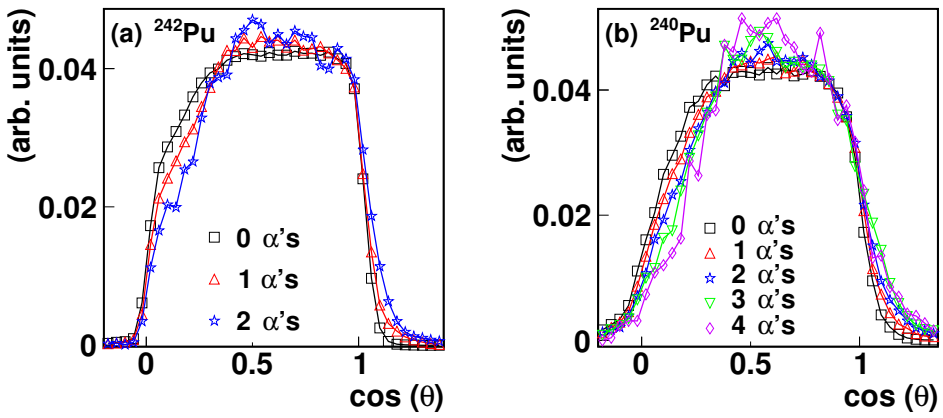

Figure 5.5: Correlation between α pile-up before the FF event and the degradation of the cosine distribution for ^{242}Pu (a) and ^{240}Pu (b) using P10 as counting gas. A stronger effect is seen for the more active target (^{240}Pu).

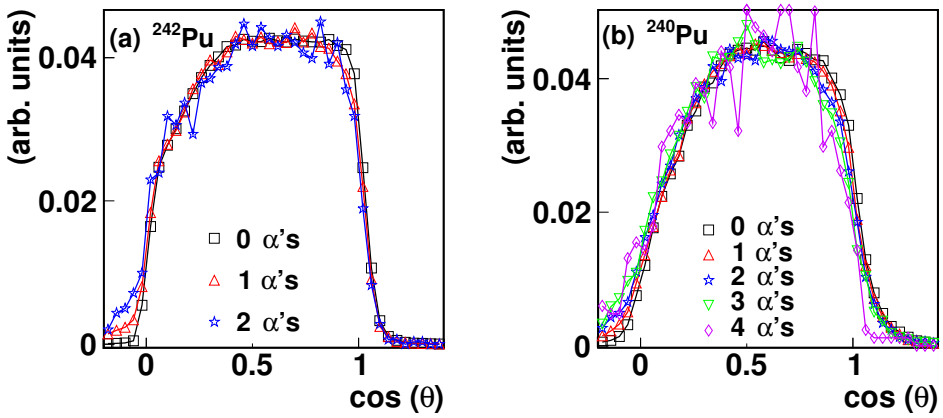

Figure 5.6: Correlation between α pile-up after the FF event and the degradation of the cosine distribution for ^{242}Pu (a) and ^{240}Pu (b) using P10 as counting gas. No strong effect is seen in the distributions of either sample.

5.2.2 Improving the signal rise time: P10 vs CH_4

Seeking to achieve a better experimental performance several improvements on the setup were considered. First, the behavior of the preamplifiers was questioned, but the rise time of the ones used is faster than 12 ns and, therefore, one order of magnitude shorter than the FF signal rise time (around 200 ns). Second, a gas with an improved drift velocity could be employed. Two gases were contemplated: CF_4 and CH_4. Both

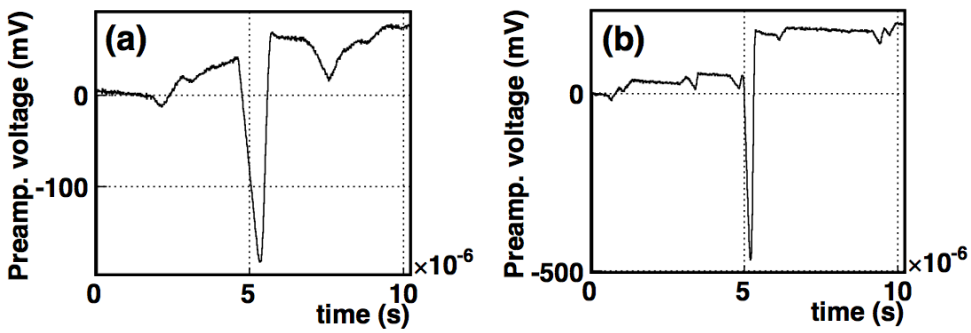

Figure 5.7: Grid signals obtained with ^{240}Pu using either P10 (a) or CH_4 (b). A big improvement is seen in the signal taken with CH_4, being able to discriminate between close by α-particles.

gases were already tested and compared with P10 elsewhere [62]. CF_4 requires to work in an under pressure vacuum tight ionization chamber. Since the TFGIC used in this experiment was not vacuum tight and it needed to work at over pressure, CH_4 was chosen. Its main properties were already listed in Chapter 3 and, as mentioned, the gas flow and the HV were increased to work in the plateau region of the drift velocity function.

Figure 5.7 compares a grid signal obtained with ^{240}Pu using (a) P10 or (b) CH_4. Since the drift velocity of the charges in CH_4 is much faster than P10, the electrodes are able to collect those charges in less time, thus the preamplifier can be completely discharged before the next set of charges reaches the electrode.

The rise time of the anode signals is around 0.077 μs for CH_4 (0.20 μs for P10). The probability of an α-signal to appear within the time frame of the FF on the anode is of $\sim$ 6% (14%) for ^{240}Pu and $\sim$ 0.8% (2%) for ^{242}Pu using CH_4 (P10) as counting gas. In the case of the grid (where the FF signal is twice as long) the probability is $\sim$ 11% (23%) for ^{240}Pu and $\sim$ 1.5% (4%) for ^{242}Pu using CH_4 (P10).

Figure 5.8 depicts the 2D distribution of the grid PH versus the anode PH obtained with ^{240}Pu using CH_4 as counting gas. Comparing the present figure with Figure 5.1, obtained with P10, it is clear that the edges of the distribution are better defined now and more important the region of α-particles is well distinguished with respect to the FF one. By performing a projection of the distribution onto the anode PH axis, and after normalizing the channels to PH energy, a distinction of 7 α pile-up lines is visible when using CH_4 as counting gas (full line). Those lines correspond to n α-particles piling up at the same time, being $n = 1, 2, 3, 4, 5, 6, 7$. Effectively each of the single peaks sits around the sum of the energy of the amount of α-particles that piled up (1 α-particle ($\sim$5 MeV), 2 α-particles ($\sim$10 MeV), etc.). In the same plot, a projection of the P10 distribution (dashed-dotted line) is presented where just one α pile-up line

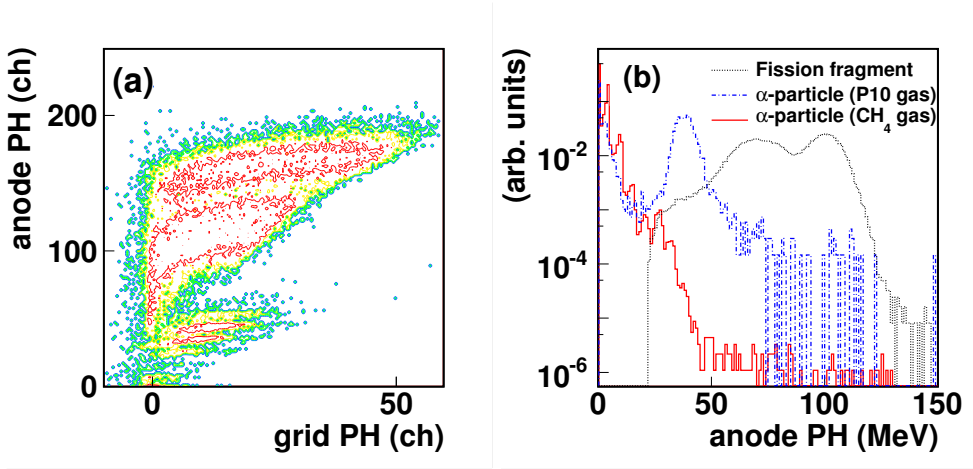

Figure 5.8: Distributions for ^{240}Pu. (a) 2D grid PH versus anode PH distribution using CH_4 as counting gas. Three α pile-up lines are visible for anode PH values between channel 20 and 50. (b) Projection of the anode PH when just FFs are selected (dotted line) using either P10 or CH_4, just α-particles are selected and P10 is used as counting gas (dashed-dotted line) and just α-particles are selected and CH_4 is used as counting gas (full line).

is visible at around 38 MeV. The dotted line shows the FF PH distribution cleaned of α-particles by applying a region of interest on the FFs. This distribution remains nearly unchanged when using P10 or CH_4.

By correlating again the amount of α-particles before the FF signal and the cosine distribution (Figure 5.9), even though the statistics at higher α pile-up for ^{240}Pu are low, an improvement is observed with respect to Figure 5.5. The analysis gives a ϵ_{exp} ranging from 98 to 100% with an uncertainty of 1% for both samples. The accuracy that this method can provide is not better than 1% in any case. This is based on the fact that analyzing different runs for both gas mixtures and samples give slightly different cosine distributions. This is exemplified in Figure 5.10.

The ideal method

A different experimental method (*ideal*) can be applied for determining the sample efficiency by means of the cosine distribution. The method consists of supposing an ideal continuous uniform cosine distribution in the range $\cos\theta = [0, 1]$, where the normalized counts in each bin are equally distributed along the range. To exemplify the method the distribution plotted in Figure 5.11 will be considered. There, two distributions of ^{240}Pu are shown, the first one obtained with P10 and the second one with CH_4 as a counting gas. In an ideal case the maximum value of the distribution will correspond to the normalized total amount of counts divided by the number of bins

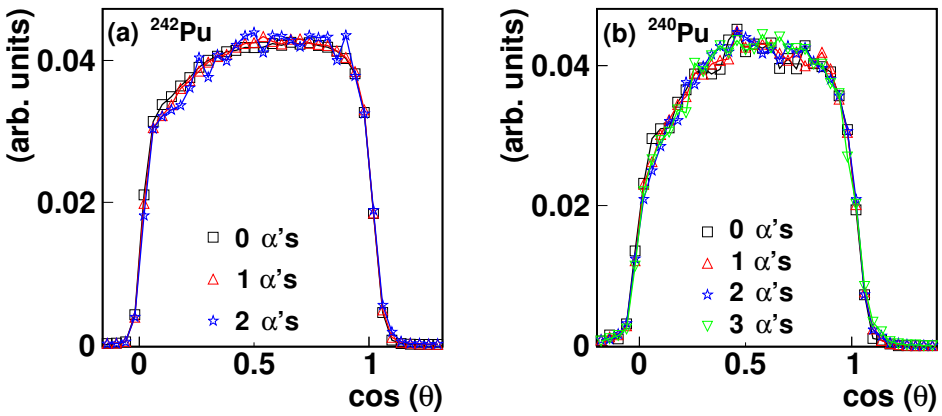

Figure 5.9: Correlation between α pile-up before the FF event and the degradation of the cosine distribution for ^{242}Pu (a) and ^{240}Pu (b) using CH_4 as counting gas.

in the range, in that case 0.04. Nevertheless, the maximum value of the distribution taken using P10 as a counting gas is well above 0.04 but, by using CH_4 as a counting gas, the maximum value of the distribution is slightly lower than for P10, yet higher than the ideal 0.04. As a consequence this difference of counts can be considered as equivalent to the lack of counts in the low cosine part (between $\cos\theta = 0$ and $\cos\theta = 0.4$). Taking into account these observations, it is possible to determine the sample efficiency considering that the maximum normalized amount of counts in each bin of the distribution would be the number of bins multiplied by their width. This is, in the present case, 0.04. In the bins that exceed this value, the difference between the value and the maximum considered value would be taken and these extra counts would be added to the bins with low cosine values. Thus, if this method is applied the value of the sample efficiency would range from 98 to 99% (1%) for the ^{242}Pu and 99.6% (1.0%) for the ^{240}Pu with P10 and around 100(1)% for both samples using CH_4.

The *zero-α method* can be applied together with the *ideal method* obtaining as a result for the sample efficiency 99(1)% for the ^{242}Pu and 100(1)% for the ^{240}Pu (using the P10 data). The *zero-α method* will not improve the result on the CH_4 cosine distributions because for these distributions there is no visible degradation due to α pile-up.

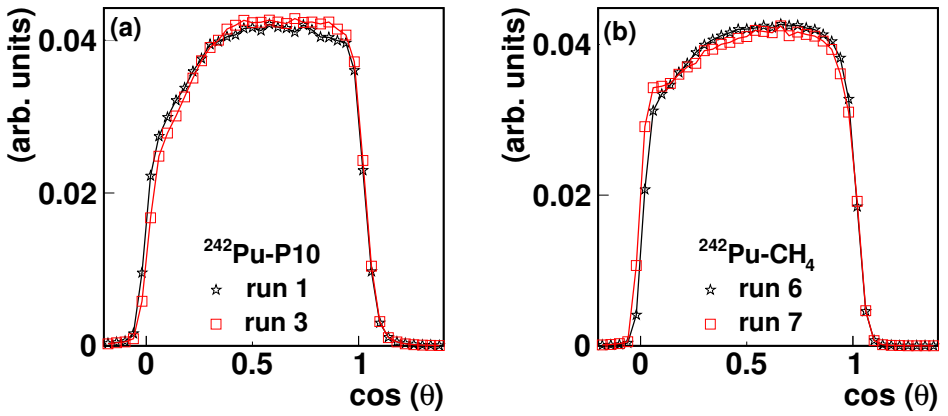

Figure 5.10: Comparison of the cosine distributions for different runs for ^{242}Pu using P10 (a) and CH_4 (b). It was observed that for two different runs with the same isotope and counting gas slightly different cosine distributions are obtained, therefore with this method it is not possible to achieve an accuracy better than 1%.

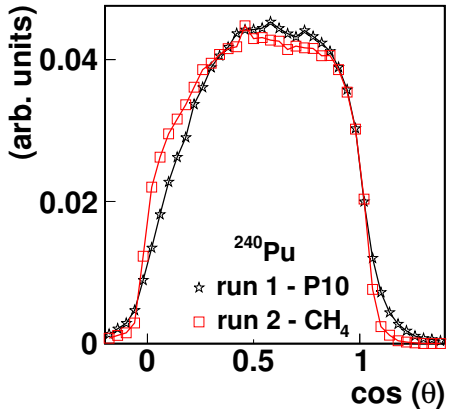

Figure 5.11: Comparison of the cosine distributions of ^{240}Pu obtained using P10 and CH_4 (see text for further explanation).

5.2.3 Theoretical calculation of FF losses in the sample

A theoretical calculation of the FF loss inside the sample can be done taking into account the range of the FFs in the sample. This range can be extracted from the stopping power of a certain particle or molecule inside a certain compound. The stopping power ranges were obtained from SRIM [63]. As presented in Ref. [52], the loss inside the sample can be calculated as:

$$\Delta_{\text{sample}} = \frac{t}{2R_{\text{sample}}} = \frac{t}{2}\sum_i \frac{W_i}{R_i} \tag{5.5}$$

with t as the thickness of the sample, R_i the range of isotope i and W_i the weight fraction of isotope i in the sample. By using the properties for two typical FF (in terms of mass and energy) the values obtained were: 99.7% for ^{240}Pu and 98.1% for ^{242}Pu.

5.2.4 GEANT4 simulations

Finally, GEANT4 simulations [64] were done to mimic the physics that FFs undergo when traveling through the sample. An initial FF kinetic energy distribution for the SF process obtained with the GEF code [65] for each isotope, ^{240}Pu and ^{242}Pu, was employed as an input of the code. The amount of FF transmitted into the counting gas geometry was 99.2% for ^{240}Pu and 97.4% for ^{242}Pu.

5.2.5 Results

Table 5.1 summarizes the results obtained using different methods and cosine distributions. By changing the counting gas inside the TFGIC, it was possible to overcome almost completely the effect of the loss of information due to an incomplete discharge of the preamplifiers caused by α pile-up. Besides, it is possible to improve the initial results by being able to tag the α-particles piled-up and use a cosine distribution of the events that had no coincidence with α-particles. The achieved experimental accuracy was not better than 1% and since the efficiency value was fluctuating for P10, the theoretical efficiency value was chosen considering the experimental uncertainty described above.

Table 5.1: Summary on the efficiency (ϵ) results by using different methods, counting gas and cosine distributions.

Description			^{240}Pu	^{242}Pu
Cosine distribution	Method	Counting gas		
All events	Ref. [52]	P10	94(1)%	94-95(1)%
All events	Ideal	P10	99.6(1)%	98-99(1)%
0-α	Ref. [52]	P10	97(1)%	95-96(1)%
0-α	Ideal	P10	100(1)%	99(1)%
All events	Ref. [52]	CH_4	98-100(1)%	98-100(1)%
All events	Ideal	CH_4	∼100(1)%	∼100(1)%
	Theory		99.7%	98.1%
	GEANT4		99.2%	97.4%

5.3 Spontaneous fission half-life determination

The SF half-life has been calculated using:

$$T_{1/2,SF} = \frac{\%^{j}\mathrm{Pu}}{\mathrm{A}_j} \frac{1}{\left(\frac{C_{SF}}{t \cdot \epsilon_j \cdot \ln 2 \cdot m_{\mathrm{Pu}} \cdot N_A} - \sum_{i}^{n} \frac{\%^{i}\mathrm{Pu}}{\mathrm{A}_i \cdot T_{1/2,SF}(i)} \right)} \tag{5.6}$$

where $\%^{j}$Pu is the purity of the sample, A_j its atomic mass, C_{SF} are the counts detected, t is the effective measuring time, ϵ_j is the detection efficiency, m_{Pu} is the sample mass, N_A the Avogadro's number and $\sum_{i}^{n} \frac{\%^{i}\mathrm{Pu}}{\mathrm{A}_i \cdot T_{1/2,SF}(i)}$ the contribution from the other isotopes contained in the sample.

5.3.1 Results and comparison with available data

Several measurements have been performed with each sample. Figure 5.12 summarizes in a graph the resulting $T_{1/2,SF}$ values. Run 1 for ^{240}Pu and 1-5 for ^{242}Pu were performed with P10 as counting gas, while runs 2-3 for ^{240}Pu and 6-7 for ^{242}Pu with CH_4. Each run encloses several individual data sets obtained under the same experimental conditions. The data sets contain between 10000 and 250000 fission events using P10 and between 50000 and 1500000 events using CH_4. All labelled runs are performed using a different electronic threshold. The error bars in the plot describe the statistical and the systematic uncertainties, the thick horizontal line is an eye guide for the weighted average of all the runs and the dotted lines are the final uncertainties (systematic and statistical) expressed with 1σ. It is worth mentioning that the weighted average was calculated using just the statistical uncertainties and, once the final value was obtained the systematic uncertainties were included. The bullet symbols represent previous experimental results, and the two highlighted literature values are the

Table 5.2: Summary of the uncertainties corresponding to the SF half-life ($T_{1/2,SF}$) for ^{240,242}Pu.

Uncertainty source	^{240}Pu	^{242}Pu
Statistical	0.13%	<0.1%
Mass	0.4%	0.9%
Sample efficiency	1%	1%
Sample purity	<0.001%	<0.001%
Dead time acquisition program	<0.07%	<0.012%
Total (systematic and statistical)	1.1%	1.3%

Table 5.3: Summary of the SF half-life ($T_{1/2,SF}$) for ^{240,242}Pu. The experimental uncertainties presented include both the statistical and systematic uncertainties. The weighted average of literature values presented by Ref. [66] and by Ref. [68] are given, too.

$T_{1/2,SF}$ (yr)	^{240}Pu	^{242}Pu
Holden (2000) [66]	$1.14 \times 10^{11}(0.9\%)$	$6.77 \times 10^{10}(1.0\%)$
Chechev (2009) [67, 68]	$1.15 \times 10^{11}(1.7\%)$	$6.79 \times 10^{10}(1.4\%)$
This experiment	$1.165 \times 10^{11}(1.1\%)$	$6.74 \times 10^{10}(1.3\%)$

weighted average of the subset of literature data presented by Refs. [66] and [67]. In Table 5.2 the present uncertainty budget is listed and Table 5.3 compares the weighted averages from previous data and the value obtained in the present experiment.

The uncertainty budget of previous literature data has been listed in two tables. Table 5.4 describes the data of ^{240}Pu and Table 5.5 data corresponding to ^{242}Pu. It is clear that the present experiment was performed with unprecedented statistics. In addition, lower systematic uncertainties than those of previous experiments were reached. In the case of ^{242}Pu, only one experiment claims to have lower systematic uncertainties (Meadows, 1977 [78]). In this experiment, the sample preparation as well as the FF detector were similar to the present work. Nevertheless, the considered uncertainty on the fission fragment loss inside the sample was only 0.1%; giving an overall statistical uncertainty of just 0.5%. Hence, their total uncertainty was only 0.7%. Despite of that, the value obtained here is the same as the value of Ref. [78] recalculated by Ref. [66], taking into account the new value of the half-life of ^{239}Pu.

The results are in agreement with the literature values for ^{242}Pu. Nevertheless, and using exactly the same method, the ^{240}Pu SF half-life value obtained is slightly higher than some of the literature values. This could be explained by the high α-activity of the sample. By having a more precise discrimination of α-particle signals the count rate in this work might have been lower than in previous experiments done with analogue electronics, thus obtaining a higher SF half-life value.

Table 5.4: Summary of the uncertainties corresponding to the SF half-life ($T_{1/2,SF}$) of the literature values presented in Fig. 5.12 for ^{240}Pu. The statistical and systematic uncertainties are given where known together with the total uncertainty. (The hyphen indicates a situation where the uncertainty budget of the experiment is not well described; thus, the total uncertainty is taken.)

Experiment	σ_{STAT}	σ_{SYST}	σ_{TOTAL}
Fieldhouse (1967) [69]	-	2%	2%
Budtz-Jørgensen (1980) [25]	1.5%	2.1%	2.6%
Androsenko (1984) [70]	-	-	2.6%
Selickij (1988) [71]	-	2.5-3.3%	2.6%
Dytlewski (1989) [72]	0.8%	∼1.4%	1.6%
Ivanov (1991) [73]	-	-	1.7%
This experiment	0.13%	1.1%	1.1%

Table 5.5: Summary of the uncertainties corresponding to the SF half-life ($T_{1/2,SF}$) of the literature values presented in Fig. 5.12 for ^{242}Pu. The statistical and systematic uncertainties are given where known together with the total uncertainty. (The hyphen indicates a situation where the uncertainty budget of the experiment is not well described; thus, the total uncertainty is taken.)

Experiment	σ_{STAT}	σ_{SYST}	σ_{TOTAL}
Studier (1956) (cited by Ref. [74])	-	-	10%
Butler (1956) [75]	0.8%	1.3%	2.6%
Mech (1956) [74]	∼0.6%	2.6%	2.7%
Druin (1961) [76]	5%	∼8.7%	10%
Malkin (1963) [77]	-	-	2.3%
Meadows (1977) [78]	0.4-0.5%	∼0.5%	0.7%
Selickij (1988) [71]	∼2.7%	2.7%	3.8%
This experiment	<0.1%	1.3%	1.3%

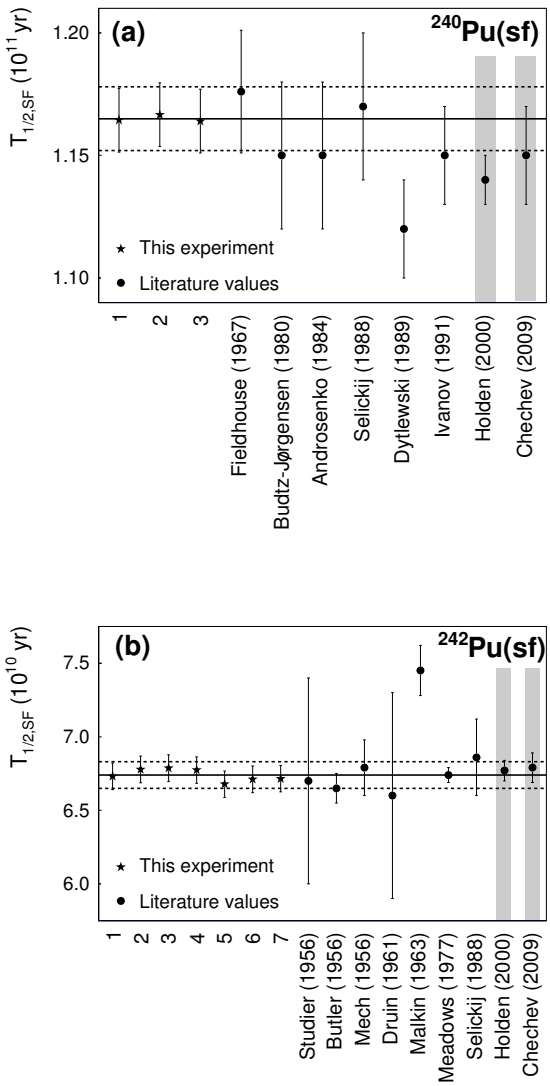

Figure 5.12: SF half-life results for ^{240}Pu (a) and ^{242}Pu (b) (stars) compared with some literature values (bullets), their weighted average calculated by Ref. [66], and the weighted average calculated by Ref. [68]. The thick line is the weighted average of all the present experimental runs and the dotted lines are the total uncertainty on the weighted average. The mean was weighted with the statistical uncertainty and then adding the systematic component (1.1% for ^{240}Pu and 1.3% for ^{242}Pu). The literature values shown are the ones used by Refs. [66] and [68] to calculate the weighted average. In the ^{240}Pu case the literature values correspond to: Fieldhouse (1967) [69], Budtz-Jørgensen (1980) [25], Androsenko (1984) [70], Selickij (1988) [71], Dytlewski (1989) [72], Ivanov (1991) [73] and Holden (2000) [66], and Chechev (2009) [68]. The literature values for the ^{242}Pu are: Studier (1956) (cited by Ref. [74]), Butler (1956) [75], Mech (1956) [74], Druin (1961) [76], Malkin (1963) [77], Meadows (1977) [78], Selickij (1988) [71], Holden (2000) [66], and Chechev (2009) [68].

Chapter 6

Neutron-induced fission cross section measurements

The main purpose of this project was to measure the neutron-induced fission cross section of ^{240,242}Pu. The experimental setup was build to lower the amount of corrections to be performed during the offline analysis. Yet, few corrections need to be considered for a correct understanding of the experiment. In this Chapter an extended explanation of them will be given. In this way, proof of the accuracy of the present analysis is given.

6.1 Cross section formulation

The number of fission events that would be obtained for any sample with N number of atoms under a neutron flux Φ is described as

$$C = \sum_i N_i \cdot \Phi \cdot \sigma_i \tag{6.1}$$

where the sub-index i accounts for the mixture of isotopes within the sample and σ_i is the neutron-induced cross section of each of them.

In addition, if the neutron flux impinging on the sample is not mono-energetic and is a mixture of two single neutron energies, the fission events are calculated as

$$C = \sum_i N_i \cdot \Phi_0 \cdot \sigma_{i,0} + \sum_i N_i \cdot \Phi_1 \cdot \sigma_{i,1} \tag{6.2}$$

where the sub-index 0 corresponds to the neutron energy from a reaction to the nuclear ground state and the sub-index 1 corresponds to the neutron energy resulting from a reaction to the first excited state of the recoil nucleus.

Since the neutron flux is not measured in this experiment a reference sample is used to normalize the counts. The reference sample is supposed to have a relatively well-known cross section, thus the contribution on the uncertainty budget will remain

low. The ratio of fission events between the two samples is

$$\frac{C_S}{C_R} = \frac{\sum_i N_i^S \Phi_0^S \sigma_{i,0}^S + \sum_i N_i^S \Phi_1^S \sigma_{i,1}^S}{\sum_i N_i^R \Phi_0^R \sigma_{i,0}^R + \sum_i N_i^R \Phi_1^R \sigma_{i,1}^R} \tag{6.3}$$

where S refers to the sample under study and R to the reference target. As it will be seen later on, even if the flux is not measured and its absolute value is not of interest, its shape is of importance to correct for the different solid angles between the neutron producing target and the samples of different sizes. If now the cross section of the main isotope of the sample under study is isolated, the following equation is obtained,

$$\sigma_{main,0}^S = \frac{C_S}{C_R}\frac{F_S}{F_R} \cdot \left(\sum_i \frac{N_i^R}{N_{main}^S} \frac{\Phi_0^R}{\Phi_0^S} \sigma_{i,0}^R + \sum_i \frac{N_i^R}{N_{main}^S} \frac{\Phi_1^R}{\Phi_0^S} \sigma_{i,1}^R \right) - \\ - \sum_i \frac{N_i^S}{N_{main}^S} \frac{\Phi_1^S}{\Phi_0^S} \sigma_{i,1}^S - \sum_j \frac{N_j^S}{N_{main}^S} \sigma_{j,0}^S \tag{6.4}$$

where the sub-index i corresponds to each of the isotopes contained in either the sample or the reference target, the sub-index j indicates the secondary isotopes also contained in the sample; and the number of events detected are

$$C = \frac{C_{total}}{\epsilon} - \sum_i C_{SF,i} \tag{6.5}$$

where C_{total} are the total counts detected in the corresponding side of the TFGIC, ϵ is the efficiency of the FF counting; and $C_{SF,i}$ are the counts due to the SF for isotope i. The factor F that has been added corresponds to the MCNP flux correction due to the thermalization of neutrons. Finally, the ratios of the fluxes due to the reaction to the ground state and the reaction to the excited state of the recoil nucleus in Equation (6.4) are described as,

$$\frac{\Phi_0^R}{\Phi_0^S}\sigma_{k,0}^R = \frac{\sum_i \%m_i^R \Phi_0^R(\theta_i)}{\sum_i \%m_i^S \Phi_0^S(\theta_i)} \frac{\sum_i \Phi_0^R(E_i)\sigma_{k,0}^R(E_i)}{\sum_i \Phi_0^R(E_i)} \tag{6.6}$$

$$\frac{\Phi_1^R}{\Phi_0^S}\sigma_{k,1}^R = \frac{\sum_i \Phi_1^R(E_i)}{\sum_i \Phi_0^R(E_i)} \frac{\sum_i \%m_i^R \Phi_1^R(\theta_i)}{\sum_i \%m_i^R \Phi_0^R(\theta_i)} \frac{\sum_i \%m_i^R \Phi_0^R(\theta_i)}{\sum_i \%m_i^S \Phi_0^S(\theta_i)} \frac{\sum_i \Phi_1^R(E_i)\sigma_{k,1}^R(E_i)}{\sum_i \Phi_1^R(E_i)} \tag{6.7}$$

$$\frac{\Phi_1^S}{\Phi_0^S}\sigma_{k,1}^S = \frac{\sum_i \Phi_1^S(E_i)}{\sum_i \Phi_0^S(E_i)} \frac{\sum_i \%m_i^S \Phi_1^S(\theta_i)}{\sum_i \%m_i^S \Phi_0^S(\theta_i)} \frac{\sum_i \Phi_1^S(E_i)\sigma_{k,1}^S(E_i)}{\sum_i \Phi_1^S(E_i)} \tag{6.8}$$

where the first term accounts for different diameter of the samples and homogeneities, as the flux is a function of the neutron energy as well as of the emission angle of the neutron produced from a reaction to the ground state, indexed 0. The second term accounts for the same parameters but when considering an interaction of the

neutron resulting from a reaction to the first exited state of the recoil nucleus with the reference sample as a function of the interaction of a neutron produced from a reaction to the ground state of the recoil nucleus at the sample under study. And the third term accounts for these geometric factors for the neutron emitted from a reaction to the excited state of the recoil nucleus at the sample under study as a function of a neutron emitted from a reaction to the ground state of the recoil nucleus in the same sample. In Equations (6.6) to (6.8) the sub-index k refers to the different isotopes in the sample and the sub-index i to the neutron energy.

6.2 Corrections to the data

It is possible to classify all the corrections needed to apply to the data obtained into two groups: the corrections that were caused due to loss of fission events produced by the high α-activity of the samples and the thickness of the sample; and the corrections due to the non-perfect monoenergetic neutron beam and its degradation due to the material of the experimental setup.

6.2.1 Lost counts due to electronic threshold

The effect of the electronic threshold applied to the experimental setup to avoid triggering on the α-particle signals needs to be corrected for since FFs that have travelled long enough inside the sample might enter the gas with a similar energy than piled-up α-particles. The influence of the electronic threshold will be higher on the thicker samples (i.e. ^{237}Np) and on the samples with high α-activity (i.e. ^{240}Pu). Table 6.1 describes the contribution of the total correction of fission events for each sample at each ratio measured.

A comparison between the different pulse height distributions obtained for the different samples is plotted in Figure 6.1. Figure 6.1(a) compares the three reference isotopes used: ^{238}U, ^{235}U (sample #1) and ^{237}Np. The ^{238}U and ^{235}U samples have very similar thicknesses, thus their PH spectra is similar; additionally their α-activity is not as strong as in the ^{240,242}Pu samples, therefore the FF slope in their signals has less

Table 6.1: Correction due to the electronic threshold for each isotope at each ratio measured. The values presented are always the upper limits.

Sample 2 $\longrightarrow$ Sample 1 $\downarrow$	^{235}U	^{238}U	^{237}Np
^{238}U	1.4%/1.5%	-	-
^{237}Np	11%/2.2%	4%/1.4%	-
^{240}Pu	5%/2.3%	3%/9.7%	4%/13.6%
^{242}Pu	4%/2.4%	3%/5%	3%/8.5%

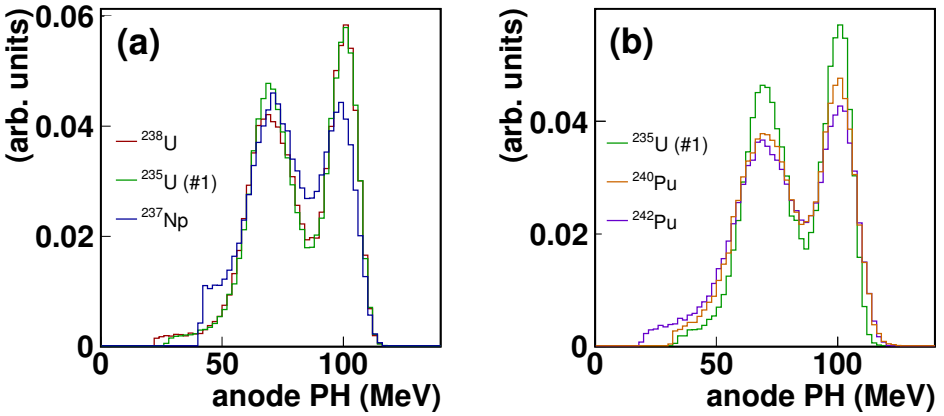

Figure 6.1: Comparison of PH spectra taken with different isotopes with an incident neutron energy of 1.8 MeV. (a) ^{238}U, ^{235}U (sample #1) and ^{237}Np samples; the degradation of the PH for the thicker ^{237}Np sample is visible. (b) ^{238}U, ^{240}Pu and ^{242}Pu samples; the ^{238}U and ^{240}Pu spectra were taken together using P10 as counting gas. The rest of the spectra were taken using CH_4. The PH obtained with the ^{240,242}Pu samples, having a stronger α-activity, is worse compared to samples with similar thicknesses and less α-activity. In addition, the effect of measuring using a high electronic threshold is seen in the ^{238}U spectra.

probability to be influenced by an α pile-up. The influence of the electronic threshold on the thicker ^{237}Np deposit is large, as it is obvious from the picture. Besides, it is clear that the peak-to-valley ratio is distorted due to the thickness. Otherwise, in Figure 6.1(b) the ^{240,242}Pu samples with stronger α-activity are compared. Even if the ^{240}Pu sample is nearly one order of magnitude thinner than the ^{242}Pu deposit, the PH spectra of both samples resembles. This could be, to some degree, because of the distortion of the FF traces due to α piled-up signals. In addition, in the same plot, a ^{235}U PH spectrum taken together with ^{242}Pu is plotted. Here it is clear how the misinterpretation of the low energy part having high electronic thresholds can be a problem in such experiments. To overcome the issue, a reference ^{235}U PH spectra taken relative to a sample with less α-activity, i.e. ^{238}U, is normalized together with the high threshold spectra. In this way, the amount of counts lost in the high threshold spectra is known.

6.2.2 Target thickness and anisotropy of FF angular distribution

The efficiency (ϵ) will depend on the thickness of the target only in the case of having a neutron energy close to 0. In all the other cases, the efficiency needs to be corrected for the momentum transfer due to the incoming neutron energy and the anisotropy of

the emitted FFs. The efficiency is described depending on the position of the foil with respect to the neutron producing target (facing the neutron source or facing away) [79],

$$\begin{aligned} \epsilon &= \frac{t_0}{2R}\left(1+2\eta\frac{R}{t_0}\right)\left(1-\frac{a_2}{2}\right) && \text{foil facing the neutron source} \\ \epsilon &= \frac{t_0}{2R}\left(1-\eta\left(\frac{2R}{t_0}-\eta\frac{R^2}{t_0^2}\right)\right)\left(1-\frac{a_2}{2}\right) && \text{foil facing away from the neutron source} \end{aligned} \tag{6.9}$$

where t_0 is the absolute[1] thickness of the target, R is the range that a FF can travel within the target, a_2 is the parameter of the Legendre polynomial corresponding to the anisotropy of the FF cosine distribution and η is the ratio of the velocity of the fissioning nucleus to the average velocity of its fragments,

$$\eta = \frac{\sqrt{\frac{E_n}{E_f}A_f}}{A_n+1} \tag{6.10}$$

where E_n is the neutron's kinetic energy, E_f is the average kinetic energy of the FF, A_f is the average FF atomic weight and A_n is the atomic weight of the target nucleus.

As presented in Chapter 5, this correction at low neutron incoming energies where the neutron momentum transfer to the FFs can be considered negligible will be simplified to Equation (5.5) if the angular distribution of the FFs is isotropic. The FF range within the sample compound was considered to be of 4.76 mg/cm^2 for the tetrafluoride samples and 3.21 mg/cm^2 for the hydroxide samples. Table 6.2 presents the range of values that the efficiency can take depending on the sample, the position of the sample with respect to the neutron beam and the neutron incoming energy. The uncertainty related with this parameter is of 1%.

6.2.3 Influence of the neutron spectrum and the sample spot size and inhomogeneity

In Chapter 3 it was shown that depending on the thickness of the neutron producing target, the energy width of the neutrons will vary. Since the proton induced cross section does not take a constant value this effect needs to be accounted for in the final cross section calculation by normalizing the reference cross section with the neutron flux shape. In addition, the emission of neutrons at the producing target is not fully isotropic. The fissioning samples used in the experiment have different spot sizes and some are not homogeneous, thus the shape of the emitted flux as a function of the

[1] To describe the energy loss of a FF within a target it is needed to take into account the compound that the target is made of. Thus, the total thickness of the compound, its density and stopping power will be of interest.

Table 6.2: Summary on the efficiency (ϵ) values for each sample as a function of its position with respect to the neutron beam and the neutron incoming energy.

	Foil towards neutron beam		Foil against neutron beam	
	E_n (MeV)	ϵ	E_n (MeV)	ϵ
^{235}U (#2 & #6)	-	-	0.5	0.990
	-	-	2.8	0.995
^{235}U (#1)	-	-	0.5	0.991
	-	-	2.8	0.995
^{238}U	1.6	0.982	1.6	0.994
	3.0	0.980	3.0	0.995
^{237}Np	0.3	0.955	-	-
	3.0	0.951	-	-
^{240}Pu	0.5	0.994	0.5	1.0
	2.6	0.989	3.0	0.997
^{242}Pu	0.5	0.979	0.3	0.984
	2.8	0.974	3.0	0.989

Table 6.3: Correction due to the anisotropy in the neutron emission and the influence of the sample spot size and its inhomogeneities. The value presented is $\frac{\sum_i \%m_i^1 \Phi^1(\theta_i)}{\sum_i \%m_i^2 \Phi^2(\theta_i)}$. Only the ground state of the LiF reaction and the TiT reaction were considered. The different ^{235}U samples used in this work were made using the same technique and have nearly the same spot size, thus the results can be summarized under the same label.

Sample 2 $\longrightarrow$	^{235}U	^{238}U	^{237}Np
Sample 1 $\downarrow$			
^{238}U	$< 0.01\%$	-	$< 2.5\%$
^{237}Np	$< 2.5\%$	$< 2.5\%$	-
^{240}Pu	$< 0.02\%$	$< 0.04\%$	$< 1.3\%$
^{242}Pu	$< 0.02\%$	$< 0.02\%$	$< 1.3\%$

solid angle is used to correct for this differences. The influence of this effect for the first term of Equation (6.4), described in Equation (6.6), is listed in Table 6.3.

From Table 6.3 and Figure 3.3 it can be concluded that the strongest effect is due when the TiT neutron producing target is used with samples of different spot size. Specifically, the 2.5% correction on the ^{235,238}U(n,f)/^{237}Np(n,f) ratios when the TiT neutron producing target was used. As it can be noticed, the inhomogeneities present in the electrodeposited samples (^{240,242}Pu) have an almost negligible effect.

The uncertainty of this correction is given by the uncertainty on the Legendre coefficients related with the emission of the neutrons. The uncertainty given in Refs. [37,38] for this parameter is 3% with either the LiF or the TiT neutron producing target. Thus, the uncertainty of the correction is of 3%, considering that the uncertainty on the mass distribution of the sample has a negligible impact on the correction.

6.2.4 Correction due to the excited state of ^{7}Li(p,n)^{7}Be

The ^{7}Li(p,n)^{7}Be reaction has an excited state with a proton energy threshold of 2.3 MeV. The energy of the neutron emitted in this excited state is around 0.4 MeV lower than the neutron emitted in the ground state. Equation (6.4) accounts for this secondary energy using the label 1. Nevertheless the influence of this correction to the final cross section value is never greater than 1%.

6.2.5 Correction of the neutron spectrum by thermalized fast neutrons due to the setup

One of the drawbacks of using a VdG accelerator without any time-of-flight setup is that, even though the neutron energy is well-known within 10-50 keV (depending on the thickness of the neutron producing target), it is difficult to determine the energy of these neutrons at the moment that they interact with the fissile deposit. The neutrons in this experiment had to travel around 8 cm between the neutron producing target and the fissile deposits. During their path, they had to cross several surfaces (backing of the neutron producing target, water cooling setup, chamber structure). Each of these layers, but specially the water layer, alter the neutron energy reaching the fissile deposits. When considering two samples of similar spot size and similar fission threshold, the effect of having neutrons with lower energy will be nearly negligible. On the other hand, when a fissile sample is used together with a threshold sample or when two samples of very different fission threshold are used the knowledge of the background neutrons is a key point for the understanding of the results. This correction corresponds to the factor F in Equation (6.4).

Two different setups were used during the different experimental campaigns. First of all, a setup with no shielding was used, the water cooling in this case had a thickness between 1 to 3 mm (an average of 2 mm will be considered here on); this first setup will be labelled *setup #1*. A second setup with a shielding around the fission chamber as explained in Figure 3.9 was used when using the ^{235}U sample. A new water cooling with a thickness of 1 mm was employed in this case. The second geometry will be called *setup #2*.

The determination of the neutron background produced by the semi-thermalized neutrons was obtained by means of a Monte Carlo simulation using the transport code MCNP [47]. The geometry of the two different setups used is presented in Figure 6.2.

The energy of the emitted neutron was distributed according to the tables of Refs. [37, 38], as well as the emission angle and its emission probability. The result obtained was the average flux over the sample surface as a function of the incident neutron energy. The flux was normalized by the neutron-induced fission cross section of the corresponding isotope. An example of the neutron flux spectra obtained using

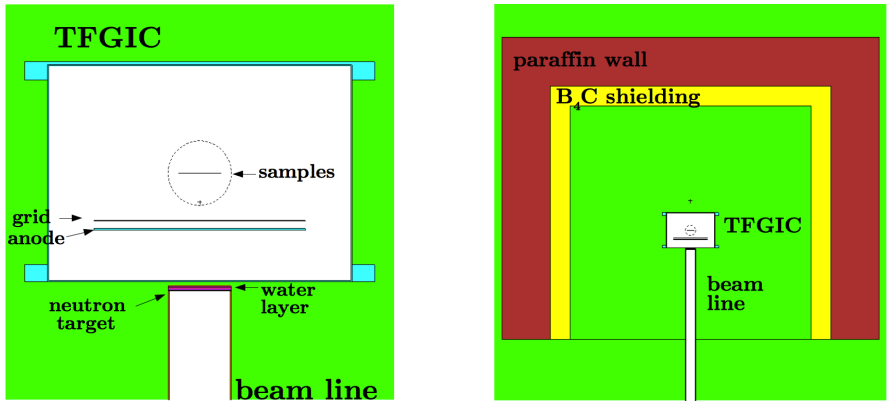

Figure 6.2: Geometry used in the simulations with the MCNP code. (a) *Setup #1*; (b) *setup #2*. Besides the shielding, the main difference between the two setups is the thickness of the water layer (2 mm for *setup #1*; 1 mm for *setup #2*).

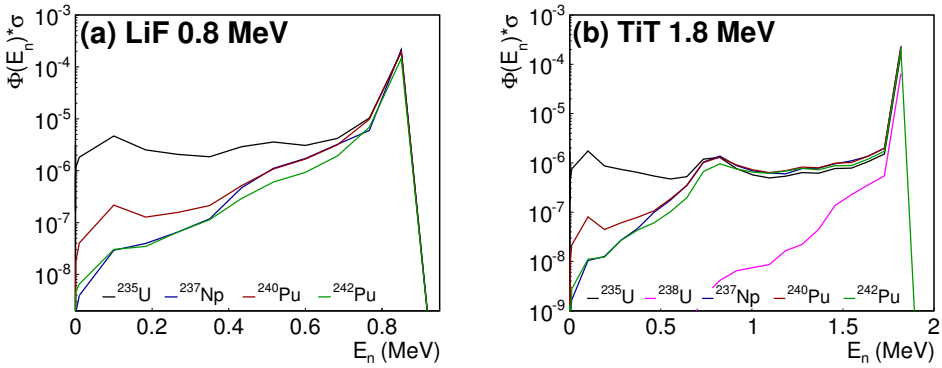

Figure 6.3: Neutron flux simulated with MCNP using the configuration of *setup #1* and normalized by the fission cross section for (a) 0.8 MeV LiF and (b) 1.8 MeV TiT.

setup #1 for each isotope at two different energies and using two different neutron producing targets is shown in Figure 6.3: (a) LiF 0.8 MeV and (b) TiT 1.8 MeV. The flux of the main neutron energy was normalized, then, by the total flux impinging the sample, obtaining the correction factor. Figures 6.4 and 6.5 present the correction factors as a function of the different isotopes and neutron energy for *setup #1* and *setup #2*, respectively, when using as neutron producing target (a) LiF or (b) TiT.

The main setup structures that lower the neutron energy are the backing of the neutron producing target, the water cooling of the neutron target, the target can and the ionization chamber structure. The effect of having the shielding structure in place

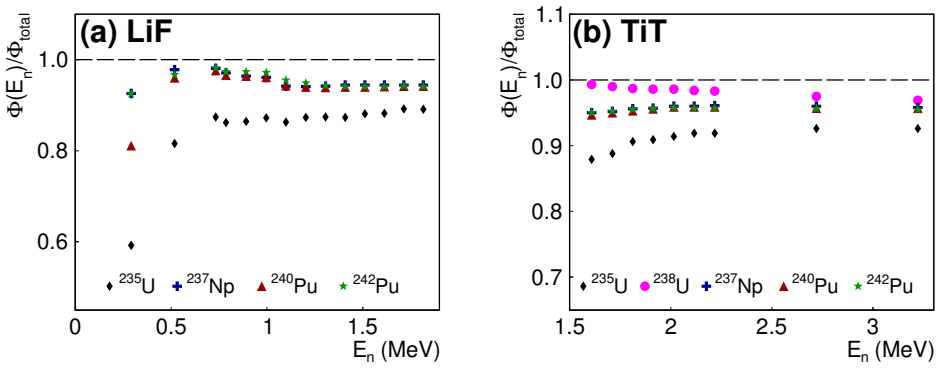

Figure 6.4: Correction factors to account for the neutrons outside the region of interest produced by a thermalization in the *setup #1* between the neutron producing target and the fissile deposits. The values plotted are the amount of neutrons that have passed the fissile deposit with the expected neutron energy normalized by the neutron-induced fission cross section of the isotope and the total number of neutrons crossing the surface. (a) Using a LiF neutron producing target; (b) Using a TiT neutron producing target. For each case the initial neutron energy was a distribution as a function of the emission angle. The differential cross section tables were taken from Refs. [37, 38].

for the measurements with the ^{235}U sample is around 1% on the neutron peak, and usually it cancels out when the ratio is performed for the two isotopes. Figure 6.6 presents the influence on some setup items in the thermalization of the neutron flux for (a) LiF at 0.8 MeV and 1.5 MeV and (b) TiT at 1.8 MeV and 2.2 MeV. For *setup #1* two modifications are presented: the setup without water (s1 nW) and without water and the ionization chamber structure (s1 nW nIC). In the case of *setup #2*, three modifications were done: without shielding (s2 nSH), without shielding and water cooling (s2 nSH nW) and additionally, without the ionization chamber structure (s2 nSH nW nIC). It is easy to recognize that the biggest influence comes from the water layer used to cool the neutron producing target. As mentioned, the influence of the shielding is negligible for the production of semi-thermalized neutrons, but it does effectively prevent thermalized neutrons backscattered in the target hall to interact with the fissile ^{235}U sample.

As an outcome, it is important to point out that these simulations are a key point to understand the results produced by using samples of very different thresholds. The uncertainty on these factors will be given for the ratio of two values and it is considered to be of 0.5%, since the variations on having a slightly different setup geometry did not give discrepancies higher than this value. The numerical values presented as figures in this section have been listed in Appendix A.

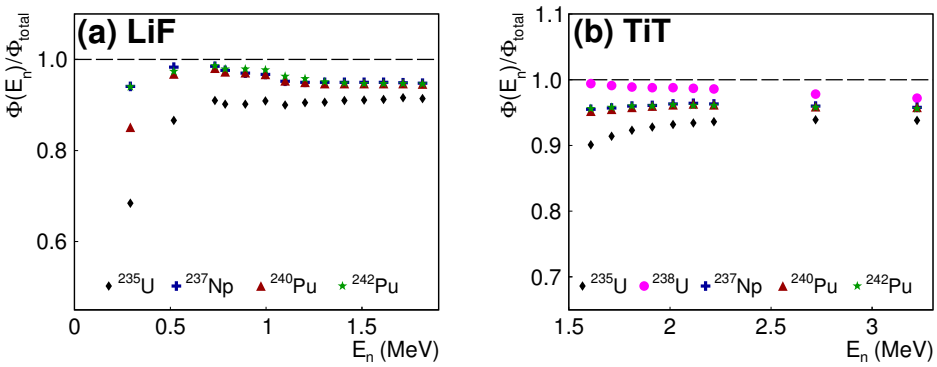

Figure 6.5: Correction factors to account for the neutrons outside the region of interest produced by a thermalization in the *setup #2* between the neutron producing target and the fissile deposits. The values plotted are the amount of neutrons that have passed the fissile deposit with the expected neutron energy normalized by the neutron-induced fission cross section of the isotope and the total number of neutrons crossing the surface. (a) Using a LiF neutron producing target; (b) Using a TiT neutron producing target. For each case the initial neutron energy was a distribution as a function of the emission angle. The differential cross section tables were taken from Refs. [37, 38].

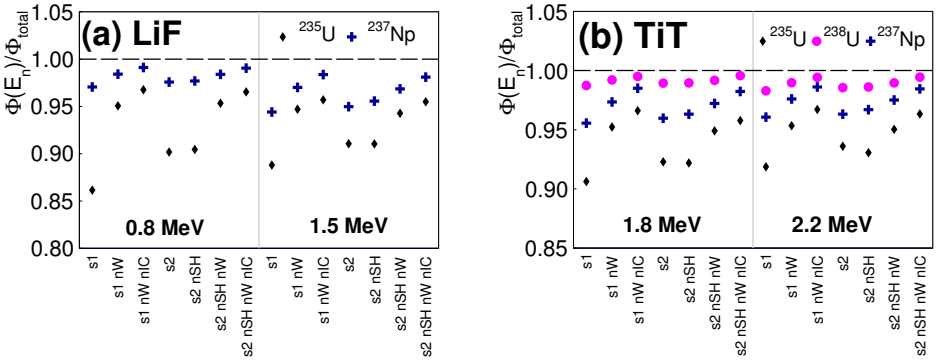

Figure 6.6: Influence of the shielding, the water layer and the ionization chamber to the correction factors for each of the two setups for (a) 0.8 MeV LiF and 1.5 MeV LiF and (b) 1.8 MeV TiT and 2.2 MeV TiT. Labels are: s1 (*setup #1*), s1 nW (*setup #1* without water layer), s1 nW nIC (*setup #1* without water layer and ionization chamber structure), s2 (*setup #2*), s2 nSH (*setup #2* without shielding), s2 nSH nW (*setup #2* without shielding and water layer), s2 nSH nW nIC (*setup #2* without shielding, water layer and ionization chamber structure). For a better visualization the ^{240,242}Pu correction factors are not shown since their cross section is very similar to the one of ^{237}Np. In the case of LiF only the correction factors of ^{235}U and ^{237}Np are presented, since no measurements were performed with ^{238}U. As it is noticeable for the two setups, the biggest influence comes from the water layer (2 mm for *setup #1* and 1 mm for *setup #2*), on the other hand, the shielding structure of *setup #2* has a negligible influence on the neutron background. Additionally, it is clear that isotopes with a fission threshold at higher energies are less affected by the neutron background than fissile isotopes.

6.3 Evaluations

The neutron-induced fission cross sections obtained using a back-to-back configuration need for their normalization a reliable and well determined reference cross section. In this work three different reference isotopes have been used, ^{237}Np, ^{238}U and ^{235}U. Among the three only the neutron-induced fission cross section of ^{235}U is considered as a primary standard. Yet, the ^{238}U(n,f) cross section is considered as a secondary standard. Finally, the ^{237}Np neutron-induced fission cross section has been lately pointed out by some experiments to be probably underestimated [80, 81].

The case of ^{237}Np(n,f)

Recent measurements of the neutron-induced fission cross section of ^{237}Np have indicated that it might be that this cross section needs to be studied in detail again. Paradela *et al.* [80] measured this cross section in an experiment together with ^{234}U(n,f) and ^{238}U(n,f). The other two isotopes showed good agreement with the evaluations in the fast neutron energy region. Nevertheless, the ^{237}Np fission cross section was measured about 5% higher. This data confirmed the data published already by Jiacoletti [82]. Figure 6.7 presents the ENDF, JEFF and JENDL evaluations for this isotope together with the two data sets mentioned.

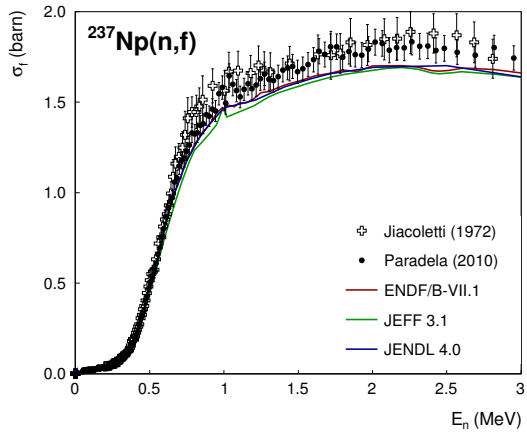

Figure 6.7: Different evaluations of the neutron-induced fission cross section of ^{237}Np. The measured data of Refs. [80, 82] show a 5% higher cross section than the present evaluations.

The case of ^{238}U(n,f) as secondary standard

The ^{238}U neutron-induced fission cross section is considered as a secondary standard by ENDF. Still, the recent evaluation of JEFF 3.2 shows a discrepancy of around 20% in the threshold and the plateau region with the ENDF and JENDL evaluations (see Figure 6.8).

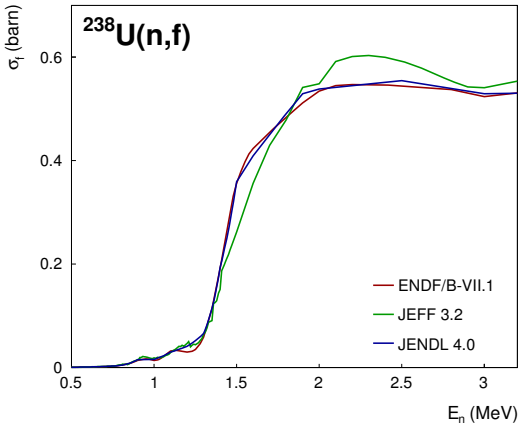

Figure 6.8: Different evaluations of the neutron-induced fission cross section of ^{238}U.

The case of ^{235}U(n,f) as primary standard

Seeing the previous cases of ^{237}Np(n,f) and ^{238}U(n,f) it is clear that the most reliable neutron-induced fission cross section is the one of ^{235}U. As it is seen in Figure 6.9 the three considered evaluations agree to a reasonable level in the neutron energy region covered in this work.

6.4 Uncertainties

A detailed description of the uncertainties related with the present measurements will give an overview of the accuracy of each correction independently. In Table 6.4 each source of uncertainty has been itemized. The acquisition system dead time is just relevant on those measurements when a sample with a short spontaneous fission half-life is employed, thus for ^{240,242}Pu. The uncertainty of the neutron spectrum correction was taken as 3% of the correction factor. As mentioned above, this 3% uncertainty is the one associated to the Legendre polynomial parameters of the neutron angular distribution fit. It is clear, finally, the major source of uncertainty is due to the ^{237}Np(n,f) ENDF evaluation when used.

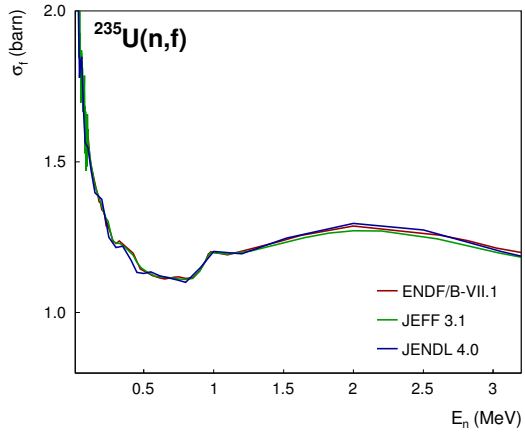

Figure 6.9: Different evaluations of the neutron-induced fission cross section of ^{235}U.

Table 6.4: Summary of the systematic uncertainties corresponding to the cross section measurements.

Uncertainty source	^{238}U	^{237}Np	^{240}Pu	^{242}Pu
Statistical	0.5%	0.5%	0.5%	<0.5%
Counts SF	-	-	<1.1%	<1.3%
Sample Mass	0.5%	0.3%	0.4%	0.9%
Reference sample ^{235}U mass	1.5% (samples #2 & #6)		2% (sample #1)	
Efficiency	1%			
Sample purity	0.001%			
Correction of neutron spectrum	<0.2%	<0.2%	<0.1%	<0.1%
MCNP correction of the thermalized flux (ratio)	0.5%			
^{237}Np - ENDF evaluation	-	-	2.2-4%	
^{238}U - standard [83]	-	0.7%		
^{235}U - standard [83]	< 0.8%			

The final uncertainty value is calculated as the quadratic sum of the corresponding uncertainties listed in Table 6.4 for each measurement ratio. A compendium is presented in Table 6.5. It is clear that the final uncertainty does not depend on the experimental statistics, but mainly on the value of the fission fragment loss inside the sample, the mass uncertainty and some of the evaluations used to normalize the data.

Table 6.5: Summary of the total uncertainty corresponding to each fission cross section ratio measured. The upper limit for each ratio is presented.

ratio	σ_{STAT}	σ_{SYST}	σ_{TOTAL}
^{238}U/^{235}U	0.6%	2.6%	2.7%
^{237}Np/^{235}U	0.5%	2.2%	2.3%
^{237}Np/^{238}U	0.4%	1.7%	1.8%
^{240}Pu/^{235}U	0.5%	2.5%	2.6%
^{240}Pu/^{238}U	0.6%	2.0%	2.1%
^{240}Pu/^{237}Np	0.7%	4.4%	4.5%
^{242}Pu/^{235}U	0.5%	3.0%	3.1%
^{242}Pu/^{238}U	1.4%	2.3%	2.7%
^{242}Pu/^{237}Np	0.8%	4.5%	4.6%

Chapter 7

Fission cross section results

7.1 Results on the fission cross section

In this Chapter a summary of the results obtained during all the measurements are presented. Several campaigns were performed from 2011 to 2014 (see Figure 7.1). In order to achieve the comprehension of the reader, the results of each set of experiments will be presented independently, as well as the conclusions that can be obtained. Finally, the overall results will be discussed. All the results presented here are obtained after applying all the corrections explained in Chapter 6.

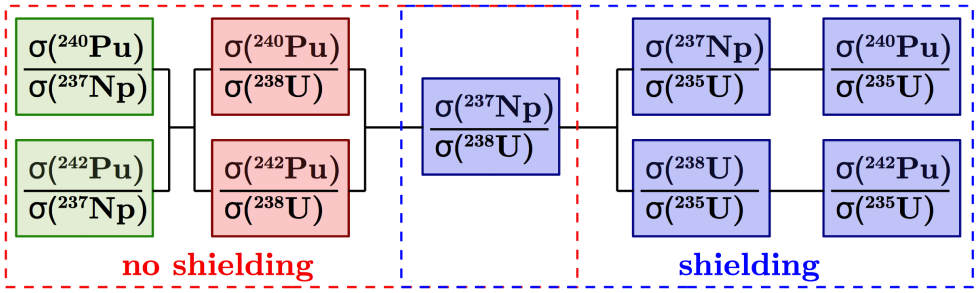

Figure 7.1: Scheme of the overall experimental campaigns. First experiments (green label) were performed of ^{240,242}Pu(n,f) relative to ^{237}Np(n,f) using *setup #1*. Afterwards, the secondary standard ^{238}U(n,f) was chosen to normalize our data of the plateau region (red label) as well using the *setup #1*. Finally, and due to some discrepancies with the available evaluations, an experiment to evaluate the ^{237}Np(n,f), ^{238}U(n,f) and ^{240,242}Pu(n,f) was performed using the primary standard ^{235}U(n,f) (blue labels); this campaign was performed mainly with the B_4C-paraffin shielding, thus using the *setup #2*.

7.1.1 Measurements of ^{240,242}Pu(n,f) relative to ^{237}Np(n,f)

A first experimental campaign was performed in December 2011. The aim of the campaign was to measure the neutron-induced fission cross section of both ^{240,242}Pu relative to ^{237}Np(n,f). The energy range was chosen from 300 keV up to 1.8 MeV in which the LiF reaction produces a none negligible neutron background.

The results normalized by the ENDF/B-VII.1 evaluation of ^{237}Np(n,f) are presented in Figures 7.2 and 7.3. The cross section values are systematically lower than most of the present evaluations; lower than 6% in the case of ^{240}Pu(n,f) and from 5 to 20% in the case of ^{242}Pu(n,f). The fission threshold of ^{240}Pu(n,f) is in concordance with the JEFF 3.1 evaluation, even though at the plateau region this evaluation shows larger discrepancies with the present data set. The data set obtained for ^{242}Pu(n,f) cannot reproduce the upper part of the fission threshold slope of the present evaluations, neither the resonance-like peak placed at 1.0 MeV nor the plateau region level. Additionally, two different runs performed at 0.9 MeV and at 1.0 MeV gave a difference of 3% and 9%, respectively. In the case of the 0.9 MeV data point, the difference can be considered negligible. For the 1.0 MeV, it is clear that the lower point is not following the trend of the rest of the set. Since it is not clear why this difference is observed, the point is discarded from the final cross section determination.

Even though corrections due to the sample size were included, a first thought was that the issue might have come because of the different sample sizes. For this reason a new set of measurements was planned using a ^{238}U sample of the same spot size as the ^{240,242}Pu ones.

7.1.2 Measurements of ^{240,242}Pu(n,f) relative to ^{238}U(n,f)

The fission cross section threshold of ^{238}U is about 1.6 MeV, as it can be seen in Figure 6.8. Therefore, a TiT target was used as neutron producing target since its neutron energy range can go above the LiF limit (1.8 MeV) with no neutron background. The goal of this experiment was not only to cross check the results obtained with the ^{237}Np reference sample, but to retrieve the level and shape of the plateau region of both ^{240,242}Pu(n,f). Because of the high uncertainty on the sample mass provided by the original certificate of the ^{238}U sample, it was remeasured by a Single Frisch-Grid Ionization Chamber (further details were given in Chapter 3).

Figures 7.4 and 7.5 display the results obtained after the normalization with the ENDF/B-VII.1 evaluation of ^{238}U(n,f) (red dots) together with the previous results obtained with ^{237}Np(n,f) (blue stars). First of all, for both isotopes at the common incoming neutron energy of 1.8 MeV the ^{237}Np(n,f) data set and the ^{238}U(n,f) are consistent. Thus, in both cases in the plateau region the present results are about 9% lower than the present ENDF/B-VII.1 evaluation. In contrast, the data values at 1.6 MeV and 1.7 MeV obtained using ^{238}U(n,f) as reference do not maintain the overall plateau region shape and are unexpectedly larger than their corresponding values obtained using as reference ^{237}Np(n,f).

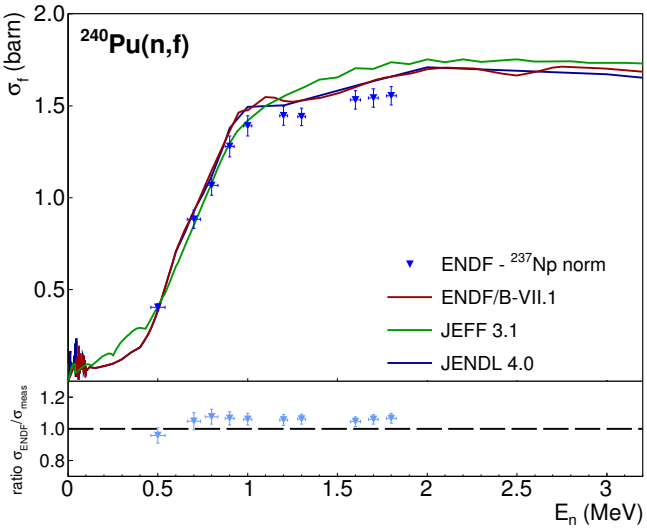

Figure 7.2: Neutron-induced fission cross section of ^{240}Pu using as reference ^{237}Np(n,f). The ratio plot shows clearly a systematic deviation of the experimental values compared to the ENDF/B-VII.1 evaluation. The experimental values agree with the fission threshold represented by the JEFF 3.1 evaluation. At the plateau region, though, the values are systematically lower than any evaluation.

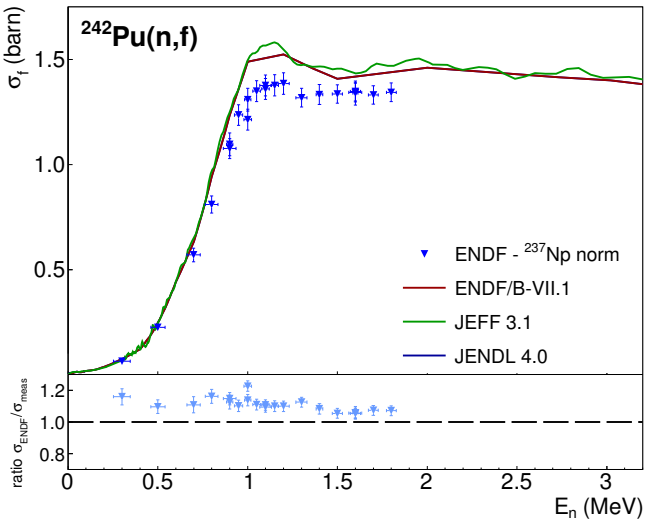

Figure 7.3: Neutron-induced fission cross section of ^{242}Pu using as reference ^{237}Np(n,f). The ratio plot shows clearly a systematic deviation of the experimental values compared to the ENDF/B-VII.1 evaluation.

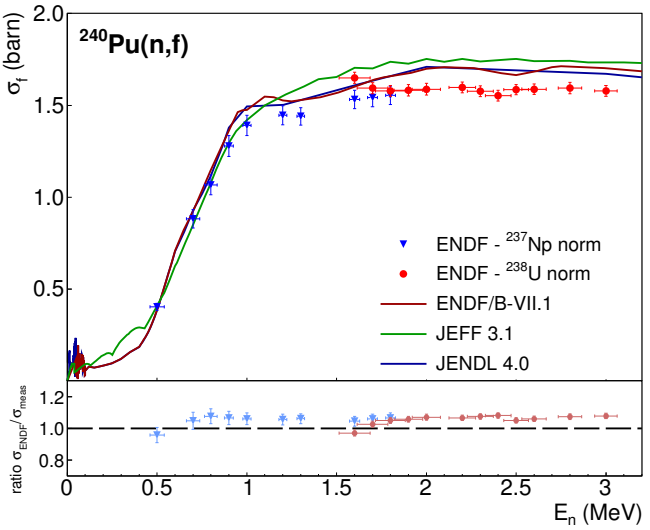

Figure 7.4: Neutron-induced fission cross section of ^{240}Pu using as reference ^{238}U(n,f). A clear agreement is found on the common data point at 1.8 MeV with the data taken relative to ^{237}Np(n,f). In this way, the plateau region is lower than evaluations for all the range. The values encountered for 1.6 MeV and 1.7 MeV show a clear discrepancy on the plateau shape, either due to an underestimation of the MCNP correction factors or a too large ^{238}U(n,f) ENDF/B-VII.1 evaluation. The ratio plot shows clearly a systematic deviation of the experimental values compared to the ENDF/B-VII.1 evaluation.

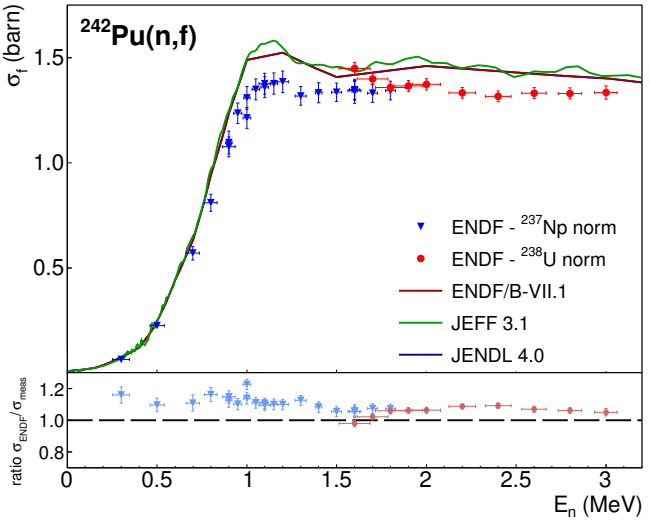

Figure 7.5: Neutron-induced fission cross section of ^{242}Pu using as reference ^{238}U(n,f). A clear agreement is found on the common data point at 1.8 MeV with the data taken relative to ^{237}Np(n,f). In this way, the plateau region is lower than evaluations for all the range. The values encountered for 1.6 MeV and 1.7 MeV show a clear discrepancy on the plateau shape, either due to an underestimation of the MCNP correction factors or a too large ^{238}U(n,f) ENDF/B-VII.1 evaluation. The ratio plot shows clearly a systematic deviation of the experimental values compared to the ENDF/B-VII.1 evaluation.

In conclusion, from the two measurements presented two statements can be put forward: (a) even though the two data sets are in agreement, the plateau level is lower than the stated evaluations, but has a similar shape compared with the evaluations for both ^{240,242}Pu(n,f); (b) either the fission threshold of ^{238}U(n,f) has too large values or our uncertainty characterizing the neutron flux is too large. Hence, new measurements to obtain the fission cross section of ^{237}Np and ^{238}U were conducted to point out whether it was possible to reproduce their evaluations and if the corrections applied were successful.

7.1.3 Measurements of ^{237}Np(n,f) relative to ^{238}U(n,f)

The understanding of both the ^{237}Np(n,f) and ^{238}U(n,f) cross sections is of importance to clarify the previous results obtained for the neutron-induced fission cross section of ^{240,242}Pu. It was decided first to measure the ^{237}Np(n,f) relative to ^{238}U(n,f) to avoid the use of a fissile sample with the need for a good determination of the thermal neutron background.

Specifically two different measurements were performed. In the first one a run at 1.8 MeV was conducted without any shielding around the TFGIC. The result, as it can be seen in Figure 7.6, was around 5% higher than any evaluation. Since the two isotopes have a different fission threshold and the beam line used was closer to the target hall wall a first thought was that there was a fast neutron background. Scattered neutrons might loose a few hundred keVs and, after, reach the detector with higher probability of interacting with the ^{237}Np sample than with the ^{238}U. Because of this reason, a first shielding was build around the chamber. A few runs were performed, but the outcome was the same. Finally, it was decided to build a proper shielding of B_4C-paraffin as explained in Chapter 3. The results obtained were in agreement with the measurements without the shielding and, as well, within uncertainties with the recent experiment of Paradela (2010) [80]. In addition, and as it happened with the ^{240,242}Pu(n,f), the value obtained at 1.6 MeV is too large compared with the rest of the set and does not maintain the plateau region shape.

The confidence on the result of the ^{237}Np(n,f) cross section fully relies on the cross section of ^{238}U(n,f). Because of that, it was tried to confirm the current ENDF/B-VII.1 evaluation of ^{238}U(n,f). Additionally, the measurement of the ^{237}Np(n,f) cross section needed to be extended at the fission threshold level, what implied the change of the ^{238}U sample to an isotope with much higher cross section at the 1 MeV region, namely ^{235}U.

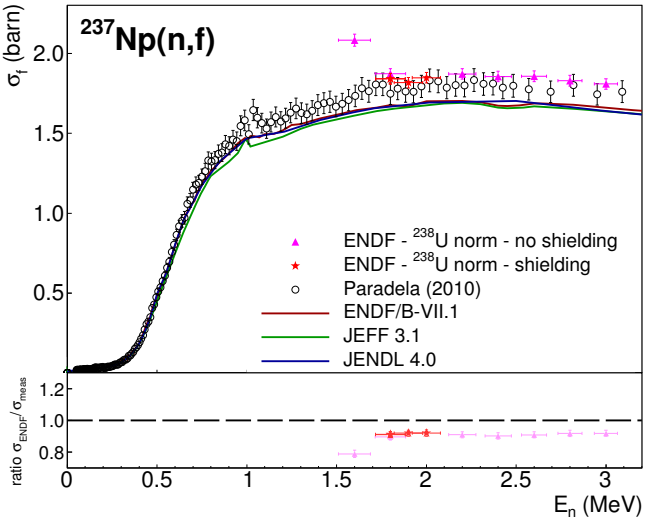

Figure 7.6: Neutron-induced fission cross section of ^{237}Np using as reference ^{238}U(n,f). The ratio plot shows clearly a systematic deviation of the experimental values compared to the ENDF/B-VII.1 evaluation of around 6%. As in the case of ^{240,242}Pu(n,f) the data point at 1.6 MeV does not maintain the plateau region shape.

7.1.4 Measurements of ^{238}U(n,f) relative to ^{235}U(n,f)

The cross section of ^{238}U(n,f) was measured from the fission threshold up to 3 MeV relative to the primary standard ^{235}U(n,f). Since ^{235}U is a fissile isotope care has to be taken to avoid low energy neutrons. A way to achieve that is to use a pulsed beam and determine the background flux when the beam is off. In the case of this experiment the shielding described in Chapter 3 was preferred.

The results obtained can be seen in Figure 7.7. The discrepancy of this experiment compared with the ENDF/B-VII.1 evaluation is around 6% in all the energy range except at the fission threshold (1.6 MeV) where it goes up to 10%. By shielding the chamber with a B_4C-paraffin wall the thermalized neutron room return was suppressed. Though, the fast background flux of neutrons produced by the setup in between the neutron producing target and the deposits could not be avoided. Nevertheless, their contribution will be higher for the fissile sample with no fission threshold. The data presented in the plot correspond to the values not corrected for the neutron background (black empty stars) and with the MCNP correction (red filled stars). Additionally, the shape of the cross section is not maintained, and it is obvious now, after comparing the present results with the ones obtained for ^{240,242}Pu(n,f) relative to ^{238}U(n,f), that the ENDF/B-VII.1 evaluation overestimates the fission cross section at the fission threshold.

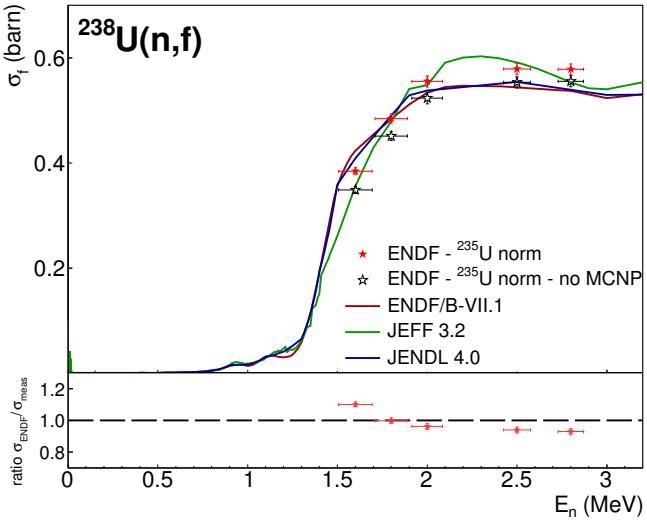

Figure 7.7: Neutron-induced fission cross section of ^{238}U using as reference ^{235}U(n,f). For completeness the MCNP corrected data (red filled stars) is presented together with the uncorrected (black empty stars). The ratio plot shows clearly a deviation of the experimental values compared to the ENDF/B-VII.1 evaluation at the fission threshold of around 10% and an overestimation at the plateau region of around 6%, when considering the corrected data.

7.1.5 Measurements of ^{237}Np(n,f) relative to ^{235}U(n,f)

The range of the data obtained for the determination of the ^{237}Np(n,f) cross section was extended using ^{235}U(n,f) as primary standard. In addition, it was decided to measure with this sample in all the energy range (0.5 MeV up to 3.0 MeV) to verify the results obtained using the ^{238}U(n,f) as reference.

The results retrieved are presented in Figure 7.8. The values reached at the threshold region are within uncertainties in agreement with the ENDF/B-VII.1 evaluation. The two common points taken both with LiF and with TiT (1.6 MeV and 1.8 MeV) differ about 5%. Up to now, the difference on the behavior of the data set taken with the LiF neutron producing target and the TiT neutron producing target is not clearly understood. The data set of ^{235}U(n,f) at the plateau region is slightly higher (5%) than the evaluations and around 2% lower than the values obtained using ^{238}U(n,f) as reference.

Comparing this results with the ones obtained for ^{240,242}Pu(n,f) it was expected that the values taken relative to ^{238}U(n,f) were lower than the present evaluations. As it is shown, this is not the case for the results ^{237}Np(n,f) relative to ^{238}U(n,f).

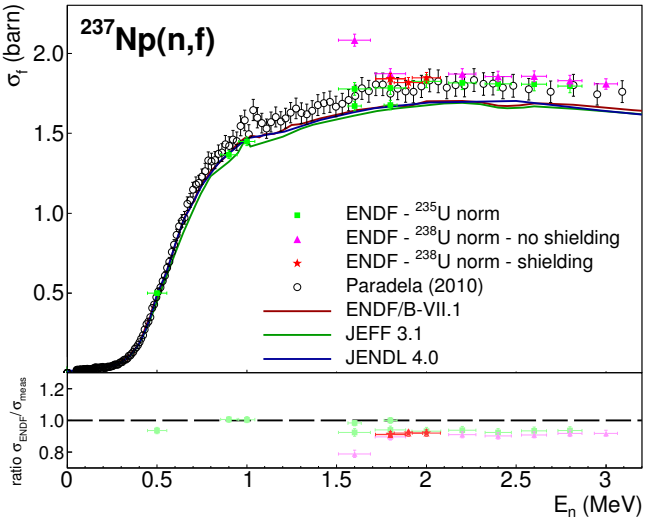

Figure 7.8: Neutron-induced fission cross section of ^{237}Np using as reference ^{238}U(n,f) and ^{235}U(n,f). The ratio plot shows an overall agreement with the ENDF/B-VII.1 evaluation for the ^{235}U(n,f) normalization using LiF as neutron producing target, but a systematic higher plateau region for the data taken using TiT targets in agreement with Paradela (2010) [80].

7.1.6 Measurements of ^{240,242}Pu(n,f) relative to ^{235}U(n,f)

A last measurement was performed to determine the cross section of both ^{240,242}Pu(n,f) relative to ^{235}U(n,f). Again, the B_4C-paraffin shielding was around the TFGIC. In the case of ^{240}Pu(n,f) only data taken with the LiF neutron producing target are presented.

The data sets taken using ^{235}U(n,f) as standard are presented together with the ones relative to ^{237}Np(n,f) and ^{238}U(n,f) in Figures 7.9 and 7.10. The results of the ^{235}U(n,f) normalization for ^{240}Pu(n,f) are consistent with the ones obtained in the previous run of ^{237}Np(n,f). Meaning that the fission threshold is consistent with the present evaluations but the plateau region shape is different. It is remarkable that the three values taken with different references at 1.8 MeV are very close. The case of ^{242}Pu(n,f) shows several differences compared to ^{240}Pu(n,f). First, the data of ^{235}U(n,f) taken with a TiT target were considered correct and can be included in the overall results. The data set of ^{242}Pu(n,f) obtained relative to ^{235}U(n,f) as standard and using a LiF neutron producing target is in agreement with the data relative to ^{237}Np(n,f). The ^{242}Pu(n,f) data obtained relative to ^{235}U(n,f) and the TiT target is in complete concord with the present ENDF/B-VII.1 evaluation. However it shows somewhat a similar structure than the JEFF 3.1 evaluation, but it has 6-9% higher values than the ones obtained using ^{238}U(n,f) as reference. This would result

in a verification of the increased cross section obtained for ^{238}U(n,f) (this issue will be treated extensively in the next Section). In addition, a 5% increase in the cross section is found when the neutron producing target was changed from LiF to TiT. This behavior is similar to what it has been presented for the ^{237}Np(n,f) case.

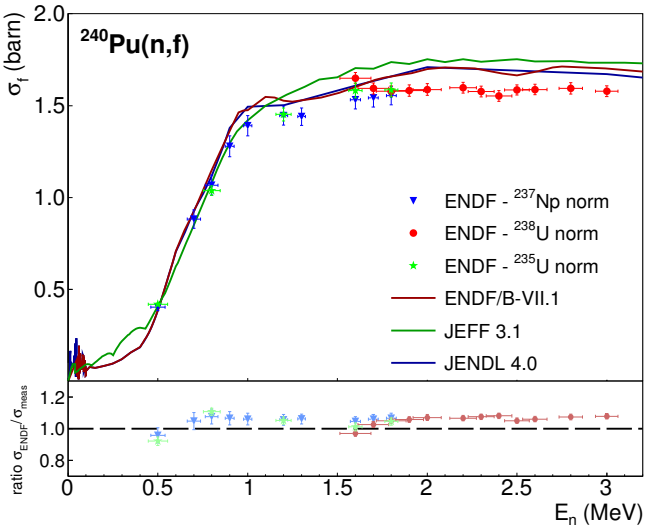

Figure 7.9: Neutron-induced fission cross section of ^{240}Pu using as reference ^{235}U(n,f), ^{238}U(n,f) and ^{237}Np(n,f). The agreement with the previous results using ^{237}Np(n,f) and ^{238}U(n,f) as reference is striking. Yet, the ratio plot shows a different plateau region shape than the ENDF/B-VII.1 evaluation.

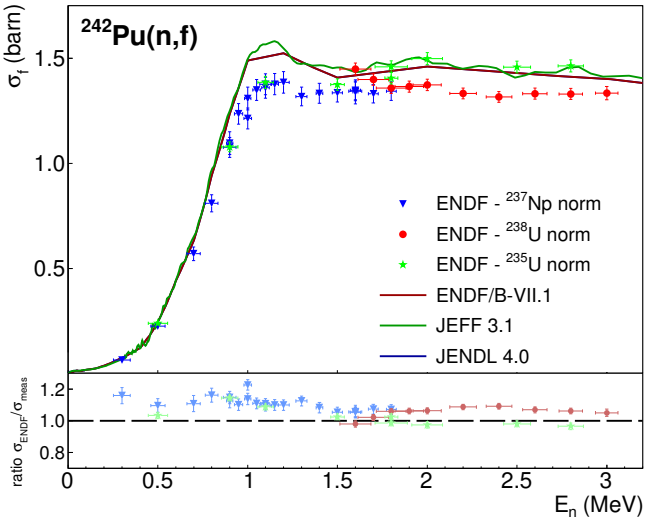

Figure 7.10: Neutron-induced fission cross section of ^{242}Pu using as reference ^{235}U(n,f), ^{238}U(n,f) and ^{237}Np(n,f). The fission threshold values obtained relative to ^{235}U(n,f) are in good agreement with the ones presented relative to ^{237}Np(n,f). In contrast, the ^{235}U(n,f) values retrieved using a TiT neutron producing target, even if they are in concordance with the present evaluations, their discrepancy with the ^{238}U(n,f) values is of 6 to 9%.

7.2 Discussions

The results presented in the previous section have been very carefully analyzed taking into account all corrections explained in Chapter 6. Nevertheless, their uncertainty is often above 2%, mainly due to the normalization to the reference fission cross section. In addition, between different runs with different reference samples discrepancies outside the error bars are observed. Hence, in the present section statements that are well understood will be presented and discussed. First, a discussion of the results obtained for the neutron-induced fission cross section of ^{238}U and ^{237}Np will be given. Later, the main characteristics of the ^{240,242}Pu(n,f) results will be explained.

7.2.1 ^{238}U(n,f) cross section

The fission cross section of ^{238}U is considered as a secondary standard. Some new measurements [84, 85] in the range of 30 MeV to 200 MeV and 5 MeV to 200 MeV, respectively, suggest an increase of the absolute cross section, as discussed in Ref. [83]. Besides, there are some data sets that determined a higher cross section than the current ENDF/B-VII.1 evaluation, such as the one of Lamphere (1956) [86]. The agreement of the present experiment with earlier literature values is satisfying at the threshold region, but 10% lower than the current ENDF/B-VII.1 evaluation. At the plateau region the present data follow the data set of Lamphere (1956) and agree with the JEFF 3.2 evaluation (see Figure 7.11). These later values are around 10% higher than most of the data sets available and the present ENDF and JENDL evaluations. The fission cross section obtained without the MCNP corrections follows the ENDF evaluation at the plateau region, nevertheless, in the present analysis it is shown that the MCNP corrections cannot be neglected.

7.2.2 ^{237}Np(n,f) cross section

The results of Figure 7.12 reveal a discrepancy using ^{235}U(n,f) as reference when data is taken with a LiF neutron producing target or a TiT neutron producing target. In the case of the data taken with the LiF, a rather good agreement (within 3%) is observed between the evaluations and the present ^{237}Np(n,f) data taken relative to ^{235}U(n,f). Nonetheless, the data taken using a TiT neutron producing target yielded values close to the ones of Paradela (2010) [80]. In addition, if the present data obtained for the ^{238}U(n,f) cross section will be used to normalize the ^{237}Np(n,f) cross section instead of the ENDF ^{238}U(n,f) evaluation, the discrepancy between Paradela's data set and the values obtained relative to ^{235}U(n,f) will become larger and amount to 15%. The reason for this mismatch of the ^{237}Np(n,f) cross section is presently unclear.

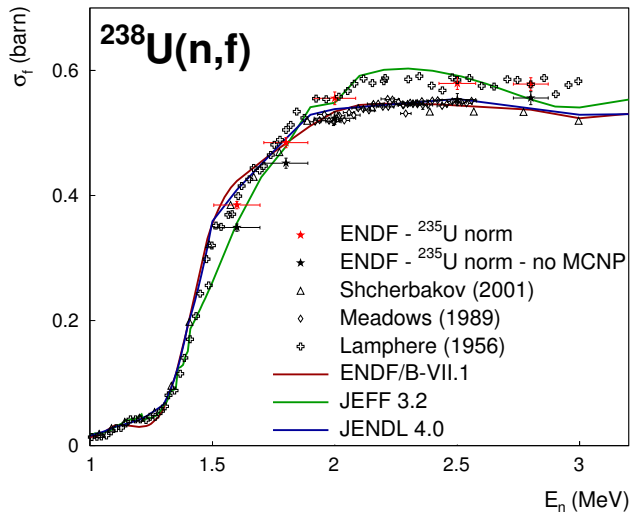

Figure 7.11: Summary of the neutron-induced fission cross section of ^{238}U data obtained normalized by ^{235}U(n,f) with (red stars) and without (black stars) MCNP corrections compared with the different evaluations available and three experimental data sets: Shcherbakov (2001) [87], Meadows (1989) [88] and Lamphere (1956) [86].

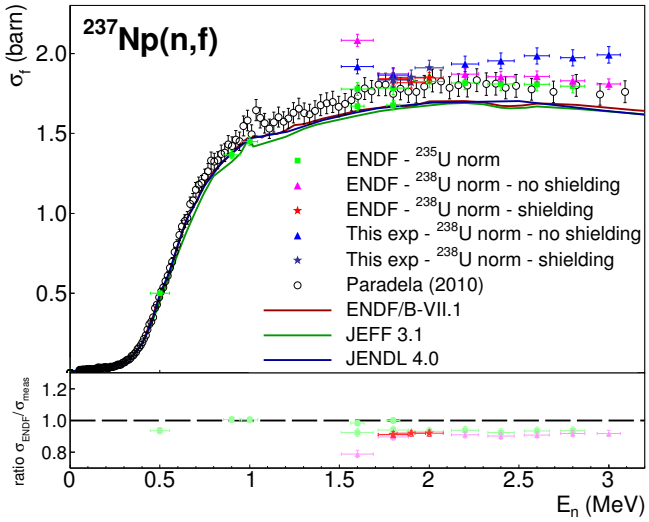

Figure 7.12: Summary of the neutron-induced fission cross section of ^{237}Np using as reference ^{238}U(n,f) and ^{235}U(n,f). A normalization using the ^{238}U(n,f) cross section values in this experiment is plotted as well. The ratio plot shows an overall agreement with the ENDF/B-VII.1 evaluation for the ^{235}U(n,f) normalization using LiF as neutron producing target, but a systematic higher plateau region for the data taken using TiT targets in agreement with Paradela (2010) [80]. The normalization using this experiment's ^{238}U(n,f) cross section is clearly mismatching the rest of the results and the plateau region shape.

7.2.3 ^{240}Pu(n,f) cross section

Considering the results obtained in the present experiment for the ^{238}U(n,f) cross section, and taking into account the agreement with previous experimental data, an interesting analysis would be to use the present ^{238}U(n,f) and ^{237}Np(n,f) results to normalize the data obtained for ^{240}Pu(n,f). Figure 7.13 shows all data sets together using the present ^{238}U(n,f) and ^{237}Np(n,f) data including MCNP corrections for normalization (gray dots). Below 1.8 MeV the agreement of the data normalized to the present ^{238}U(n,f) cross section is in concordance with the rest of the values determined at this energy. Finally, the shape at the plateau region resembles the one of the ENDF/B-VII.1 evaluation, though 5% lower values are found in the region 1.8-2.5 MeV. The values at 0.7 and 0.8 MeV normalized to the present ^{237}Np(n,f) cross section are lower than ENDF. The reason is that only two points in the ^{237}Np(n,f) cross section threshold were measured in this work, thus a linear interpolation was in between. The slope of this linear interpolation is, logically, different than the threshold slope for the ^{237}Np(n,f) cross section. As consequence, this leads to too small cross section values at 0.7 and 0.8 MeV.

7.2.4 ^{242}Pu(n,f) cross section

Following the procedure for ^{240}Pu(n,f), a normalization using the present ^{238}U(n,f) and ^{237}Np(n,f) cross section has been applied to the ^{242}Pu(n,f)/^{238}U(n,f) ratio and the ^{242}Pu(n,f)/^{237}Np(n,f) ratio. The overall results obtained using different normalizations can be explored in Figure 7.14. Using the new ^{238}U(n,f) normalization considering the MCNP corrections (gray dots) the values obtained from 1.8-2.5 MeV are off by 7-9% compared to the ones using the ^{235}U(n,f) normalization (green stars). In contrast, at higher energies, the concordance is striking. The problem of the normalization at 0.7 and 0.8 MeV using the present ^{237}Np(n,f) cross section is seen in this case, too.

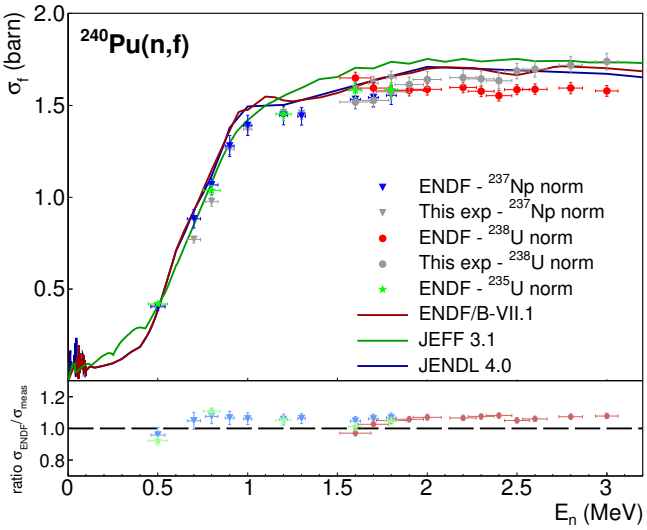

Figure 7.13: Summary of the ^{240}Pu(n,f) results obtained in this experiment. A new normalization using the experimental data of ^{238}U(n,f) presented in this work is used with MCNP corrections (gray dots). The overall agreement with the different normalizations is very high.

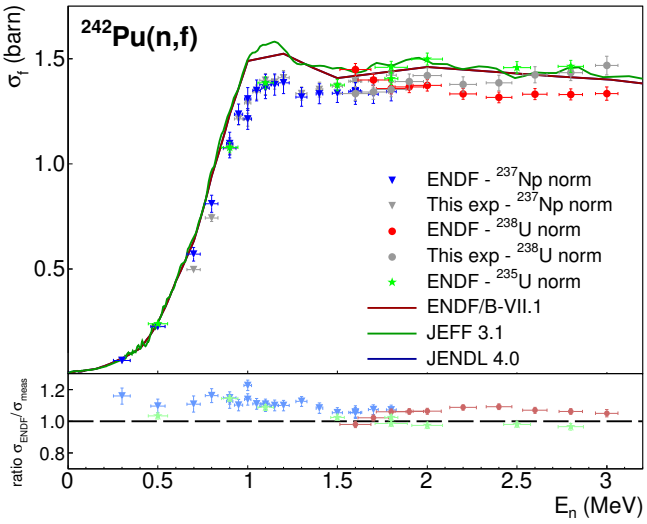

Figure 7.14: Summary of the ^{242}Pu(n,f) results obtained in this experiment. A new normalization using the experimental data of ^{238}U(n,f) presented in this work is used with MCNP corrections (gray dots). The overall agreement with the different normalizations is very high at the threshold region, though discrepancies are found at the 1.8-2.5 MeV region between the ^{238}U(n,f) normalization and the ^{235}U(n,f) normalization.

Conclusions

The determination of the neutron-induced fission cross section of ^{240,242}Pu was the main goal of this project. The detector chosen was a TFGIC that was assembled to work in a back-to-back configuration. The optimized settings of the detector were investigated during this work, using the experience with these chambers acquired over the past decades at the JRC-IRMM. To begin with, the spontaneous fission half-lives for both isotopes (^{240,242}Pu) were determined, reaching unprecedented statistics and achieving very small systematic uncertainties. The results of this particular work were already published in Paper I. In this way, the acquisition software could be developed as well as the analysis routines.

The cross section measurements were performed at the VdG laboratory at the JRC-IRMM. The quasi-monoenergetic neutron source provided a high intense flux at fast neutron energies. The energy range covered in this set of experiments was from 300 keV up to 3 MeV. Metallic lithium targets were tested during the period when this experiment took place. These targets would give much more neutrons compared to LiF targets. It is known, however, that metallic lithium diffuses into certain materials and reacts with atmospheric air. Therefore, the targets were prepared using passivation layers on the backing substrate and a protective cover was investigated. An extended description of this work is presented in Paper II. Three different reference samples (^{235}U, ^{238}U and ^{237}Np) were chosen to normalize the neutron flux. Very preliminary results using ^{237}Np(n,f) and ^{238}U(n,f) as reference cross sections were published in Paper III and Paper IV. The preliminary data of these two papers, published as conference proceedings, were based on a different ^{238}U sample mass and not considering any flux correction due to the background neutron contribution. Therefore, the results and conclusions need to be revised based on the results of Chapters 6 and 7.

Further investigations showed that the high α-activity of the ^{240,242}Pu samples needed special attention. In particular, the complete separation of the α-particle signals from the low energy fission fragment signals was at stake. To do so, the counting gas was changed from P10 to CH_4. All data was stored using a waveform digitizer for further offline analysis. Additionally, the mass of the ^{238}U sample was remeasured independently by two methods, as explained in Chapter 3: low geometry α-counting and using a single sided ionization chamber. The agreement on the value

obtained by the two methods was outstanding and within uncertainties. The mass value was 7% lower that the one mentioned in Paper III and Paper IV. Hence the difference between the two data sets published in there and the present ones was mainly due to the ^{238}U mass, as well as the neutron background flux correction.

Special emphasis has been put to determine the different systematic corrections. Not only the effects of the characteristics of the different deposits were considered, but an effort was put in the determination of the correct neutron flux impinging each deposit as a function of the isotope and the initial neutron energy spectra. Additionally, the study of the different reference samples independently of the ^{240,242}Pu(n,f) measurements, their evaluations and previous experimental data brought important information to meet the objectives of this work.

Figures A and B present the final fission cross section values for ^{240}Pu and ^{242}Pu, respectively. In each Figure two weighted averages are considered: all the primary data normalized to the ENDF evaluation (red crosses) and the primary data normalized to the ^{237}Np(n,f) and ^{238}U(n,f) cross section obtained in the present experiment (green stars). It is clear that the best agreement comes for both ^{240,242}Pu(n,f) cross section when the latter weighted average is used. In all cases, the uncertainty of the final value corresponds to the highest individual uncertainty at this incoming neutron energy. The window on the neutron energy corresponds to the neutron energy spread due to the thickness of the neutron producing target. When more than one measurement was done at a certain neutron energy the highest neutron energy spread was considered for the final value. The values used for calculating the weighted averages are listed in Appendix B. In the ^{242}Pu(n,f) case, an interpolation between two experimental values was performed prior to the weighted average calculation not to bias the results when only one experimental normalization at a single energy was available (either ^{238}U(n,f) or ^{235}U(n,f)).

The results obtained for the neutron-induced fission cross section of ^{240}Pu are in good agreement at the fission threshold with previous experimental data and with the current evaluations. At the plateau region, the present experiment is clearly comparable with the lower experimental values available in literature. Above 2.5 MeV only measurements relative to ^{238}U(n,f) were available. Hence, an overestimation at these energies of the ^{238}U(n,f) reference cross section could be the cause of the rising slope. The same effect is seen for the ^{242}Pu fission cross section. Comparable with the higher spontaneous fission half-life value obtained for ^{240}Pu, a possible explanation of the lower fission cross section values measured here might be due to a better separation of the low energy fission fragments compared with several α-particles piled up together.

In the case of the results achieved for the neutron-induced fission cross section of ^{242}Pu, the present experiment agrees with previous experimental data at the beginning of the fission threshold. At around a neutron energy of 0.7 MeV systematic discrepancies are observed, specially if the values presented here are compared with the present evaluations. First of all, the present experiment could not reproduce in any case the resonance-like structure that some previous experiments observed around 1.1 MeV.

Additionally, as can be seen in Figure B, the evaluations are following mainly the data sets with higher values. At the plateau region, this experiment is in concordance especially with the experiment of Staples (1998) [27] and Tovesson (2009) [35].

In Appendix B the presented numerical values are listed. For each isotope studied the values obtained using the different reference samples are first presented, together with the values used to normalize them. Second, the obtained weighted average values are given.

Finally, the investigations of the neutron-induced fission cross section of ^{237}Np did not lead to a clarification whether the present ENDF/B-VII.1 evaluation or the data of Paradela (2010) [80] are correct. But, if a weighted average of all the data obtain is performed (see Figure C) using either the ENDF normalization for ^{238}U(n,f) (red crosses) or the normalization using the present experimental data for ^{238}U(n,f) (green stars), a good agreement of the data with the evaluations is seen in the fission threshold. In contrast, a discrepancy in the plateau region is observed in both cases similar to the results of Paradela (2010) [80].

Regarding the ^{238}U neutron-induced fission cross section, the present experiment has obtained higher values than most of the available literature data. Nevertheless, using these results lead to coherent results for the ^{240,242}Pu fission cross sections. Therefore, and taking into account the challenges meet during the present experiment, it might be that the ^{238}U neutron-induced fission cross section in the fast neutron energy region (below 6 MeV) cannot be considered as a secondary standard. Moreover, the large discrepancies between the JEFF 3.2 and the ENDF/B-VII.1 need to be investigated. The results obtained in the present experiment are presented in Figure D together with the current evaluations and the data sets of Shcherbakov (2001) [87], Meadows (1989) [88] and Lamphere (1956) [86].

Proposals for further investigations

In view of the present results, new measurements of the ^{237}Np(n,f) and ^{238}U(n,f) cross section are highly recommended. Those measurements should be performed with a well characterized neutron flux beam, either from a VdG accelerator or a Linear accelerator. In case where there is no possibility to set up a time-of-flight measurement an effort should be taken to characterize the neutron flux. For instance, a specific proposal for the VdG facility would be to monitor with the ^{235}U(n,f) cross section the beam at different distances from the neutron producing target and with different water layer thicknesses to cool the neutron producing target. Furthermore, this monitoring could be compared with MCNP simulations of the setup used. The neutron angular distribution could be checked in the same way. Additionally, this would bring information on the systematic uncertainties related with the MCNP simulations. Finally, the 5% difference obtained between the data taken relative to ^{235}U using a LiF neutron producing target and a TiT neutron producing target needs to be investigated. This mismatch could be due to a deficiency on the MCNP simulations, since it was not present when the ^{240,242}Pu(n,f) cross section was measured relative to threshold reactions, such as ^{237}Np(n,f) or ^{238}U(n,f).

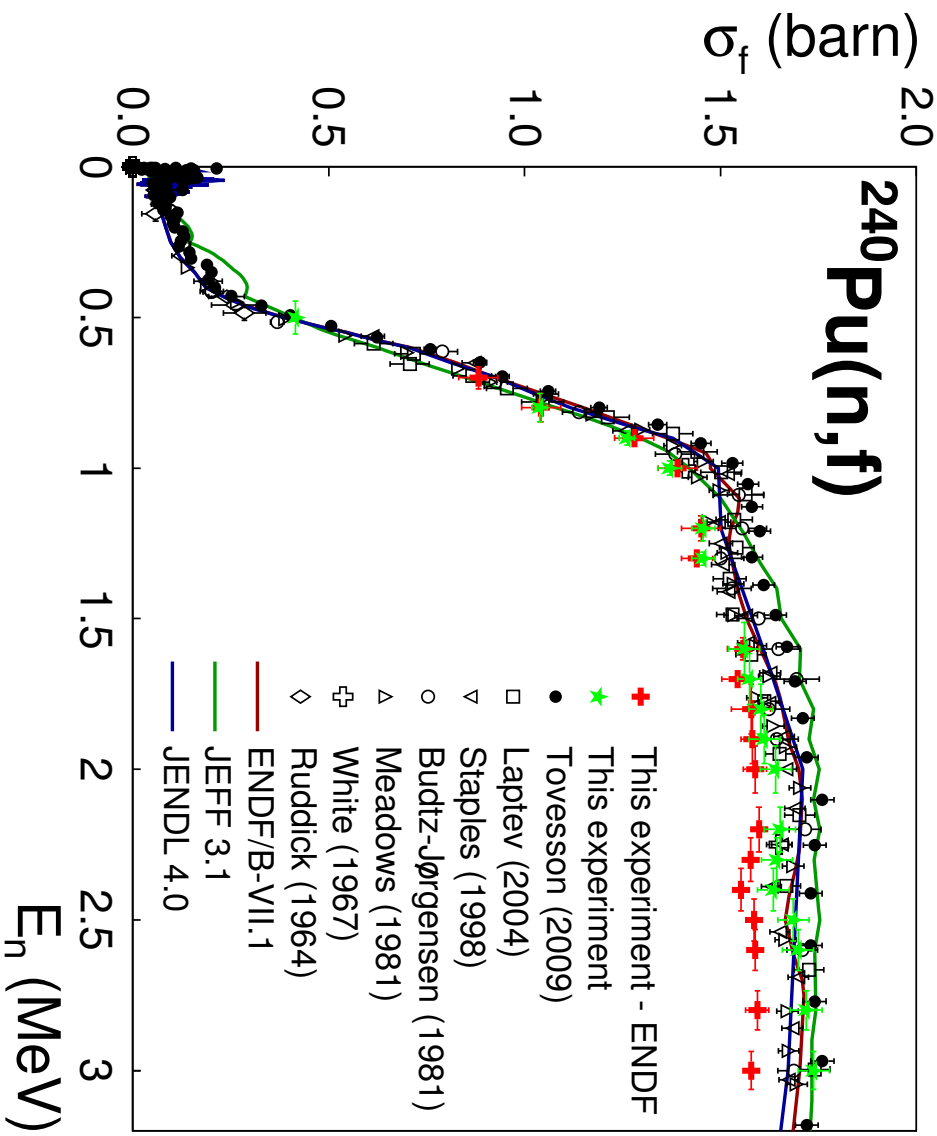

Figure A: Summary of the results of this experiment compared with the most relevant experiments performed on the neutron-induced fission cross section of ^{240}Pu and with current evaluations. Two weighted averages of the results of this experiment are plotted: one using purely the experimental data normalized to the ENDF evaluation of ^{237}Np(n,f) and ^{238}U(n,f) and the other normalizing the data using this experiment's results for ^{237}Np(n,f) and ^{238}U(n,f). The evaluations chosen are: ENDF/B-VII.1 [19], JEFF 3.1 [20] and JENDL 4.0 [21]. The experimental data shown are: Ruddick (1964) [22], White (1967) [23], Meadows (1981) [24], Budtz-Jørgensen (1981) [25], Staples (1998) [27], Laptev (2004) [26] and Tovesson (2009) [35]. Selected data points are shown for legibility of the plot. Data found as a ratio to ^{235}U(n,f) were normalized to the ENDF/B-VII.1 evaluation of this isotope. Further explanation is given in the text.

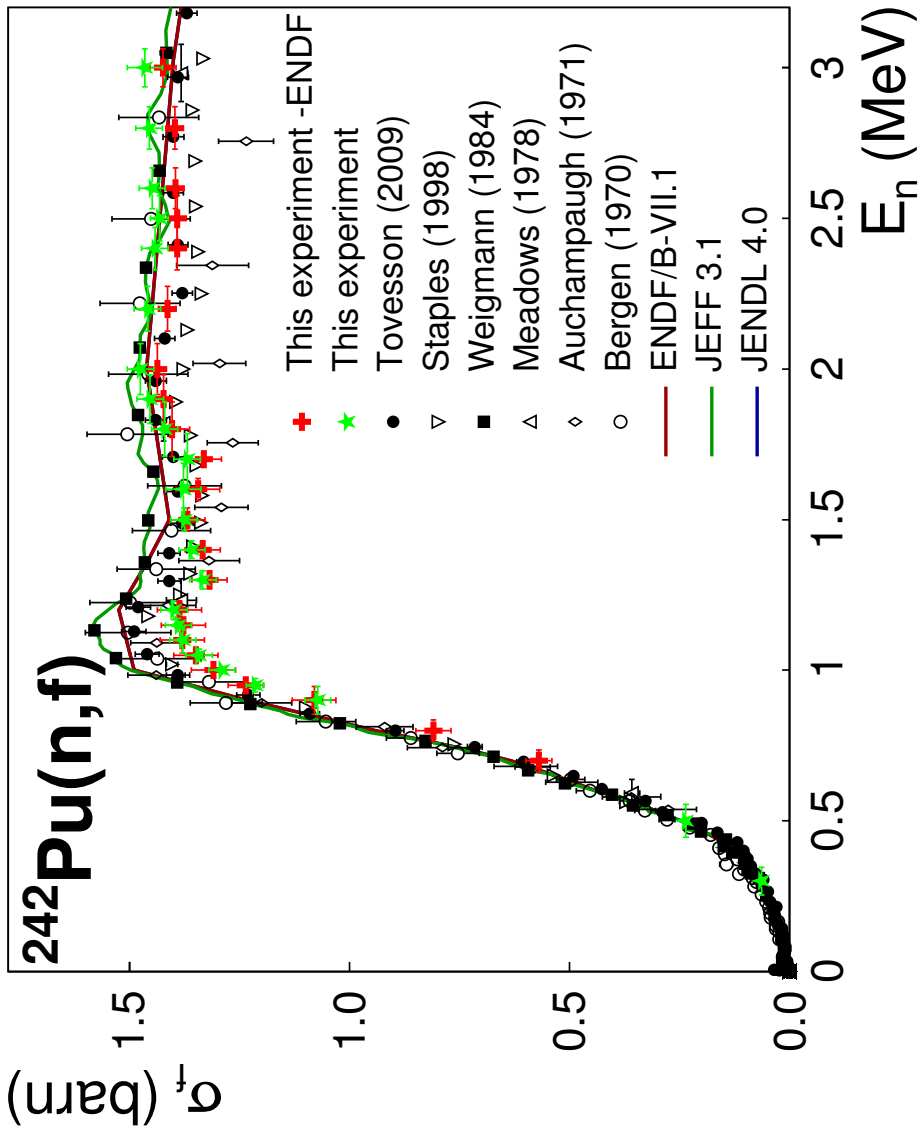

Figure B: Summary of the results of this experiment compared with the most relevant experiments performed on the neutron-induced fission cross section of ^{242}Pu and with current evaluations. Two weighted averages of the results of this experiment are plotted: one using purely the experimental data normalized to the ENDF evaluation of ^{237}Np(n,f) and ^{238}U(n,f) and the other normalizing the data using this experiment's results for ^{237}Np(n,f) and ^{238}U(n,f). The evaluations chosen are: ENDF/B-VII.1 [19], JEFF 3.1 [20] and JENDL 4.0 [21]. The JENDL 4.0 evaluation follows perfectly the ENDF/B-VII.1. The experimental data shown are: Bergen (1970) [31], Auchampaugh (1971) [32], Meadows (1978) [33], Weigmann (1984) [34], Staples (1998) [27] and Tovesson (2009) [35]. Selected data points are shown for legibility of the plot. Data found as a ratio to ^{235}U(n,f) were normalized to the ENDF/B-VII.1 evaluation of this isotope. Further explanation is given in the text.

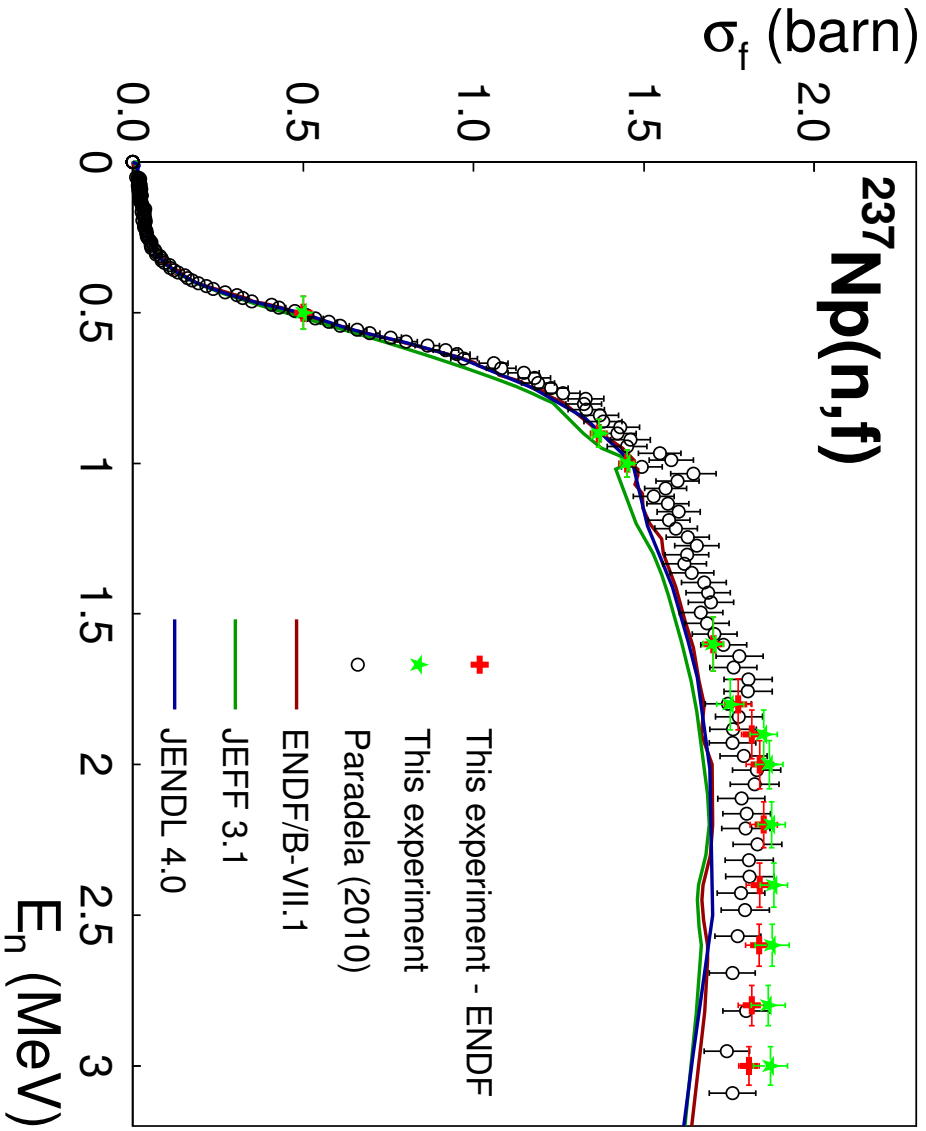

Figure C: Summary of the results of this experiment compared with Paradela (2010) [80] performed on the neutron-induced fission cross section of ^{237}Np and with current evaluations. Two weighted averages are plotted: using the ENDF normalization for ^{238}U(n,f) (red crosses) or using the normalization using this experiment's data for ^{238}U(n,f) (green stars).

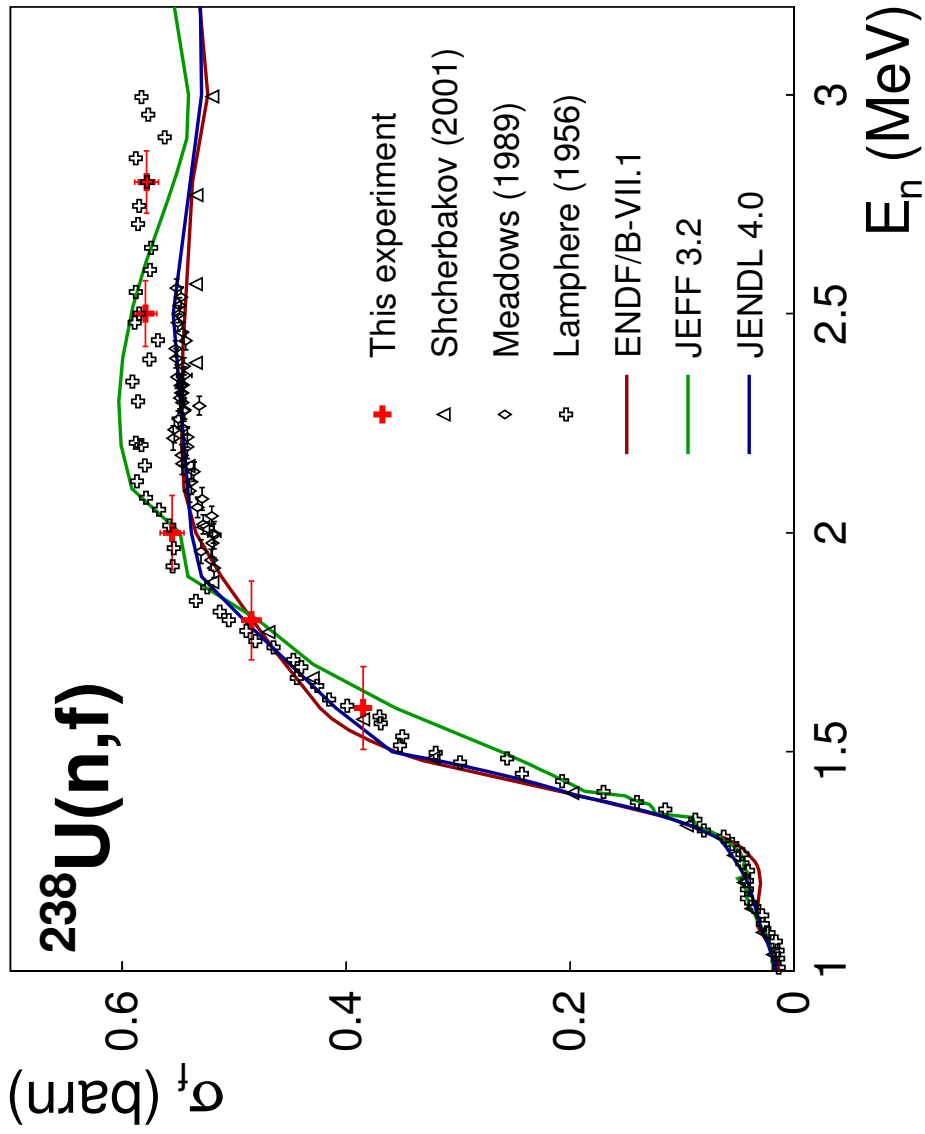

Figure D: Summary of the results of this experiment compared with some experiments performed on the neutron-induced fission cross section of ^{238}U and with current evaluations. The experimental data shown are: Lamphere (1956) [86], Meadows (1989) [88], Shcherbakov (2001) [87].

Appendix A
Numerical values of the MCNP simulations

In this Appendix the numerical values of the correction factors based on the MCNP simulations described in Chapter 6 are listed.

Table A.1: Numerical values of the correction factors corresponding to Figure 6.4(a). *Setup #1* was used for the simulations and the neutron producing target was a LiF.

E_n (MeV)	^{235}U	^{237}Np	^{240}Pu	^{242}Pu
0.291	0.592	0.926	0.811	0.925
0.518	0.816	0.978	0.960	0.967
0.733	0.874	0.981	0.976	0.982
0.786	0.862	0.971	0.966	0.974
0.891	0.864	0.964	0.964	0.974
0.996	0.872	0.961	0.961	0.972
1.099	0.863	0.942	0.943	0.955
1.203	0.873	0.941	0.940	0.949
1.306	0.874	0.942	0.939	0.943
1.408	0.873	0.944	0.940	0.941
1.511	0.881	0.944	0.940	0.941
1.613	0.882	0.944	0.941	0.941
1.715	0.892	0.944	0.942	0.942
1.816	0.891	0.944	0.942	0.941

Table A.2: Numerical values of the correction factors corresponding to Figure 6.4(b). *Setup #1* was used for the simulations and the neutron producing target was a TiT.

E_n (MeV)	^{235}U	^{238}U	^{237}Np	^{240}Pu	^{242}Pu
1.609	0.879	0.993	0.950	0.947	0.950
1.711	0.888	0.990	0.952	0.950	0.952
1.812	0.906	0.987	0.956	0.953	0.955
1.913	0.909	0.986	0.957	0.956	0.956
2.015	0.914	0.986	0.960	0.959	0.958
2.116	0.919	0.984	0.960	0.959	0.957
2.217	0.919	0.983	0.961	0.959	0.957
2.720	0.926	0.975	0.960	0.957	0.956
3.222	0.926	0.969	0.958	0.957	0.955

Table A.3: Numerical values of the correction factors corresponding to Figure 6.5(a). *Setup #2* was used for the simulations and the neutron producing target was a LiF.

E_n (MeV)	^{235}U	^{237}Np	^{240}Pu	^{242}Pu
0.291	0.684	0.941	0.851	0.940
0.518	0.866	0.983	0.968	0.974
0.733	0.910	0.985	0.981	0.986
0.786	0.902	0.976	0.973	0.979
0.891	0.902	0.970	0.971	0.979
0.996	0.909	0.967	0.967	0.977
1.099	0.900	0.952	0.953	0.963
1.203	0.905	0.950	0.950	0.958
1.306	0.906	0.950	0.947	0.951
1.408	0.910	0.950	0.947	0.948
1.511	0.911	0.950	0.947	0.947
1.613	0.912	0.950	0.947	0.947
1.715	0.916	0.949	0.947	0.947
1.816	0.914	0.948	0.946	0.946

Table A.4: Numerical values of the correction factors corresponding to Figure 6.5(b). *Setup #2* was used for the simulations and the neutron producing target was a TiT.

E_n (MeV)	^{235}U	^{238}U	^{237}Np	^{240}Pu	^{242}Pu
1.609	0.901	0.994	0.955	0.952	0.956
1.711	0.914	0.991	0.957	0.955	0.958
1.812	0.923	0.989	0.960	0.958	0.960
1.913	0.928	0.988	0.961	0.960	0.960
2.015	0.932	0.988	0.963	0.962	0.962
2.116	0.934	0.987	0.964	0.963	0.961
2.217	0.936	0.986	0.963	0.962	0.961
2.720	0.939	0.978	0.960	0.959	0.958
3.222	0.938	0.972	0.958	0.958	0.956

Table A.5: Numerical values of the correction factors corresponding to Figure 6.6(a). The influence of the different setup layers is analyzed at 0.8 MeV and 1.5 MeV using a LiF neutron producing target. Labels are: s1 (*setup #1*), s1 nW (*setup #1* without water layer), s1 nW nIC (*setup #1* without water layer and ionization chamber structure), s2 (*setup #2*), s2 nSH (*setup #2* without shielding), s2 nSH nW (*setup #2* without shielding and water layer), s2 nSH nW nIC (*setup #2* without shielding, water layer and ionization chamber structure).

	0.8 MeV		1.5 MeV	
	^{235}U	^{237}Np	^{235}U	^{237}Np
s1	0.862	0.971	0.888	0.944
s1 nW	0.951	0.984	0.947	0.970
s1 nW nIC	0.968	0.991	0.957	0.984
s2	0.902	0.976	0.911	0.950
s2 nSH	0.905	0.977	0.910	0.956
s2 nSH nW	0.953	0.984	0.943	0.969
s2 nSH nW nIC	0.965	0.990	0.955	0.981

Table A.6: Numerical values of the correction factors corresponding to Figure 6.6(b). The influence of the different setup layers is analyzed at 1.8 MeV and 2.2 MeV using a TiT neutron producing target. Labels are: s1 (*setup #1*), s1 nW (*setup #1* without water layer), s1 nW nIC (*setup #1* without water layer and ionization chamber structure), s2 (*setup #2*), s2 nSH (*setup #2* without shielding), s2 nSH nW (*setup #2* without shielding and water layer), s2 nSH nW nIC (*setup #2* without shielding, water layer and ionization chamber structure).

	1.8 MeV			2.2 MeV		
	^{235}U	^{238}U	^{237}Np	^{235}U	^{238}U	^{237}Np
s1	0.906	0.987	0.956	0.919	0.983	0.961
s1 nW	0.952	0.992	0.973	0.953	0.990	0.976
s1 nW nIC	0.966	0.995	0.985	0.967	0.994	0.986
s2	0.923	0.989	0.960	0.936	0.986	0.963
s2 nSH	0.922	0.990	0.963	0.931	0.986	0.967
s2 nSH nW	0.949	0.992	0.972	0.950	0.990	0.975
s2 nSH nW nIC	0.958	0.996	0.982	0.963	0.995	0.985

Appendix B
Numerical results of the cross section measurements

In this Appendix the numerical values presented in the cross section plots of Chapters 7 and 8 are listed.

The parameters presented in each table are: E_n (MeV), mean neutron energy; ΔE_n (MeV), uncertainty in neutron energy due to target thickness; σ (b), neutron-induced fission cross section; $\Delta\sigma$ (b), uncertainty on the neutron-induced fission cross section; and, $\sigma_{\mathbf{i,j}}$ (b), neutron-induced fission cross section of the isotope **i** used in the normalization (**j** refers to the ENDF/B-VII.1 evaluation - **ENDF** - or the weighted average of the results of this experiment - **exp** -).

As explained in Chapter 3 and 6, the neutron energy is not discrete but it has a distribution within a range. This range of neutron energies depends mainly on the thickness of the neutron producing target. Additionally, the (p,n) cross section of both LiF and TiT reactions do not have a constant behavior. Therefore, to calculate the cross section values these parameters were accounted for by weighting the neutron flux with the neutron-induced fission cross section of the reference isotope. In this way, the values presented in the weighted average tables (Tab. B.1 and B.4) might be slightly different than the ones written under the label $\sigma_{\mathbf{i,exp}}$, where **i** is the isotope.

B.1 Numerical results of the ^{238}U(n,f)

Table B.1: Measured ^{238}U(n,f) cross section using as a reference the ENDF/B-VII.1 ^{235}U(n,f) cross section. The values in brackets are the uncertainty in the last digit.

E_n (MeV)	ΔE_n (MeV)	σ (b)	$\Delta\sigma$ (b)	$\sigma_{\mathbf{235,ENDF}}$ (b)
1.6	0.094	0.385	0.006	1.253(7)
1.8	0.090	0.484	0.008	1.271(7)
2.0	0.085	0.555	0.010	1.284(7)
2.5	0.075	0.579	0.010	1.262(7)
2.8	0.071	0.578	0.010	1.240(8)

B.2 Numerical results of the ^{237}Np(n,f)

Table B.2: Measured ^{237}Np(n,f) cross section using as a reference the ENDF/B-VII.1 ^{238}U(n,f) cross section and the values obtained for the ^{238}U(n,f) cross section in this experiment (see Table B.1). The values in brackets are the uncertainty in the last digit.

E_n (MeV)	ΔE_n (MeV)	σ (b)	$\Delta\sigma$ (b)	$\sigma_{\mathbf{238,ENDF}}$ (b)	σ (b)	$\Delta\sigma$ (b)	$\sigma_{\mathbf{238,exp}}$ (b)
1.8	0.083	1.84	0.03	0.484(3)	1.83	0.04	0.482(8)
1.8	0.083	1.84	0.03	0.484(3)	1.84	0.04	0.482(8)
1.9	0.080	1.82	0.03	0.511(3)	1.85	0.04	0.521(8)
2.0	0.078	1.85	0.03	0.532(3)	1.91	0.04	0.550(10)
1.6	0.089	2.08*	0.03	0.419(3)	1.92*	0.04	0.386(5)
1.8	0.083	1.87	0.03	0.484(3)	1.87	0.04	0.482(8)
2.2	0.076	1.87	0.03	0.547(3)	1.94	0.04	0.565(12)
2.4	0.073	1.86	0.03	0.546(3)	1.95	0.04	0.574(14)
2.6	0.070	1.86	0.03	0.542(3)	1.99	0.05	0.579(16)
2.8	0.067	1.83	0.03	0.536(4)	1.97	0.05	0.578(10)
3.0	0.064	1.81	0.03	0.525(3)	1.99	0.05	0.578(10)

* Value not included in the final weighted average.

Table B.3: Measured ^{237}Np(n,f) cross section using as a reference the ENDF/B-VII.1 ^{235}U(n,f) cross section. The values in brackets are the uncertainty in the last digit.

E_n (MeV)	ΔE_n (MeV)	σ (b)	$\Delta\sigma$ (b)	$\sigma_{\mathbf{235,ENDF}}$ (b)
0.5	0.054	0.500	0.009	1.138(7)
0.9	0.046	1.37	0.02	1.142(7)
1.0	0.045	1.45	0.02	1.198(7)
1.6	0.038	1.67	0.02	1.253(7)
1.8	0.036	1.68	0.02	1.270(7)
1.6	0.089	1.78	0.03	1.253(7)
1.8	0.085	1.78	0.04	1.271(7)
2.0	0.080	1.83	0.04	1.284(7)
2.2	0.076	1.82	0.04	1.277(7)
2.4	0.073	1.81	0.04	1.267(7)
2.6	0.070	1.81	0.04	1.257(7)
2.8	0.067	1.80	0.04	1.240(8)

Table B.4: Weighted average of the measured ^{237}Np(n,f) cross section (1) using the ENDF/B-VII.1 ^{238}U(n,f) cross section normalization and (2) using the present ^{238}U(n,f) cross section. An interpolation between two experimental values was performed prior to the weighted average calculation not to bias the results when only one experimental normalization at a single energy was available (either ^{238}U(n,f) or ^{235}U(n,f)).

E_n (MeV)	ΔE_n (MeV)	σ_1 (b)	$\Delta\sigma_1$ (b)	σ_2 (b)	$\Delta\sigma_2$ (b)
0.5	0.054	0.500	0.009	0.500	0.009
0.9	0.046	1.37	0.02	1.37	0.02
1.0	0.045	1.45	0.02	1.45	0.02
1.6	0.089	1.70	0.03	1.70	0.03
1.8	0.085	1.78	0.04	1.75	0.04
1.9	0.080	1.82	0.03	1.85	0.04
2.0	0.080	1.84	0.04	1.87	0.04
2.2	0.076	1.85	0.04	1.88	0.04
2.4	0.073	1.84	0.04	1.88	0.04
2.6	0.070	1.84	0.04	1.88	0.05
2.8	0.067	1.83	0.04	1.87	0.05
3.0	0.064	1.80	0.04	1.87	0.05

B.3 Numerical results of the ^{240}Pu(n,f)

Table B.5: Measured ^{240}Pu(n,f) cross section using as a reference the ENDF/B-VII.1 ^{237}Np(n,f) cross section and the values obtained for the ^{237}Np(n,f) cross section in this experiment (see Table B.4). The values in brackets are the uncertainty in the last digits.

E_n (MeV)	ΔE_n (MeV)	σ (b)	$\Delta\sigma$ (b)	$\sigma_{\mathbf{237,ENDF}}$ (b)	σ (b)	$\Delta\sigma$ (b)	$\sigma_{\mathbf{237,exp}}$ (b)
0.5	0.040	0.404	0.018	0.486(20)	0.410	0.010	0.493(8)
0.7	0.037	0.88	0.05	1.068(57)	0.770*	0.017	0.930(13)
0.8	0.036	1.07	0.05	1.259(59)	0.98*	0.02	1.149(16)
0.9	0.024	1.28	0.05	1.375(56)	1.26	0.02	1.354(18)
1.0	0.023	1.39	0.05	1.468(51)	1.37	0.03	1.446(20)
1.2	0.022	1.45	0.05	1.520(47)	1.46	0.03	1.534(21)
1.3	0.022	1.44	0.04	1.559(44)	1.46	0.03	1.577(22)
1.6	0.028	1.53	0.04	1.642(44)	1.59	0.03	1.704(23)
1.7	0.028	1.54	0.04	1.658(44)	1.62	0.03	1.741(24)
1.8	0.027	1.55	0.05	1.675(45)	1.65	0.03	1.778(25)

* Value not included in the final weighted average.

Table B.6: Measured ^{240}Pu(n,f) cross section using as a reference the ENDF/B-VII.1 ^{235}U(n,f) cross section. The values in brackets are the uncertainty in the last digit.

E_n (MeV)	ΔE_n (MeV)	σ (b)	$\Delta\sigma$ (b)	$\sigma_{\mathbf{235,ENDF}}$ (b)
0.5	0.054	0.420	0.010	1.138(7)
0.8	0.047	1.04	0.02	1.115(7)
1.2	0.042	1.45	0.03	1.203(6)
1.6	0.037	1.58	0.04	1.253(7)
1.8	0.036	1.59	0.03	1.270(7)

Table B.7: Measured ^{240}Pu(n,f) cross section using as a reference the ENDF/B-VII.1 ^{238}U(n,f) cross section and the values obtained for the ^{238}U(n,f) cross section in the present (see Table B.1). The values in brackets are the uncertainty in the last digit.

E_n (MeV)	ΔE_n (MeV)	σ (b)	$\Delta\sigma$ (b)	$\sigma_{\mathbf{238,ENDF}}$ (b)	σ (b)	$\Delta\sigma$ (b)	$\sigma_{\mathbf{238,exp}}$ (b)
1.6	0.087	1.65*	0.02	0.420(3)	1.52	0.03	0.387(5)
1.7	0.085	1.59*	0.03	0.455(3)	1.53	0.03	0.436(6)
1.8	0.083	1.58	0.03	0.484(3)	1.57	0.03	0.482(7)
1.9	0.080	1.58	0.03	0.511(3)	1.61	0.04	0.521(8)
2.0	0.078	1.59	0.03	0.532(3)	1.64	0.04	0.550(9)
2.2	0.074	1.60	0.03	0.547(3)	1.65	0.04	0.565(10)
2.3	0.073	1.58	0.02	0.547(3)	1.64	0.04	0.570(10)
2.4	0.071	1.55	0.02	0.546(3)	1.63	0.04	0.575(10)
2.5	0.070	1.59	0.02	0.544(3)	1.69	0.04	0.578(10)
2.6	0.068	1.59	0.02	0.542(3)	1.70	0.04	0.579(11)
2.8	0.065	1.59	0.03	0.536(4)	1.72	0.04	0.578(10)
3.0	0.063	1.58	0.02	0.525(3)	1.74	0.04	0.578(10)

* Value not included in the final weighted average.

Table B.8: Weighted average of the measured ^{240}Pu(n,f) cross section (1) using the ENDF/B-VII.1 ^{238}U(n,f) and ^{237}Np(n,f) cross section normalization and (2) using this experiment ^{238}U(n,f) and ^{237}Np(n,f) cross section.

E_n (MeV)	ΔE_n (MeV)	σ_1 (b)	$\Delta\sigma_1$ (b)	σ_2 (b)	$\Delta\sigma_2$ (b)
0.5	0.054	0.416	0.018	0.415	0.010
0.7	0.037	0.882	0.05	-	-
0.8	0.047	1.04	0.05	1.04	0.02
0.9	0.024	1.28	0.05	1.26	0.02
1.0	0.023	1.39	0.05	1.37	0.03
1.2	0.042	1.45	0.05	1.46	0.03
1.3	0.022	1.44	0.04	1.46	0.03
1.6	0.087	1.56	0.04	1.56	0.04
1.7	0.085	1.54	0.04	1.57	0.03
1.8	0.083	1.58	0.05	1.60	0.03
1.9	0.080	1.58	0.03	1.61	0.04
2.0	0.078	1.59	0.03	1.64	0.04
2.2	0.074	1.60	0.02	1.65	0.04
2.3	0.073	1.58	0.02	1.64	0.04
2.4	0.071	1.55	0.02	1.69	0.04
2.6	0.068	1.59	0.02	1.70	0.04
2.8	0.065	1.59	0.03	1.72	0.04
3.0	0.063	1.58	0.02	1.74	0.04

B.4 Numerical results of the ^{242}Pu(n,f)

Table B.9: Measured ^{242}Pu(n,f) cross section using as a reference the ENDF/B-VII.1 ^{237}Np(n,f) cross section and the values obtained for the ^{237}Np(n,f) cross section in this experiment (see Table B.4). The values in brackets are the uncertainty in the last digits.

E_n (MeV)	ΔE_n (MeV)	σ (b)	$\Delta\sigma$ (b)	$\sigma_{\mathbf{237,ENDF}}$ (b)	σ (b)	$\Delta\sigma$ (b)	$\sigma_{\mathbf{237,exp}}$ (b)
0.3	0.047	0.064	0.003	0.078(3)	0.064	0.003	0.078(3)
0.5	0.040	0.225	0.010	0.486(20)	0.228	0.006	0.493(7)
0.7	0.037	0.57	0.03	1.068(57)	0.497*	0.012	0.930(14)
0.8	0.036	0.81	0.04	1.259(59)	0.740*	0.017	1.149(16)
0.9	0.034	1.08	0.04	1.375(56)	1.06	0.02	1.354(18)
1.0	0.032	1.21*	0.04	1.468(51)	1.20*	0.03	1.446(20)
1.1	0.032	1.38	0.05	1.490(46)	1.38	0.03	1.491(20)
1.2	0.031	1.39	0.05	1.520(47)	1.40	0.03	1.534(21)
1.3	0.031	1.32	0.04	1.559(43)	1.33	0.03	1.577(22)
1.4	0.029	1.33	0.04	1.591(44)	1.36	0.03	1.619(22)
1.5	0.029	1.34	0.04	1.615(43)	1.37	0.03	1.662(23)
1.6	0.028	1.35	0.04	1.642(44)	1.40	0.03	1.704(23)
1.7	0.028	1.33	0.04	1.658(44)	1.40	0.03	1.741(24)
1.8	0.027	1.34	0.04	1.675(45)	1.43	0.03	1.778(24)
0.9	0.018	1.10	0.05	1.375(56)	1.08	0.03	1.354(18)
1.0	0.018	1.31	0.05	1.468(51)	1.29	0.03	1.446(20)
1.1	0.021	1.36	0.04	1.490(46)	1.36	0.03	1.491(20)
1.6	0.015	1.34	0.05	1.642(44)	1.39	0.04	1.704(23)
0.95	0.023	1.24	0.04	1.433(50)	1.21	0.02	1.407(19)
1.05	0.021	1.35	0.05	1.480(45)	1.34	0.03	1.471(20)
1.15	0.022	1.38	0.05	1.500(46)	1.39	0.03	1.513(21)
1.6	0.036	1.34	0.04	1.642(44)	1.39	0.03	1.704(23)

* Value not included in the final weighted average.

Table B.10: Measured ^{242}Pu(n,f) cross section using as a reference the ENDF/B-VII.1 ^{235}U(n,f) cross section. The values in brackets are the uncertainty in the last digit.

E_n (MeV)	ΔE_n (MeV)	σ (b)	$\Delta\sigma$ (b)	$\sigma_{\mathbf{235,ENDF}}$ (b)
0.5	0.054	0.239	0.004	1.138(7)
0.9	0.046	1.08	0.02	1.142(7)
1.1	0.043	1.39	0.02	1.193(6)
1.5	0.038	1.38	0.02	1.240(7)
1.8	0.036	1.41	0.02	1.270(7)
1.8	0.090	1.46	0.02	1.271(7)
2.0	0.085	1.50	0.02	1.193(7)
2.5	0.075	1.46	0.02	1.262(7)
2.8	0.071	1.46	0.02	1.240(8)

Table B.11: Measured ^{242}Pu(n,f) cross section using as a reference the ENDF/B-VII.1 ^{238}U(n,f) cross section and the values obtained for the ^{238}U(n,f) cross section in this experiment (see Table B.1). The values in brackets are the uncertainty in the last digit.

E_n (MeV)	ΔE_n (MeV)	σ (b)	$\Delta\sigma$ (b)	$\sigma_{\mathbf{238,ENDF}}$ (b)	σ (b)	$\Delta\sigma$ (b)	$\sigma_{\mathbf{238,exp}}$ (b)
1.6	0.087	1.45*	0.02	0.420(3)	1.33	0.03	0.387(5)
1.7	0.085	1.40*	0.02	0.455(3)	1.34	0.03	0.436(6)
1.8	0.083	1.36	0.02	0.484(3)	1.35	0.03	0.482(7)
1.9	0.080	1.37	0.02	0.511(3)	1.39	0.03	0.521(8)
2.0	0.078	1.37	0.02	0.532(3)	1.42	0.03	0.550(9)
2.2	0.074	1.33	0.02	0.547(3)	1.38	0.03	0.565(10)
2.4	0.071	1.32	0.02	0.546(3)	1.39	0.03	0.575(10)
2.6	0.068	1.33	0.02	0.542(3)	1.42	0.03	0.579(11)
2.8	0.065	1.33	0.02	0.536(4)	1.43	0.03	0.578(10)
3.0	0.063	1.33	0.03	0.525(3)	1.47	0.04	0.578(10)

* Value not included in the final weighted average.

Table B.12: Weighted average of the measured ^{242}Pu(n,f) cross section (1) using the ENDF/B-VII.1 ^{238}U(n,f) and ^{237}Np(n,f) cross section normalization and (2) using the present ^{238}U(n,f) and ^{237}Np(n,f) cross section. An interpolation between two experimental values was performed prior to the weighted average calculation not to bias the results when only one experimental normalization at a single energy was available (either ^{238}U(n,f) or ^{235}U(n,f)).

E_n (MeV)	ΔE_n (MeV)	σ_1 (b)	$\Delta\sigma_1$ (b)	σ_2 (b)	$\Delta\sigma_2$ (b)
0.3	0.047	0.064	0.003	0.064	0.003
0.5	0.054	0.237	0.010	0.236	0.006
0.7	0.037	0.57	0.03	-	-
0.8	0.036	0.81	0.04	-	-
0.9	0.046	1.08	0.05	1.07	0.03
0.95	0.023	1.24	0.04	1.21	0.02
1.0	0.018	1.31	0.05	1.29	0.03
1.05	0.021	1.35	0.05	1.34	0.03
1.1	0.043	1.38	0.05	1.38	0.03
1.15	0.022	1.38	0.05	1.39	0.03
1.2	0.031	1.39	0.05	1.40	0.03
1.3	0.031	1.32	0.04	1.33	0.03
1.4	0.029	1.33	0.04	1.36	0.03
1.5	0.038	1.37	0.04	1.38	0.03
1.6	0.087	1.34	0.05	1.38	0.04
1.7	0.085	1.33	0.04	1.37	0.03
1.8	0.090	1.40	0.04	1.42	0.03
1.9	0.080	1.42	0.02	1.45	0.03
2.0	0.085	1.44	0.02	1.47	0.03
2.2	0.074	1.41	0.02	1.46	0.03
2.4	0.071	1.39	0.02	1.44	0.03
2.5	0.075	1.39	0.02	1.43	0.02
2.6	0.068	1.40	0.02	1.45	0.03
2.8	0.071	1.40	0.02	1.46	0.03
3.0	0.063	1.42	0.03	1.47	0.04

Acknowledgements

This thesis work could not have been performed without the help and collaboration of multiple people.

First of all, I am devoted to Dr. Hambsch who gave me the great opportunity to join his group at JRC-IRMM. He led me, trusted me and support me during my stay there. Without his scientific knowledge none of this could have been possible. Specially, I would like to thank him during the last part of the thesis, when he took over the experiment while I was in Barcelona. During this time, the discussions exchanged via email were essential to finish this work.

I would like to thank, as well, to Dr. Oberstedt. His fruitful discussions during this three years were encouraging. I really appreciate his will to help at any time, his objectivity and all his new ideas to push this work further.

To both of them, I will always appreciate that you had an open door to your office, because you made me feel like at home.

This project was carried out thanks to the financial support received from the ANDES Collaboration (Contract No. FP7-249671).

During this work I am devoted to the support I have received from Dr. Pretel at the Technical University of Catalonia.

To my officemate, colleague and friend Robert Billnert. I still remember the first day we met. Back then I could not imagine that thanks to him I will be writing this sentences today. Not only he supported me scientifically, but he was my support everyday. He made me believe in myself and gave me the strength to fight, when I could not.

To Dr. Bevilacqua and Dr. Bryś. I will always thank your support in my path through `c++` and `ROOT`. I could always come to you to ask and, even if I did not like the answer at first, I always got the best advisement.

To Dr. Frégeau and Dr. Göök, even if I had the chance to spend less working time with you, your help in developing the acquisition and analyzing programs in the later stage of this work was uncountable.

Additionally, I would like to thank to Dr. Al-Adili. His help at the beginning of this project was so precious. He led my first steps on TFGIC and nuclear fission.

I cannot forget of Dr. Jovančević, Dr. Matei, Dr. Borcea, Dr. Daraban and Dr. Dragić. To help made this group just the perfect place to work.

To Marzio Vidali to his help and support when using Linux systems and setting up experiments, as well as his overall disponibility. In addition, to take care of the last experiment together with Josch while I was in Barcelona. To the VdG technicians: Cedric Bonaldi, Carlos Chávez de Jesús, Thierry Gamboni and Wouter Geerts. Thanks for your availability, for all your answers to all my questions, for all your discussions, for coming to change energies during weekends and in the evenings, for doing this wonderful work to repair the Van de Graaff this last year and for delivering the beam. To Klaus Okkinga for his help during the target changes.

To the people at the Linac, specially to Dr. Mondelaers, Dr. Plompen and Carmen Cabanillas. Thanks as well to the target preparation group, to Goedele Sibbens and David Vanleeuw.

I would like to thank, in addition, to all the people who made my stay in Geel grateful. To Susana, Raquel, Robert, Nikola, Alf, Tomek, Riccardo, Maria José, Iria, and all the others, for all the nights out, conversations shared, trips made ... To my friends from the university: Ana, Cristi, Gemm, Larus, Meri; sense vosaltres mai hagués acabat la carrera. And my friends from school: Àlex, Alberto, Alfons, Ana, Carin, Cris, Mire, Ricky i Xavi; gràcies per tots aquests anys.

To Luis. I have no words to express my full gratitude to you, but thank you!

Als Pares per confiar sempre amb mi i donar-me suport incondicional, sense ells mai hagués arrivat fins aquí. A la Mar (i al Javi), al Pere i al Martí, per ser els germans que qualsevol desitjaria tenir. A l'Iu i al Jan, per què, tot i ser els petits de la casa, són els qui ens alegren cada dia. Al Blacky, al Joshi i a la Narya. Al Pairó, la Nené i a l'Erola, perquè gràcies a ells vaig decidir estudiar físiques.

References

[1] M. Salvatores, *Uncertainty and Target Accuracy Assessment for Innovative Systems Using Recent Covariance Data Evaluations (NEA/WPEC-26).* Nuclear Energy Agency (OECD), 2008.

[2] "ANDES project." [Online]. Available: http://www.andes-nd.eu

[3] International Energy Agency, "Key world energy statistics," 2013. [Online]. Available: http://iea.org/

[4] "Nuclear energy today," 2013. [Online]. Available: http://www.oecd-nea.org/

[5] International Energy Agency, "Technology Roadmap: Nuclear Energy," 2010. [Online]. Available: http://iea.org/roadmaps

[6] World Nuclear Associations, "Nuclear energy data," 2013. [Online]. Available: http://www.world-nuclear.org/

[7] International Atomic Energy Agency, "Power reactor information system." [Online]. Available: http://www.iaea.org/pris

[8] M. Salvatores and G. Palmiotti, "Radioactive waste partitioning and transmutation within advanced fuel cycles: Achievements and challenges," *Progress in Particle and Nuclear Physics*, vol. 66, no. 1, pp. 144–166, 2011.

[9] GenIV International Forum. [Online]. Available: https://www.gen-4.org

[10] ——, "GIF R&D Outlook for Generation IV Nuclear Energy Systems," 2009. [Online]. Available: https://www.gen-4.org

[11] GenIV International Forum, "Technology Roadmap Update for Generation IV Nuclear Energy Systems," 2014. [Online]. Available: https://www.gen-4.org

[12] Y. Giomataris, P. Rebourgeard, J. P. Robert, and G. Charpak, "MICROMEGAS: a high-granularity position-sensitive gaseous detector for high particle-flux environments," *Nuclear Instruments and Methods in Physics Research Section A: Accelerators, Spectrometers, Detectors and Associated Equipment*, vol. 376, no. 1, pp. 29–35, 1996.

[13] P. Salvador-Castiñeira, A. Tsinganis, M. Aïche, S. Andriamonje, G. Beliet, E. Berthoumieux, G. Boutoux, T. Bryś, M. Calviani, S. Czajkowski, N. Colonna, Q. Ducasse, R. Eykens, C. Guerrero, F. Gunsing, F.-J. Hambsch, B. Jurado, G. Kessedjian, C. Massimi, L. Mathieu, J. Mattarranz, A. Moens, S. Oberstedt, A. Plompen, C. Pretel, G. Sibbens, J. Taieb, D. Vanleeuw, M. Vidali, V. Vlachoudis, R. Vlastou, and the n_TOF collaboration, "Fission cross section measurements for ^{240,242}Pu," JRC scientific and policy reports, 2013, deliverable 1.5 of the ANDES project.

[14] A. Tsinganis, M. Calviani, E. Berthoumieux, S. Andriamonje, N. Colonna, C. Guerrero, F. Gunsing, C. Massimi, V. Vlachoudis, R. Vlastou, and the n_TOF collaboration, "The ^{242}Pu(n,f) measurement at the cern n_tof facility," September 8-12, 2014, fIESTA Fission School & Workshop Santa Fe.

[15] ——, "^{240,242}Pu(n,f) measurement update," January 8-11, 2013, 2nd ERINDA Progress Meeting, Jyväskylä.

[16] G. Kessedjian, G. Barreau, M. Aïche, B. Jurado, A. Bidaud, S. Czajkowski, D. Dassié, B. Haas, L. Mathieu, L. Tassan-Got *et al.*, "^{243}Am neutron-induced fission cross section in the fast neutron energy range," *Physical Review C*, vol. 85, no. 4, p. 044613, 2012.

[17] "MetroFission project." [Online]. Available: http://projects.npl.co.uk/metrofission/

[18] "Experimental Nuclear Reaction Data (EXFOR)." [Online]. Available: http://www.nndc.bnl.gov/exfor/exfor.htm

[19] M. B. Chadwick, M. Herman, P. Obložinskỳ, M. E. Dunn, Y. Danon, A. C. Kahler, D. L. Smith, B. Pritychenko, G. Arbanas, R. Arcilla *et al.*, "ENDF/B-VII.1 nuclear data for science and technology: cross sections, covariances, fission product yields and decay data," *Nuclear Data Sheets*, vol. 112, no. 12, pp. 2887–2996, 2011.

[20] A. Santamarina, D. Bernard, P. Blaise, M. Coste, A. Courcelle, T. Huynh, C. Jouanne, P. Leconte, O. Litaize, S. Mengelle *et al.*, "The JEFF-3.1.1 nuclear data library," *JEFF Report*, vol. 22, no. 10.2, p. 2, 2009.

[21] K. Shibata, O. Iwamoto, T. Nakagawa, N. Iwamoto, A. Ichihara, S. Kunieda, S. Chiba, K. Furutaka, N. Otuka, T. Ohasawa *et al.*, "JENDL-4.0: a new library for nuclear science and engineering," *Journal of Nuclear Science and Technology*, vol. 48, no. 1, pp. 1–30, 2011.

[22] P. Ruddick and P. White, "The measurement of the neutron fission cross section of ^{240}Pu in the energy range 60-500 keV," *Journal of Nuclear Energy. Parts A/B. Reactor Science and Technology*, vol. 18, no. 10, pp. 561–567, 1964.

[23] P. White, "The fission cross sections of 233U, 234U, 236U, 238U, 237Np, 239Pu, 240Pu and 241Pu relative to that of 235U for neutrons in the energy range 1-14 MeV," *Journal of Nuclear Energy*, vol. 21, pp. 671–679, 1967.

[24] J. Meadows, "Fission cross section of plutonium-240 relative to uranium-235 from 0.35 to 9.6 MeV," *Nuclear Science and Engineering*, vol. 79, no. 2, 1981.

[25] C. Budtz-Jorgensen and H.-H. Knitter, "Neutron induced fission cross section of Pu-240 in the energy range from 10 keV to 10 MeV," *Nuclear Science and Engineering*, vol. 79, p. 380, 1981.

[26] A. Laptev, A. Y. Donets, A. Fomichev, A. Fomichev, R. Haight, O. Shcherbakov, S. Soloviev, Y. V. Tuboltsev, and A. Vorobyev, "Neutron induced fission cross-sections of ^{240}Pu and ^{243}Am in the energy range 1-200 MeV," *Nuclear Physics A*, vol. 734, pp. E45–E48, 2004.

[27] P. Staples and K. Morley, "Neutron-induced fission cross-section ratios for 239Pu, 240Pu, 242Pu, and 244Pu relative to 235U from 0.5 to 400 MeV," *Nuclear Science and Engineering*, vol. 129, no. 2, pp. 149–163, 1998.

[28] T. Nakagawa, K. Shibata, S. Chiba, T. Fukahori, Y. Nakajima, Y. Kikuchi, T. Kawano, Y. Kanda, T. Ohsawa, H. Matsunobu *et al.*, "Japanese evaluated nuclear data library version 3 revision-2: JENDL-3.2," *Journal of Nuclear Science and Technology*, vol. 32, no. 12, pp. 1259–1271, 1995.

[29] D. K. Butler, "Fission cross section of plutonium-242," *Physical Review*, vol. 117, 1960.

[30] E. Fomushkin and E. Gutnikova, "Cross sections and angular distributions of fragments in the fission of ^{238}Pu, ^{242}Pu, and ^{241}Am by neutrons of energy 0.45-3.6 MeV," *Sovietic Journal of Nuclear Physics*, vol. 10, p. 529, 1970.

[31] D. Bergen and R. Fullwood, "Neutron-induced fission cross section of ^{242}Pu," *Nuclear Physics A*, vol. 163, no. 2, pp. 577–582, 1971.

[32] G. Auchampaugh, J. Farrell, and D. Bergen, "Neutron-induced fission cross sections of ^{242}Pu and ^{244}Pu," *Nuclear Physics A*, vol. 171, no. 1, pp. 31–43, 1971.

[33] J. Meadows, "Fission cross sections of plutonium-239 and plutonium-242 relative to uranium-235 from 0.1 to 10 MeV," *Nuclear Science and Engineering*, vol. 68, no. 3, 1978.

[34] H. Weigmann, J. Wartena, and C. Bürkholz, "Neutron-induced fission cross section of ^{242}Pu," *Nuclear Physics A*, vol. 438, no. 2, pp. 333–353, 1985.

[35] F. Tovesson, T. Hill, M. Mocko, J. Baker, and C. McGrath, "Neutron induced fission of ^{240,242}Pu from 1 eV to 200 MeV," *Physical Review C*, vol. 79, no. 1, p. 014613, 2009.

[36] G. Lövestam, "Energyset ver. 3.1," 2009.

[37] H. Liskien and A. Paulsen, "Neutron production cross sections and energies for the reactions T(p,n)^{3}He, D(d,n)^{3}He, and T(d,n)^{4}He," *Atomic Data and Nuclear Data Tables*, vol. 11, no. 7, pp. 569–619, 1973.

[38] ——, "Neutron production cross sections and energies for the reactions ^{7}Li(p,n)^{7}Be and ^{7}Li(p,n)^{7}Be*," *Atomic Data and Nuclear Data Tables*, vol. 15, no. 1, pp. 57–84, 1975.

[39] D. Vanleeuw, D. Sapundjiev, G. Sibbens, S. Oberstedt, and P. Salvador-Castiñeira, "Physical vapour deposition of metallic lithium," *Journal of Radioanalytical and Nuclear Chemistry*, vol. 299, no. 2, pp. 1113–1120, 2014.

[40] O. Frisch, "British atomic energy report," *BR-49*, vol. 65, 1944.

[41] O. Bunemann, T. Cranshaw, and J. Harvey, "Design of grid ionization chambers," *Canadian Journal of Research*, vol. 27, no. 5, pp. 191–206, 1949.

[42] A. Göök, F.-J. Hambsch, A. Oberstedt, and S. Oberstedt, "Application of the Shockley-Ramo theorem on the grid inefficiency of Frisch grid ionization chambers," *Nuclear Instruments and Methods in Physics Research Section A: Accelerators, Spectrometers, Detectors and Associated Equipment*, vol. 664, no. 1, pp. 289–293, 2012.

[43] A. Al-Adili, F.-J. Hambsch, R. Bencardino, S. Pomp, S. Oberstedt, and S. Zeynalov, "On the frisch–grid signal in ionization chambers," *Nuclear Instruments and Methods in Physics Research Section A: Accelerators, Spectrometers, Detectors and Associated Equipment*, vol. 671, pp. 103–107, 2012.

[44] T. Bortner, G. Hurst, and W. Stone, "Drift velocities of electrons in some commonly used counting gases," *Review of Scientific Instruments*, vol. 28, no. 2, pp. 103–108, 1957.

[45] M. A. Lieberman and A. J. Lichtenberg, *Principles of plasma discharges and materials processing*. John Wiley & Sons, 2005.

[46] Y. Han, *Spark plug based diagnostics for fuel-air ratio determination.* National Library of Canada, Bibliothèque Nationale du Canada, 1998.

[47] "MCNP." [Online]. Available: https://mcnp.lanl.gov/

[48] G. Sibbens, A. Moens, R. Eykens, D. Vanleeuw, F. Kehoe, H. Kühn, R. Wynants, J. Heyse, A. Plompen, R. Jakopič, S. Richter, and Y., "Preparation of ^{240}Pu and ^{242}Pu targets to improve cross section measurements for advanced reactors and fuel cycles," *Journal of Radioanalytical and Nuclear Chemistry*, no. 2, pp. 1093–1098, 2014.

[49] S. Pommé, "private communication," 2012.

[50] A. Göök, "private communication," 2014.

[51] G. Sibbens, A. Moens, and D. Vanleeuw, "private communication," 2013.

[52] C. Budtz-Jørgensen, H.-H. Knitter, and G. Bortels, "Assaying of targets for nuclear measurements with a gridded ionization chamber," *Nuclear Instruments and Methods in Physics Research Section A: Accelerators, Spectrometers, Detectors and Associated Equipment*, vol. 236, no. 3, pp. 630–640, 1985.

[53] "National Nuclear Data Center." [Online]. Available: http://www.nndc.bnl.gov/nudat2/chartNuc.jsp

[54] J. Heyse, M. Anastasiou, R. Eykens, A. Moens, A. J. M. Plompen, P. Schillebeeckx, G. Sibbens, D. Vanleeuw, and R. Wynants, "Characterization of 235U targets for the development of a secondary neutron fluence standard," *Journal of Radioanalytical and Nuclear Chemistry*, vol. 299, no. 2, pp. 1055–1059, 2014.

[55] R. V. Ammel, "private communication," 2013.

[56] "Daqpoint." [Online]. Available: http://www.daqpoint.nl/products/plug-in/M2i30xx_series.html

[57] T. Bryś, "Annual report 2011," JRC-IRMM Internal Reports, 2011.

[58] ——, "private communication," 2014.

[59] "ROOT." [Online]. Available: http://root.cern.ch/drupal/

[60] "C++." [Online]. Available: http://www.cplusplus.com/

[61] G. F. Knoll, *Radiation detection and measurement*, 4th ed. John Wiley & Sons, 2010.

[62] F. Tovesson, F.-J. Hambsch, S. Oberstedt, and H. Bax, "Fission fragment properties and the problem of the pulse height defect," *Journal of Nuclear Science and Technology*, pp. 673–676, 2002.

[63] J. Ziegler. [Online]. Available: http://www.srim.org/

[64] "Geant 4." [Online]. Available: http://geant4.web.cern.ch/geant4/

[65] K.-H. Schmidt and B. Jurado, "Gef-code version 2012/2.7."

[66] N. E. Holden, D. C. Hoffman *et al.*, "Spontaneous fission half-lives for ground-state nuclide (technical report)," *Pure and Applied Chemistry*, vol. 72, no. 8, pp. 1525–1562, 2000.

[67] V. P. Chechev, "The evaluation of ^{238}Pu, ^{240}Pu, and ^{242}Pu decay data," in *AIP Conference Proceedings*, vol. 769, no. 1. IOP INSTITUTE OF PHYSICS PUBLISHING LTD, 2005, p. 91.

[68] Chechev, 2009. [Online]. Available: http://www.nucleide.org/DDEP_WG/DDEPdata_by_Z.htm

[69] P. Fieldhouse, D. Mather, and E. Culliford, "The spontaneous fission half-life of ^{240}Pu," *Journal of Nuclear Energy*, vol. 21, no. 10, pp. 749–754, 1967.

[70] A. Androsenko, P. Androsenko, Y. V. Ivanov, A. Konyaev, V. Kositsyn, E. Tsenter, and V. Shchebolev, "Spontaneous fission half-life of ^{240}Pu," *Atomic Energy*, vol. 57, no. 5, pp. 788–791, 1984.

[71] J. Selickij, V. Funstein, and V. Jakovlev, *Proc. 38th Annual Conf. Nuclear Spectros. and Structure in Atomic Nuclei, Baku, 12-14 Apr., Acad. Sci. USSR*, p. 131, 1988.

[72] N. Dytlewski, M. Hines, and J. Boldeman, "The spontaneous fission half-life of Pu-240," *Nuclear Science and Engineering*, vol. 102, no. 4, pp. 423–427, 1989.

[73] Y. Ivanov, A. Konyaev, V. Kositsyn, E. Kholnova, V. Shchebolev, and M. Yudin, "^{240}Pu half-life ratios," *Soviet Journal of Atomic Energy*, vol. 70, p. 491, 1991.

[74] J. Mech, H. Diamond, M. Studier, P. Fields, A. Hirsch, C. Stevens, R. Barnes, D. Henderson, and J. Huizenga, "Alpha and spontaneous fission half-lives of Plutonium-242," *Physical Review*, vol. 103, pp. 340–341, 1956.

[75] J. Butler, M. Lounsbury, and J. Merritt, "The preparation and properties of ^{242}Pu," *Canadian Journal of Chemistry*, vol. 34, p. 253, 1956.

[76] V. Druin, V. Perelygin, and G. Khlebnikov, "Spontaneous fission periods of Np-237, Pu-238, and Pu-242," *Soviet Physics JETP-USSR*, vol. 13, no. 5, pp. 913–914, 1961.

[77] L. Z. Malkin, I. D. Alkhazov, A. S. Krivokhatskii, and K. A. Petrzhak, "The periods of spontaneous fission of Pu-240 and Pu-242," *Atomic Energy*, vol. 15, no. 2, pp. 851–852, 1964.

[78] J. Meadows, "Alpha and spontaneous fission half-lives of ^{242}Pu," Argonne National Lab., Ill.(USA), Tech. Rep., 1977.

[79] G. W. Carlson, "The effect of fragment anisotropy on fission-chamber efficiency," *Nuclear Instruments and Methods*, vol. 119, pp. 97–100, 1974.

[80] C. Paradela, L. Tassan-Got, L. Audouin, B. Berthier, I. Duran, L. Ferrant, S. Isaev, C. Le Naour, C. Stephan, D. Tarrío *et al.*, "Neutron-induced fission cross section of U-234 and Np-237 measured at the CERN Neutron Time-of-Flight (n_TOF) facility," *Physical Review C*, vol. 82, no. 3, p. 034601, 2010.

[81] L. Leong, L. Tassan-Got, L. Audouin, C. Paradela, J. Wilson, D. Tarrío, B. Berthier, I. Duran, C. Le Naour, and C. Stéphan, "Criticality experiments for validation of cross sections: The neptunium case," *Annals of Nuclear Energy*, vol. 54, pp. 36–42, 2013.

[82] R. Jiacoletti, W. Brown, and H. Olson, "Fission cross sections of Neptunium-237 from 20 eV to 7 MeV determined from a nuclear-explosive experiment," *Nuclear Science and Engineering*, vol. 48, pp. 412–1972, 1972.

[83] A. D. Carlson, V. G. Pronyaev, D. L. Smith, N. M. Larson, Z. Chen, G. M. Hale, F.-J. Hambsch, E. V. Gai, S.-Y. Oh, S. A. Badikov *et al.*, "International evaluation of neutron cross section standards," *Nuclear Data Sheets*, vol. 110, no. 12, pp. 3215–3324, 2009.

[84] R. Nolte and *et al.*, "Measurement of ^{235}U, ^{238}U, ^{209}Bi and $^{\text{nat}}$Pb fission cross sections using quasi-monoenergetic neutrons with energies from 30 to 150 MeV," *Proc. Int. Conf. on Nuclear Data for Science and Technology, 7-12 October 2011*, pp. 311–314, 2002.

[85] P. Lisowski, A. Gavron, W. Parker, J. Ullmann, S. Balestrini, A. Carlson, O. Wasson, and N. Hill, "Fission cross sections in the intermediate energy region," Los Alamos National Lab., NM (USA). Funding organisation: USDOE, Washington, DC (USA), Tech. Rep., 1991.

[86] R. Lamphere, "Fission cross sections of the uranium isotopes, 233, 234, 236, and 238, for fast neutrons," *Physical Review*, vol. 104, no. 6, p. 1654, 1956.

[87] O. Shcherbakov, Y. Donets, A. Evdokimov, A. Fomichev, T. Fukahori, A. Hasegawa, A. Laptev, V. Maslov, G. Petrov, Y. Tuboltsev, and A.S.Vorobiev, "Neutron-induced fission of 233-U, 238-U, 232-Th, 239-Pu, 237-Np, nat-Pb and 209-Bi relative to 235-U in the energy range 1-200 MeV," *Int. Sem. on Interactions of Neutrons with Nuclei*, no. 9, p. 257, 2001.

[88] J. Meadows, D. Smith, and L. Geraldo, "A search for possible structure in the ^{238}U(n, f) cross section near 2.3 MeV," *Annals of Nuclear Energy*, vol. 16, no. 9, pp. 471–476, 1989.

ATENCIÓ ¡

Les pàgines 123 a 153 de la tesi contenen els articles següents, que es poden consultar a les web dels editors.

ATENCIÓN ¡

Las páginas 123 a 153 de la tesis contienen los artículos siguientes, que puede consultarse en las webs de los editores

ATTENTION ¡

Pages 123 to 153 of the thesis are availables at the editor's web

Paper I: P. Salvador-Castiñeira, T. Bry´s, R. Eykens, F.-J. Hambsch, A. Moens, S. Oberstedt, G. Sibbens, D. Vanleeuw, and M. Vidali *Highly accurate measurements of the spontaneous fission half-life of 240,242Pu* Physical Review C **88**, 064611 (2013)

http://journals.aps.org/prc/abstract/10.1103/PhysRevC.88.064611

Paper II: D. Vanleeuw, D. Sapundjiev, G. Sibbens, S. Oberstedt, P. Salvador Castiñeira. *Physical vapour deposition of metallic lithium.* J. Radioanal. Nucl. Chem. (2014) 299:1113–1120

http://link.springer.com/article/10.1007%2Fs10967-013-2669-6

Paper III P. Salvador-Castiñeira, T. Bry´s, F.-J. Hambsch, S. Oberstedt, C. Pretel, and M. Vidali *Neutron-induced Fission Cross Section of 240,242Pu up to En = 3 MeV*. Nuclear Data Sheets 119 (2014) 55–57

https://www.oecd-nea.org/science/wpec/nemea7/docs/presentations/40_S5_Salvador.pdf